THE GHOST SOLID METHODS FOR THE SOLID-SOLID INTERFACE

ABOUZAR KABOUDIAN

(M.Eng., NTU)
(B.Sc., IUT)

A THESIS SUBMITTED

FOR THE DEGREE OF DOCTOR OF PHILOSOPHY
NUS GRADUATE SCHOOL FOR INTEGRATIVE
SCIENCES AND ENGINEERING
NATIONAL UNIVERSITY OF SINGAPORE

2014

Declaration

I hereby declare that the thesis is my original work and it has been written by me in its entirety. I have duly acknowledged all the sources of information which have been used in the thesis.

This thesis has also not been submitted for any degree in any university previously.

Abouzar Kaboudian

28 November 2014

To Elly, whose love, patience, and support made this work possible.

Acknowledgments

I would like extend my greatest gratitude to my research supervisor Prof. B.C. Khoo for his continuous guidance and support through every single step of this research, and for his patience through the tough times of this PhD. program. I would also like to thank Prof. Tie-Gang Liu for his invaluable guidance towards this project. Moreover, I would like to thank *NUS Graduate School of Integrative Sciences and Engineering* for providing the funds for this research project.

Contents

Summary

Original and modified variants of the Ghost Solid Method (GSM) are proposed for application to the boundary conditions at the solid-solid interface of isotropic linearly elastic, as well as elastic-plastic materials, in a Lagrangian framework. The methods are discussed for one dimensional as well as two dimensional settings with slip and no-slip conditions. The effect of using different solvers for these methods is discussed. It is shown, in the presence of the wave propagation through the solid-solid mediums, the original GSM can lead to large numerical errors in the solution, either in the form of large oscillations in stress and velocity at the interface, or significant deviations from the exact solution. A scheme for prediction of these errors at the interface is also introduced. The other two variants of GSM proposed, however, can remove the large numerical errors that may rise at the interface. Numerous numerical examples in one and two-dimensional settings are provided attesting to the viability and effectiveness of the GSM for treating wave propagation at the solid-solid interface.

List of Figures

List of Symbols

ρ	density
σ	stress
α	longitudinal wave speed
β	transverse wave speed
κ	current yield
$\mathbf{A}$	coefficient matrix
ε	displacement
ξ, η	normal and tangential coordinates
a	acceleration-added
b	body force vector
c	speed of sound in the medium
E	modulus of elasticity
E_p	modulus of plasticity
e_{kl}	deviatoric strain
F	flux function
G	flux function
h	plastic factor
p	$-\sigma$
S_{kl}	deviatoric stress tensor
t	time
U	variable vector

u	velocity component
v	velocity component
x, y, z	cartesian coordinates

Chapter 1

Introduction

Fluid Structure Interaction (FSI) modeling has gained significant interest among the research community in recent years. FSI modeling has been the subject of investigation in various areas, including but not limited to offshore oil and gas exploration and production industries [3–9], aerospace industries [10–15], geophysical wave propagation modeling [16–19], biomedical fields [20–27], and many more.

Systems with fluid solid interactions, and in general multi-medium systems, may involve the presence of various phases of material, namely fluid phase (liquid and gas), and solid phase. As a result, various interactions can be considered: liquid-liquid, gas-liquid, gas-gas, fluid-solid, and solid-solid interactions. Therefore, a robust, reliable, consistent, and coherent approach that can numerically model all these interactions is highly desirable.

Various research attempts have been made to obtain numerical methods which can simulate multi-medium interactions [28–33]. Due to the presence of mixed cells, existing multi-medium methods may have to make numerous assumptions about the shape and behavior of the interface. For example, the Volume-of-Fluid (VOF) method [34, 35], despite being a conservative method, diffuses the interface. Level set method [36, 37] has been extensively used [28,36–46] to preserve the interface sharp. However, this method is intrinsically not conservative. There are other attempts for simulating multi-medium problems such as the moment-of-fluid (MOF) methods [47], interface reconstruction-VOF methods [48], or the phase-field method [49].

Single medium solvers have matured significantly over the years. Various groups, in the research community, have implemented different single medium solvers, and tested them for their specific fields of application. Any technique that can reliably combine these single medium solvers, for multi-medium problems, in a mathematically consistent manner can be regarded as a significant development.

This work seeks to develop the Ghost Solid Methods (GSMs) to faithfully simulate and capture the boundary conditions at the interface for the elastic-elastic and elastic-plastic solid-solid interaction problems. Once combined with the Ghost Fluid Method counterparts, it shall be discussed that this can facilitate a consistent and truly multi-medium modeling of fluid and several layers of solid interaction using ghost nodes.

The Ghost Fluid Method (GFM) was first proposed in a pioneering work by Fedkiw et al. [2] for multi-material flows. The GFM can be easily extended to multi-dimensions and be applied to fairly complex geometries. The application of this method is simpler than other competing methods such as the Immersed Interface Method [50–57], or even the Immersed Boundary Method [58–61]. At the same time, the GFM keeps the solver intact. Due to its inherent simplicity, the GFM became very popular among the research community. To the date of the writing of this manuscript, this pioneering work has been cited over a thousand times by various authors.

In Chapter 2, we will briefly review the major approaches to solve for multi-medium problems. We will discuss various available methods and their respective advantages and disadvantages. This can enable the reader to appreciate the reason why the Ghost Solid Methods are the subject of this study.

In Chapter 3, we will introduce the Ghost Solid Methods for the one-dimensional elastic solids. Three variations of the method will be introduced, namely the Original Ghost Solid Method (OGSM), the Modified Ghost Solid Method (MGSM), and the Double Riemann Ghost Solid Method (DRGSM). It will be discussed that the OGSM, despite its simplicity to implement, is highly problem related and can cause large numerical errors. We will discuss the source of these errors. We will explain that using a higher order solver, not only will not rectify the problem, but also makes the problem even worse. The MGSM will be derived to minimize these numerical errors. The DRGSM is designed after a GFM counter part. However, it will be shown that it does not provide much benefit over the MGSM. We will also present a very simple to use criterion, which we call ϑ-criterion, to self-check the results obtained using the OGSM results.

In Chapter 4, we will extend the GSM methods to two-dimensional settings for the elastic-elastic solid-solid interactions. We will explain that, in multi-dimensions, the interfacial conditions can vary according to the problem. We will explain two major (and idealized) conditions, namely the no-slip and the perfect slip conditions. The implementation of the GSMs for these conditions will be discussed. It will be shown that the large numerical errors due to the OGSM are also present in the multi-dimensions. Moreover, it will be shown that the ϑ-criterion can also be used in multi-dimensions. Furthermore, in our numerical experiment section of the chapter, we show the method applied to multi-dimensions. We show the comparison of the developed methods against the analytical solution. Moreover, convergence studies and error analysis of the results have been included in the numerical studies.

In Chapter 5, we will develop the GSM methods for the elastic-plastic solid-solid interactions. The discontinuities in elastic-plastic interactions can be more complicated compared to the elastic-elastic interactions. It will be shown, that the OGSM method can lead to large numerical errors for the elastic-plastic interactions just as well. Sometimes, these errors are more severe compared to the elastic-elastic interactions, while at other times they may be less pronounced. In either scenario, the ϑ-criterion can successfully predict the stability or the large numerical errors due to the OGSM. The MGSM method will be derived to minimize these large errors. It is shown that the MGSM can successfully rectify the large numerical errors due to the OGSM.

In Chapter 6, we develop the GSM methods for the elastic-plastic solid-solid interactions in two-dimensional space. We will discuss the details how these methods can be extended to multi-dimensional settings. Moreover, the two idealized interface conditions are studied for the elastic-plastic solid-solid interactions. We will show that the OGSM results can also suffer from large numerical errors for the case of elastic-plastic deformations. The solution obtained using the OGSM, and MGSM results are compared against the results obtained by the method proposed by Zwas [62]. The error analysis and the convergence studies for the numerical experiments in multi-dimension are presented in this chapter. The error analysis shows that the solution obtained using the MGSM is monotonically convergent, however, the accuracy of the results are less than first order.

In Chapter 7, we will summarize the findings in this work. In the end, we provide a series of suggestions for future lines of research based on this work.

Chapter 2

Literature Review

In this chapter, we will present a brief review of the multi-medium problems and the methods generally used to treat the interfacial conditions. We will go over the methods used for multi-medium interactions. Furthermore, we will discuss the strong and weak points of these methods accordingly.

2.1 Coupling Approaches

Various methods have been developed by various researches for solving multi-medium/interfacial problems. These methods may be significantly varied. Schäfer suggested these approaches to be classified as either strong or weak [63, 64].

The term "weak coupling" refers to the partitioned approaches where the solver for each field is independent of the other fields. The coupling is achieved by passing the force and displacement between the solvers back and forth and trying to satisfy the interfacial conditions. This may be done through an iterative predictor-corrector approach. This approach gives the user the flexibility to use the solver of choice for each field.

The term "strong coupling" refers to monolithic approaches where the solver is extensively modified such that the unknowns are calculated simultaneously for all the fields by properly constructing the coupled equations. These methods are usually more stable, with higher convergence rates. However, once implemented, it is not easy to change the solver for each medium. Many approaches have also been proposed that are neither fully monolithic and not completely partitioned: middle-ground approaches that have the advantages of the both mentioned approaches. A schematic of this classification can be seen in Fig. 2.1.

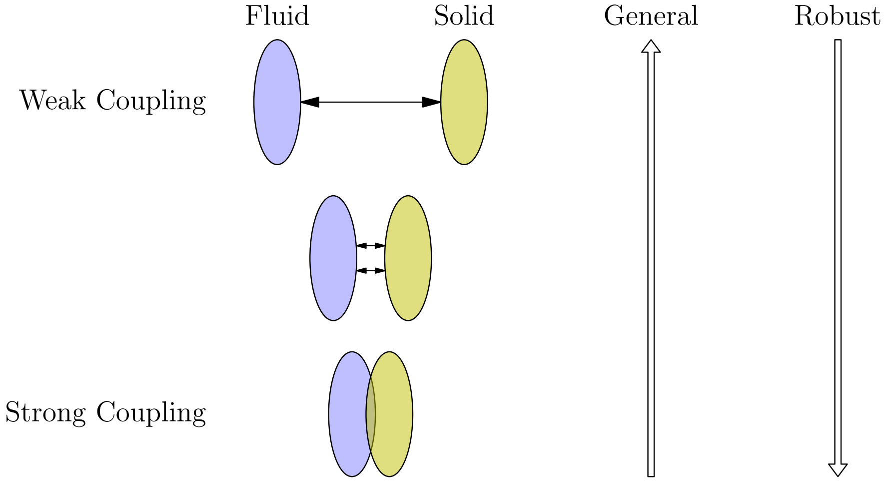

Figure 2.1: A schematic of different coupling approaches and their characteristics.

2.1.1 Weak Coupling Approaches

Weak coupling, or partitioned coupling, approaches are very popular as they allow for the use of separate solver codes on each side of the interface. As a result, these methods provide for a way to use readily available solvers for each field as black-box solvers. This makes them very versatile and can provide significant advantages in improving the efficiency of the computational systems. It is proposed that the partitioned approaches can themselves be categorized into “loose partitioned coupling approaches” versus the “strong partitioned coupling approaches” [65].

Loose partitioned coupling, or sequentially staggered approaches, are referred to the methods that implement a single step solution of each field per time-step. This makes these methods very computationally efficient. For instance, Flippa and Park proposed the formulation and computer implementation of a loose coupling approach for two-field problems governed by semi-discrete second-order coupled differential equations [66]. Their approach can be applied to structure-fluid, structure-soil and structure-structure interactions. However, despite their wider range of applicability and their ease of implementation, it is noticed that these methods can lead to numerical instabilities when the density ratio between the two fields is significantly high. Moreover, it has been shown that these instabilities can depend on the geometry of the solution domain [67–69]. It appears that sequential coupling schemes, even if one uses implicit schemes to solve each field, have an inherent explicit characteristic [65]. Moreover, it has been observed that the instability in these schemes cannot be overcome by reducing the time-step as the instability is inherent to the scheme. This inherent instability has been named ‘artificial added mass effect’ [65]. The reason is that, for the sequentially staggered approaches, the interfacial forces depend on the predicted interfacial displacements, rather than the correct value of the interfacial displacements. Hence, the interfacial forces always suffer from numerical errors which results in the instability of these schemes.

To overcome the instability problems in sequentially partitioned schemes, ‘strong partitioned coupling approaches’ have been introduced. This is achieved by iterating back and forth, between the solvers for each field, to satisfy the interface conditions, in order to achieve higher accuracy and stability in the solution. Karlo and Tezduyar [70] proposed a finite element based method for 3D simulation of fluid-structure interactions. Their fluid solver is based on the stabilized finite element formulation and the structural dynamic solver is based on a Lagrangian description of motion. They solve the non-linear equations iteratively. Wall et al. [71] proposed a strong partitioned coupling approach for FSI problems with free surface. They introduce an implicit partitioned free surface and they embed it in a strong coupling FSI solver. They calculate the elevation by a dimensionally reduced pseudo-structural approach. The stability of their method is comparable to a fully implicit approach. See [21, 72–77] for other works which have attempted to develop various strong partitioned coupled approaches.

2.1.2 Strong Coupling Approaches

Strong partitioned approaches are much more robust and powerful in comparison to the loose partitioned approaches. However, these methods may require substantial numerical effort to obtain a converged solution in the presence of added mass effects [78]. The efforts and the computational needs required for these schemes have motivated the development of monolithic schemes. In these schemes, all the unknowns are solved for, simultaneously. This means that the field solvers can no longer be decoupled. This ensures that the computational requirements are minimal and the methods remain stable.

Heil proposed a monolithic approach for the solution of large-displacement fluids-structure problems by Newton's method [79]. He proposes a block-triangular approximation of the Jacobian matrix. Schur complement is used as the preconditioner for the GMRES solver. He shows that although the suggested preconditioners are not suitable for the Newton method, they act efficiently for the GMRES iterative solver.

Hübner et al. developed a solution procedure for FSI problems [80]. They used the geometrically nonlinear elastodynamics model for the structural field, and assumed the fluid field to be governed by the incompressible

Navier-Stokes. Then, they applied the space-time finite element method to both fields to obtain a uniform discretization. Velocity variables were used as dependent variables for both fields. They used a weighted residual formulation to enforce the interface conditions. Their formulation enabled them to solve the fluid, solid, and interfacial conditions in one single step. They could obtain a very stable solution for strongly nonlinear interactions.

Bazilevs et al. [81] proposed a non-uniform ration B-splines-based isogeometric FSI formulation which couples the incompressible fluids with non-linear elastic-solids. Their formulation is designed to allow for large structural displacements. The resulting formulation is a fully coupled FSI problem which can solve the fluid, structural, and interfacial unknowns in a single step. They have successfully applied their method to problems involving arterial blood flow to simulate the fluid-structure interactions in these problems.

Liu et al. [82] have developed a second-order time accurate scheme for solving FSI problems. They used the so-called Combined Field with Explicit Interface (CFEI) which advances the formulation based on the ALE approach with finite element formulation. They showed that their method is stable for any density ratio. This makes their method specially suitable for problems with strong added mass effects. See [78,83,84,84–87] for more works on the monolithic approaches.

Although monolithic approaches can provide stable solutions for a wide range of multi-medium problems, they require a single-step formulation of the solution of the coupled problem. This does not allow for decoupling of the fields. Consequently, matured solvers cannot be readily employed to be used with monolithic approaches. Moreover, if one has already implemented a certain field setup (e.g. incompressible fluid and elastic solid interaction) it is not easy to change one field for another (e.g. change incompressible fluid into compressible fluid) without changing the entire formulation. Moreover, it is not easy to change the interfacial conditions without changing the formulation itself. This makes the application of the monolithic schemes confined to the problem that they are developed for.

2.1.3 Other Methods

Various attempts have been made to develop methods that are suitable for multi-medium problems and at the same time need are not necessarily fully monolithic or fully-partitioned approaches. This means that the fields are decoupled using special techniques that will make the coupling more stable, and at the same time, satisfy the interfacial conditions as accurately as possible.

Zhang and LeVeque proposed an immersed interface method for the acoustic wave equations with discontinuous coefficients [51]. In this method, the acoustic wave is considered to be traveling through a heterogeneous media. They use high-resolution flux-limiter methods on a Cartesian grid. On the grid points which are far from the interface, standard finite difference methods are used. For the computational cells which the interface passes through them, tailor series expansions are applied and jump conditions are satisfied over the tailor approximations to calculate derivatives and their jumps. This enables them to construct the final discretization scheme. The resulting scheme boasts a second order accuracy even when the interface is not aligned with the grid. However, in order to calculate the coefficients one needs to solve a system of equations. For example, for the acoustic equations in a 2D setting, a system of 54 unknowns needs to be solved. This system of linear equations may also vary according to the jump conditions at the interface which further complicates the method. See [50, 52, 53, 55], for further details on the immersed interface method the.

In 2002, Peskin introduced the Immersed Boundary Method (IBM) for fluid-solid interaction problems [59]. In that work, he develops the IBM for the problems which involve Eulerian as well as Lagrangian variables. In the method motivated by the IBM, the Eulerian variables are considered to exist on a fixed Cartesian grid, while the Lagrangian variables are defined on a curvilinear mesh that can freely move over the Cartesian Eulerian grid. In such problems, the variables are derived from the principal of least action are connected through a Dirac delta function. In the IBM method, the interaction equations are satisfied using a smoothed Dirac delta function which introduces an approximation to the exact solution. Using this method the distinction between the fluid dynamics and the elasticity is blurred. An important feature of the method is that the Eulerian and the Lagrangian grids do not have to be related at all. Which makes this method very desirable for FSI problems.

In 1979, Hirt and Nichols developed the Volume of Fluid (VOF) method based on the concept of the fractional volume of the fluid [34]. VOF can detect intersecting free boundaries automatically. Despite being a conservative method, due to the averaging nature of the VOF, it tends to diffuse the interface. In an attempt to recover the sharpness of the interface the interface reconstruction-VOF method have been developed [48].

In 1982, Fix developed the Phase-Field Method (PFM) [49]. This method was originally developed for the Stefan problems. In this method, an auxiliary phase function is defined which can take two distinct values in each phase. Hence, the interface is implicitly defined by the presence of the phase function. Then, the interface conditions are captured implicitly by introducing a set of partial differential equations to advance the whole system including the phase-function. A characteristic of the phase-field approach is that the phase-function changes smoothly around the interface, and can keep the interface sharp only in the limit.

Level set method [36, 37] has been extensively used [28, 36–46] to preserve the interface sharp. The concept of the Level-set method is that an auxiliary function is defined, were the level-set zero of this function represents the interface in the problem. The interface movement is captured by advancing the auxiliary function which is usually a signed-distance function through a time marching PDE by using the velocity field as the extension velocity. The level-set zero of the problem always represent the location of the interface. This method can keep the interface very sharp, however, it is intrinsically not conservative. Moreover, the level-set function after some time marching, for problems with high deformation looses its quality and needs to be reconstructed.

2.1.4 The Ghost Fluid Methods

In a pioneering work, Fedkiw et al. [2] introduced the Ghost Fluid Method (GFM) for multi-material flows. The GFM can be easily extended to multi-dimensions and be applied to fairly complex geometries. The application of this method is simpler than other competing methods such as the Immersed Interface Method [50–57], or even the Immersed Boundary Method [58–61]. At the same time, the GFM keeps the solver intact like staggered approaches. Due to its inherent simplicity, the GFM became very popular among the research community. To the date of the writing of this dissertation, this pioneering work has been cited over a thousand times by various authors. Subsequently, another version of the method was developed in particular for gas-water flow by Fedkiw [88]; this is nominally referred here to as the gas-water GFM. To facilitate subsequent discussion, the above-mentioned GFM in [2] is referred to here as the original GFM (OGFM) to distinguish it from other modified versions. These characteristic features of OGFM have led to development of similar methods for simulating multi-medium flow [89–92].

Apart from the simplicity, the OGFM appears to be rather problem related. It has been shown that the OGFM is not quite suitable for extreme conditions like the case of high speed jet impact problems and can lead to large numerical errors [93]. This is largely attributed to the fact that the OGFM essentially does not take into account the effect of wave interaction at the interface and the different material properties. To overcome the limitation, Liu et al. [1] proposed the modified GFM (MGFM) algorithm. Subsequent to that, the real GFM (RGFM) was developed by Wang et al. [94] as a variant of MGFM-based algorithm. The latter two MGFMs have been successfully applied to different extreme cases of gas-gas, gas-water, and even fluid-structure problems [1, 44, 93–97]. It is fairly clear that the MGFMs are much less problem-related and can be used much more extensively.

Although as mentioned, there has been various attempts to address the shortcomings of the OGFM through development of modified versions of the GFM, no apparent systematic study of the error, and no criterion for predicting when large errors may occur due to the GFM has been proposed. Moreover, despite the apparent success in the application to the various multi-medium problems, there appears no attempt to explore the applicability of the Ghost Methods to purely solid-solid interaction. These two key factors mostly provide the motivation of the present work.

This work seeks to develop the Ghost Solid Methods (GSMs) to faithfully simulate and capture the boundary conditions at the interface for the elastic-elastic and elastic-plastic solid-solid interaction problems. It shall be shown that this can facilitate a consistent and truly multi-medium modeling of fluid and several layers of solid interaction using ghost nodes.

Moreover, we shall present a simple criterion which can successfully predict the large numerical errors that may occur due to the use of the OGSM. The importance of this criterion, once satisfied, lies in the fact that it can add a level of reliability to the result that are obtained by the much simpler OGSM.

2.2 The Eulerian vs. the Lagrangian Approach

There are two major approaches for modeling solid-solid interactions: using an Eulerian frame of reference, or a Lagrangian frame of reference. The Eulerian framework has the advantage that no regeneration of the mesh is required throughout the computational process. However, the challenge is that all physical boundaries should be somehow tracked through the mesh, as they may not be fixed in this frame [98]. Moreover, tracking the interface needs special attention. This may require the use of level-set methods [36] or any other accurate front tracking techniques [99, 100]. On the other hand, the Lagrangian framework does not require tracking of the boundaries through the mesh. This is due to the fact that the boundaries of the solid are usually Lagrangian points. Moreover, most of the engineering measuring devices for solids, like strain-gages, are attached to the solid considered to be in a Lagrangian framework for ease of reference and comparison. The only possible drawback for the Lagrangian framework is that the computer codes developed under this framework may regularly require mesh regeneration. However, as in work in which the deformations are assumed to be reasonably limited, the necessity for mesh regeneration will be minimal. Therefore, the Lagrangian framework has been used in this work.

Chapter 3

One Dimensional Elastic-Elastic Solid Interactions

In this chapter[1], the one-dimensional elastic solid-solid interaction is investigated. We start with the Original Ghost Solid Method (OGSM), to be followed by two variants in the form of Modified Ghost Solid Method (MGSM) and Double Riemann Ghost Solid Method (DRGSM). The advantages and possible disadvantages of each of these methods are discussed and compared. These numerical methods are then validated and compared using numerical experiments.

---

[1] Part of this chapter has been presented in the 1D section of the journal paper, "*The ghost solid method for the elastic solid-solid interface*" [101] by Kaboudian and Khoo.

3.1 Governing Equation

The Cauchy equation of motion at any point inside a solid can be written in tensor notation as:

$$\rho b_i + \sigma_{ji,j} - \rho a_i = 0 \tag{3.1}$$

where ρ is density of the material, $\overrightarrow{b}$ is the body force, σ is the stress tensor, and $\overrightarrow{a}$ is the acceleration. Considering the body forces are negligible, equation (3.1) can be simplified to

$$\sigma_{ji,j} - \rho a_i = 0. \tag{3.2}$$

For the case of pure shear, in a one dimensional setting, one can further simplify equation (3.2) to

$$\frac{\partial \sigma}{\partial x} - \rho \frac{\partial u}{\partial t} = 0. \tag{3.3}$$

In this work, for the closure of the system, Hooke's law is used as the constitutive equation. For 1D isotropic linearly elastic solid, it can be written as

$$\sigma = E \frac{\partial \varepsilon}{\partial x} \tag{3.4}$$

where ε is the displacement in x-direction, and E is the modulus of elasticity. If equation (3.4) is differentiated with respect to time, this leads to:

$$\frac{\partial \sigma}{\partial t} = E\frac{\partial}{\partial t}\left(\frac{\partial \varepsilon}{\partial x}\right) = E\frac{\partial}{\partial x}\left(\frac{\partial \varepsilon}{\partial t}\right) = E\frac{\partial u}{\partial x} \tag{3.5}$$

since

$$u = \frac{\partial \varepsilon}{\partial t}.$$

By using equations (3.3) and (3.5), the governing equation for pressure wave propagation, in a semi-infinite isotropic linearly elastic solid, can be formulated as

$$\frac{\partial U}{\partial t} + \frac{\partial F(U)}{\partial x} = 0 \tag{3.6}$$

in conservative form, or the following non-conservative form given as

$$\frac{\partial U}{\partial t} + \mathbf{A}\frac{\partial U}{\partial x} = 0 \tag{3.7}$$

where

$$U = \begin{bmatrix} u \\ p \end{bmatrix}, \quad F = \begin{bmatrix} p/\rho \\ Eu \end{bmatrix}, \quad \mathbf{A} = \begin{bmatrix} 0 & 1/\rho \\ E & 0 \end{bmatrix}.$$

Here, u is the velocity in the x-direction, $p = -\sigma$, ρ is the density of the solid, and E is the modulus of elasticity. It is noticed that $c = \sqrt{\frac{E}{\rho}}$ is the speed of sound in the elastic solid [102].

3.2 The Riemann Problem for the Linearly Elastic Solid-Solid Interface

The Riemann problem is given as

$$\frac{\partial U}{\partial t} + \mathbf{A}\frac{\partial U}{\partial x} = 0, \quad U(x,0) = \begin{cases} U_L & x < x_I \\ \\ U_R & x > x_I \end{cases} \tag{3.8}$$

where x_I is a reference length for the problem. For the solid-solid interaction problem, x_I can be considered as the location of the interface. The subscripts L and R refer to the values on the left and right side of the interface, respectively. The subscript I refers to the interfacial values.

The objective is to find the values of $U_I = U(x_I, 0)$. One can now solve the stated Riemann problem as illustrated in Figure (3.1).

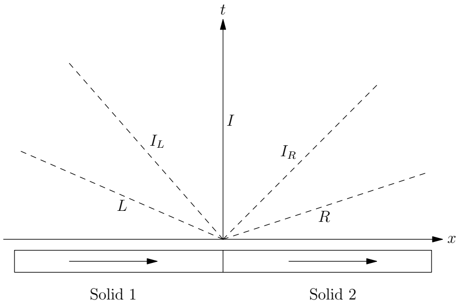

Figure 3.1: Riemann problem in (x, t) plane raised in the impact of two solid rods

In the leftward wave region, the information propagates along the characteristic $x/t = c_L$. Therefore, in this region, the following characteristic equation holds true:

$$\frac{d}{dt}\left(p+\frac{E_L}{c_L}u\right)=0 \quad \Rightarrow \quad dp+\frac{E_L}{c_L}du=0. \tag{3.9}$$

Similarly, in the rightward wave region, the information propagates alongside the characteristic line $x/t = -c_R$. Therefore, in this region, the following characteristic equation can be considered. That is,

$$\frac{d}{dt}\left(p-\frac{E_R}{c_R}u\right)=0 \quad \Rightarrow \quad dp-\frac{E_R}{c_R}du=0. \tag{3.10}$$

Now, one can integrate (3.9) as

$$\int_{p_L}^{p_{I_L}} dp+\frac{E_L}{c_L}\int_{u_L}^{u_{I_L}} du=0 \quad \Rightarrow \quad (p_{I_L}-p_L)+\frac{E_L}{c_L}\left(u_{I_L}-u_L\right)=0 \tag{3.11}$$

and (3.10) as

$$\int_{p_R}^{p_{I_R}} dp-\frac{E_R}{c_R}\int_{u_R}^{u_{I_R}} du=0 \quad \Rightarrow \quad (p_{I_R}-p_R)-\frac{E_R}{c_R}\left(u_{I_R}-u_R\right)=0. \tag{3.12}$$

The subscripts I_L and I_R refer to the interfacial values when integrated on the leftward and rightward wave regions, respectively. With continuity, we have

$$u_{I_L} = u_{I_R} = u_I, \quad p_{I_L} = p_{I_L} = p_I. \tag{3.13}$$

Using (3.11), (3.12), and (3.13), one can derive at the interfacial values u_I and u_L as

$$u_I = \frac{c_L c_R (p_L - p_R) + E_L c_R u_L + E_R c_L u_R}{E_L c_R + E_R c_L} \tag{3.14}$$

and

$$p_I = p_L - \frac{E_L}{c_L}\left(\frac{c_L c_R (p_L - p_R) + E_L c_R (u_R - u_L)}{E_L c_R + E_R c_L}\right). \tag{3.15}$$

This Riemann solver is used below in conjunction with the proposed numerical methods. One key issue is the assignment of the appropriate real values for the leftward and rightward regions, and selection of the (numerical) interface.

3.3 The First Order Godunov Solver for a Homogeneous Elastic Medium

In this section, we will briefly explain the first order Godunov solver [102] for the one dimensional homogeneous elastic solid medium. We start from the governing equation in the conservative form which is:

$$\frac{\partial U}{\partial t} + \frac{\partial F(U)}{\partial x} = 0. \tag{3.16}$$

We assume that the solution at the time step $t = t^n$ is known at every grid point, $1 \leq i \leq N$, where N is the number of grid points. This nodal value is represented by U_i^n. In the finite volume sense, in order to obtain the solution at time step $t = t^{n+1}$, the following discretization can be employed:

$$\frac{U_i^{n+1} - U_i^n}{\Delta t} + \frac{F_{i+1/2} - F_{i-1/2}}{\Delta x} = 0, \tag{3.17}$$

where $F_{i+1/2}$ and $F_{i-1/2}$ are the flux on cell borders. A schematic of this computational cell can be seen in Fig. 3.2. Here, we will discuss the calculation of the numerical flux at $x_{i+1/2}$ with the assumption of a homogeneous medium. In a first order Godunov scheme, the flux at $i + 1/2$ is calculated by assuming that $U_{1+1/2}$ is the solution of the following Riemann problem at $x_{i+1/2}$:

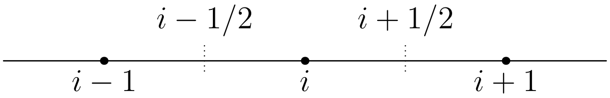

Figure 3.2: Schematics of the nodes $i-1$ to i and the cell boundaries.

$$U^n(x) = \begin{cases} U_i^n & \text{for} \quad x < x_i \\ U_{i+1}^n & \text{for} \quad x > x_i \end{cases}, \qquad \mathbf{A}(x) = \mathbf{A}_i = \mathbf{A}. \tag{3.18}$$

By comparing the above mentioned Riemann problem with the general Riemann problem solved in Sec. 3.2, and after some simple algebraic manipulation, we can obtain the solution at $x_{i+1/2}$ which is

$$u_{1+1/2} = \frac{c(p_i - p_{i+1}) + E(u_i + u_{i+i})}{2E}, \tag{3.19}$$

and

$$p_{i+1/2} = \frac{c(p_i + p_{i+1}) + E(u_i - u_{i+1})}{2c}. \tag{3.20}$$

Now that $U_{i+1/2}$ is determined, we can easily determine the Godunov flux which is

$$F_{i+1/2} = \mathbf{A}U_{i+1/2}. \tag{3.21}$$

Using a similar technique, or simply shifting the subscripts in the above solution, we can obtain $F_{i-1/2}$. For further details on the theory of the Godunov scheme or different implementations of this method, you can refer to the works of Toro [102] or Xiao [62].

3.4 GSM-Based Algorithms

3.4.1 Outline of Various Ghost Solid Methods

For the Ghost Solid Method (GSM)-based algorithms, we shall assume that the solution at time $t = t^n$ is known. In the implementation, usually a band of 2 to 5 grid points is defined as ghost nodes, in the neighbourhood of the solid-solid interface. At each ghost node, ghost solid and real solid are both present. In the GSM-based algorithm for a multi-medium interaction problem, one has to solve for two separate 1-medium Riemann problems at each time step. One is for the left solid medium with the following initial conditions

$$\frac{\partial U}{\partial t} + \mathbf{A}\frac{\partial U}{\partial x} = 0, \quad U(x,0) = \begin{cases} U_L^n & x < x_I \\ \\ U_R^* & x > x_I \end{cases}. \tag{3.22}$$

Here, the '$*$' sign is used to represent the ghost status at $t = t^n$. Equation (3.22) solves the Riemann problem from the first grid node on the left to the ghost node on the right of the interface. Similarly, the other Riemann problem for the right solid medium is given as

$$\frac{\partial U}{\partial t} + \mathbf{A}\frac{\partial U}{\partial x} = 0, \quad U(x,0) = \begin{cases} U_L^* & x < x_I \\ \\ U_R^n & x > x_I \end{cases}. \tag{3.23}$$

It solves from the ghost node on the left of the interface to the last node on the right. To solve the above mentioned (3.22) and (3.23) Riemann problems, it is essential to assign the values of U_R^* and U_L^* on their respective ghost nodes properly. Once these ghost values are defined, at the time step $t = t^n$, any desired solid solver can be used to advance the solution of (3.22) and (3.23) independently.

Depending on the method which is used to define these values on the ghost nodes, various methods of GSM are therefore developed. Three types of GSM-based algorithms are proposed and formulated below. It is worthwhile, however, to reiterate the lemma by Liu et al [103]:

Lemma The GSM Riemann problems (3.22) and (3.23) provide a solution which is identical to that of the Riemann Problem (3.8) in their respective solid fields, provided that their ghost solid states are respectively defined as the exact interfacial states, $U_L^* = U_{I_L}$ and $U_R^* = U_{I_R}$.

3.4.2 On the Original Ghost Solid Method (OGSM)

This method follows the pioneering work by Fedkiw [2, 88] on ghost fluid method. Here, the local real solid velocity and stress are simply copied to the corresponding ghost solid nodes. The Young modulus as well as the speed of sound is copied from the real solid to its corresponding ghost solid node, on the other side of the interface. By assuming that the interface lies between node i and $i+1$, and a band of 3-5 ghost nodes on each side of interface, this method can be formulated as:

$$\begin{array}{lll} U_L^*|_{x=x_j} = U_j^n, & \mathbf{A}_j^* = \mathbf{A}_{i+1}, & i-4 \leq j \leq i \\ U_R^*|_{x=x_j} = U_j^n, & \mathbf{A}_j^* = \mathbf{A}_i, & i+1 \leq j \leq i+5 \end{array} . \tag{3.24}$$

Figure (3.3) illustrates the process of defining the ghost nodes on the right hand side of the interface. The simplicity lies in that no Riemann problem needs to be solved to define the values of ghost nodes. Moreover, no system

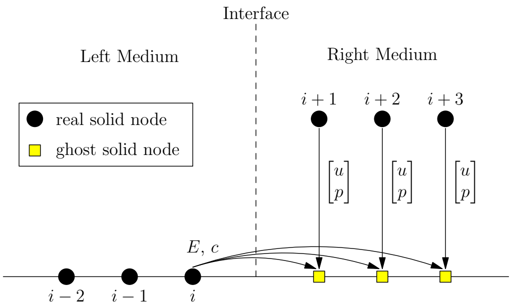

Figure 3.3: Schematic illustration of OGSM for defining ghost solid status for medium 1.

of linear equations need to be solved along with the solid solver in comparison to other methods such as the Immersed Interface Method [51] (the IIM requires solving a system of 12 equations for 12 unknowns in 1D, and 54 equation for 54 unknowns in 2D). However, as will be discussed below, under certain settings it can, and will, result in non-physical oscillations in the velocity as well as the stress waves.

In the following section on numerical experiments, it is shown the OGSM can lead to non-physical oscillations even for first-order methods. It is further demonstrated that these oscillations can become even more severe using the higher order schemes.

3.4.3 On the Modified Ghost Solid Method (MGSM)

Here, we assume the modulus of elasticity and the speed of sound are copied from real solid to its corresponding ghost solid nodes on the other side of the interface. We shall define the ghost node values such that the interfacial values predicted by the left and right single mediums will be identical to that of the multi-medium problem. In other words, we shall ensure the solutions to the problems (3.22) and (3.23) for the interfacial values are identical to those of (3.8).

Considering the left medium and the ghost nodes on the right side of the interface, similar to Section 3.2, characteristic analysis of (3.22) reveals:

$$(p_I - p_L) + \frac{E_L}{c_L}(u_I - u_L) = 0, \tag{3.25}$$

in the leftward wave region, and

$$(p_I - p_R^*) - \frac{E_L}{c_L}(u_I - u_R^*) = 0, \tag{3.26}$$

in the rightward region. u_I and p_I are the interfacial values obtained in Section 3.2. It can be seen that equations (3.25) and (3.11) are identical. Hence, equation (3.25) is automatically satisfied. Moreover, it is clear that equation (3.26) will be satisfied if $u_R^* = u_I$ and $p_R^* = p_I$. Using a similar analysis for the right medium, and the ghost solid nodes on the left side of the interface, we can conclude that $u_L^* = u_I$ and $p_L^* = p_I$.

Now, assuming that the interface lies between the nodes i and $i+1$, the interfacial values of velocity and stress can be approximated by assuming that

$$U_L = U_i^n, \quad U_R = U_{i+1}^n \tag{3.27}$$

and similarly

$$\mathbf{A}_L = A_i, \quad \mathbf{A}_R = \mathbf{A}_{i+1} \tag{3.28}$$

as in Section 3.2. The approximate interfacial values of u_I and p_I can be calculated using equations (3.14) and (3.15) as

$$u_I = \frac{c_i c_{i+1}(p_i^n - p_{i+1}^n) + E_i c_{i+1} u_i^n + E_{i+1} c_i u_{i+1}^n}{E_i c_{i+1} + E_{i+1} c_i} \tag{3.29}$$

$$p_I = p_i^n - \frac{E_i}{c_i} \left(\frac{c_i c_{i+1}(p_i^n - p_{i+1}^n) + E_i c_{i+1}(u_{i+1}^n - u_i^n)}{E_i c_{i+1} + E_{i+1} c_i} \right). \tag{3.30}$$

Therefore, the ghost nodes can be defined as:

$$\begin{aligned} U_L^*|_{x=x_j} &= U_I, \quad \mathbf{A}_j^* = \mathbf{A}_{i+1}, \quad i-4 \le j \le i \\ U_R^*|_{x=x_j} &= U_I, \quad \mathbf{A}_j^* = \mathbf{A}_i, \qquad i+1 \le j \le i+5 \end{aligned} . \tag{3.31}$$

Figure 3.4 illustrates the method schematically. One may note that the same values of u_I and p_I are used for both the left and right ghost nodes. This means that only a single Riemann problem needs to be solved in order to define the ghost node values.

By numerical experiment, it will be shown that this method can greatly mitigate or effectively eliminate the non-physical oscillations seen for the OGSM. The disadvantage of this method vis-a-vis the OGSM is that it

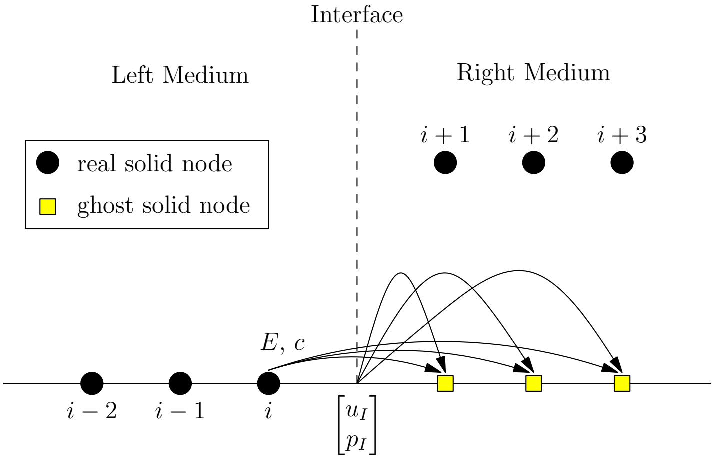

Figure 3.4: Schematic illustration of MGSM for defining the ghost solid on the right side of the interface

involves solving for a Riemann problem at the interface.

3.4.4 On the Stability of the OGSM and MGSM

For the instability of the numerical solution to be caused by, or associated with, the use of the GSMs, and not by the solid solver of choice, the leading numerical error must be traced to the implemented GSMs. Here, we will follow the Lax-Richtmyer stability analysis [104, 105].

As the effects of the GSMs are sensed closest to the interface at each time step, it is reasonable to assume that the maximum error, due to the GSMs, may occur at the interface. As discussed in Section 3.4.3, if the MGSM is employed, U_I from the MGSM and the multi-medium solution will be identical. Hence, the error incurred due the MGSM will be theoretically zero, if the exact solution of the Riemann problem is used. Consequently, the stability of the solution will be unconditionally associated with the stability of the single medium solver employed; i.e. $||E^n||_\infty$ will not be determined by the use of MGSM. Similarly, we can conclude if an approximate Riemann solver is used, the stability of the solution will be determined by both the approximate Riemann solver and the single medium solver employed together with the MGSM.

However, if the OGSM is employed, the interfacial values calculated, from the left and right mediums, are not necessarily identical to those of the exact solution of the multi-medium problem. Using the ghost solid-values, and the multi-medium Riemann problem values, the error in velocity, at the interface, for the left medium is:

$$\begin{aligned} |E_{u_{I_L}}| = \; & \left| \left(\tfrac{c_R c_L}{E_L c_R + E_R c_L} - \tfrac{c_L^2}{2E_L c_L} \right) (p_L - p_R) + \right. \\ & \left(\tfrac{E_L c_R}{E_L c_R + E_R c_L} - \tfrac{1}{2} \right) u_L + \\ & \left. \left(\tfrac{E_R c_L}{E_L c_R + E_R c_L} - \tfrac{1}{2} \right) u_R \right| . \end{aligned} \tag{3.32}$$

As it can be seen, the above error has no upper bound in general. We can obtain similar relations for stress in the left medium. Moreover, we can obtain similar results for the right medium. This means that the error due to the use of the OGSM can be generally unbounded and lead to instabilities. In other words, $||E^n||_\infty$ may be determined by and associated with the error incurred by the OGSM. These large errors may become evident in the form of spurious oscillations, or complete instabilities in the solution, even when a first order solid solver is used. Higher order schemes may tend to switch to lower order schemes, specifically a first order scheme, which is required by the Godunov theorem, to avoid spurious oscillations [102] in the presence of large discontinuities. As a result, the use of a higher order scheme, may not be successful in rectifying the instabilities caused by the use of the OGSM.

If we want to minimize this error for the OGSM, we derive at the special case of the acoustic impedance matching where the error given by (3.32), and equivalents of it, will become zero and the stability becomes synonymous with the stability of the solid solver employed for the single medium. In this special case, the calculated interfacial values from the left and right medium become identical to those of the multi-medium problem. Moreover, it will be the only case where the interfacial values from the left and right mediums become identical. The special case of the acoustic impedance matching and its stable characteristics can be used as reference and guide to predict the stability of the (more general) OGSM. To quantify, a much simpler dimensionless parameter, ϑ, (than that of equivalents of (3.32) made applicable for both velocity and stress) is proposed:

$$\vartheta = \max\left(\frac{|u_{IL} - u_{IR}|}{|u_{IL}| + |u_{IR}|}, \frac{|p_{IL} - p_{IR}|}{|p_{IL}| + |p_{IR}|}\right) \tag{3.33}$$

where the subscript IL and IR refer to the interfacial values obtained from the left and right single medium solutions, respectively. The ϑ value quantifies how close the numerical situation is to the acoustic impedance matching case. Our extensive numerical tests indicate that the maximum permissible value of ϑ, before non-physical oscillations are observed, is $\vartheta_{crit} \approx 0.1$. The above discussion not only explains the origin/reason for possible non-physical oscillations, but also provides a means forward to determine the applicability of the OGSM. For the latter, one can ascertain beforehand if ϑ is within the permissible range to ensure the non-physical oscillations are kept to an acceptable level as time progresses. If at any time step ϑ exceeds the value of 0.1, the OGSM as applied to across the interface can no longer be considered as a viable approach at that time step. One may then need an alternative GSM at that time step. Subsequently, if the value of ϑ drops below 0.1, the OGSM can be reinstated for use due to its simplicity.

It is worth noting that calculation of ϑ is not computationally expensive, specially, if a TVD solver is used; the first order fluxes may be readily available to calculate ϑ.

3.4.5 On the Double Riemann Ghost Solid Method (DRGSM)

This is a variant of the MGSM. A similar variant MGFM was recently developed by Liu et al. [103] to capture the fluid-solid interaction due to very strong shock impacting the interface in the Eulerian-Lagrangian coupling. Here, instead of solving a single Riemann problem at the interface, a separate Riemann problem is defined and solved for each side of the interface.

To obtain the ghost values on the ghost nodes, one has to solve the approximate Riemann problem by assuming that the interface lies on the ghost node just beside the actual interface. This interface can be referred to as a ghost interface. Next, using the real values of its neighbouring nodes a Riemann problem is formulated. As soon as this Riemann problem is solved for the ghost node that lies just beside the interface, the values of $U = [u \quad p]^T$ on this node can be copied to its corresponding ghost nodes.

Similar to Section 3.4.3, it is assumed that the actual interface lies between the nodes i and $i + 1$. To obtain the values of U_R^*, in (3.8), the following Riemann problem is defined:

$$\frac{\partial U}{\partial t} + \mathbf{A}\frac{\partial U}{\partial x} = 0, \quad U(x, t = t^n) = \begin{cases} U_i^n & x < x_{i+1} \\ \\ U_{i+2}^n & x > x_{i+1} \end{cases}. \tag{3.34}$$

The physical properties of problem (3.39) are defined as

$$\mathbf{A}(x) = \begin{cases} \mathbf{A}_i & x < x_{i+1} \\ \\ \mathbf{A}_{i+2} & x > x_{i+1} \end{cases}. \tag{3.35}$$

Figure 3.5 illustrates the position of the ghost interface as well as the closest ghost node to the actual interface. One can then solve for the values of u and p on the node $i + 1$. By comparing equations (3.34) and (3.35) with

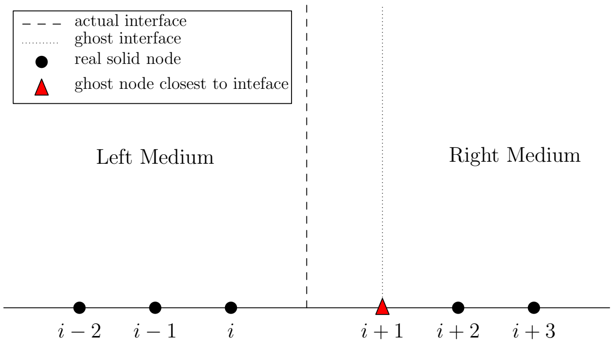

Figure 3.5: Schematic illustration of position of the ghost interface and the ghost node closest to the interface in order to define the ghost nodes on the right hand side of the interface for Medium 1.

the problem (3.8), one can solve for the solution at the ghost interface:

$$u_{I_R} = \frac{c_i c_{i+2}(p_i^n - p_{i+2}^n) + E_i c_{i+2} u_i^n + E_{i+2} c_i u_{i+2}^n}{E_i c_{i+2} + E_{i+2} c_i} \tag{3.36}$$

and

$$p_{I_R} = p_i^n - \frac{E_i}{c_i}\left(\frac{c_i c_{i+2}(p_i^n - p_{i+2}^n) + E_i c_{i+2}(u_{i+2}^n - u_i^n)}{E_i c_{i+2} + E_{i+2} c_i}\right) \tag{3.37}$$

where the index I_R refers to the values on the ghost interface applicable on the node on the right side of the interface. In this setting, this index refers to the ghost interface at the location $x = x_{i+1}$. Using these values, one can then properly define values for the rest of the ghost nodes on the right side:

$$U_R^*\big|_j = \begin{bmatrix} u_{I_R} \\ \\ p_{I_R} \end{bmatrix}, \quad \mathbf{A}_j = \mathbf{A}_i \qquad i+1 \leq j \leq i+5 \ . \tag{3.38}$$

Similarly, one can then define the following Riemann problem for the node just on the left side of the interface. Assuming that the ghost interface lies on the node i, we have

$$\frac{\partial U}{\partial t} + \mathbf{A}\frac{\partial U}{\partial x} = 0, \quad U(x, t = t^n) = \begin{cases} U^n_{i-1} & x < x_i \\ \\ U^n_{i+1} & x > x_i \end{cases} \tag{3.39}$$

and the material properties as

$$\mathbf{A}(x) = \begin{cases} \mathbf{A}_{i-1} & x < x_i \\ \\ \mathbf{A}_{i+1} & x > x_i \end{cases}. \tag{3.40}$$

Therefore, by comparing (3.39) and (3.40) with (3.8) one can get the solution for the ghost interface at $x = x_i$:

$$u_{I_L} = \frac{c_{i-1}c_{i+1}(p^n_{i-1} - p^n_{i+1}) + E_{i-1}c_{i+1}u^n_i + E_{i+1}c_{i-1}u^n_{i+1}}{E_{i-1}c_{i+1} + E_{i+1}c_{i-1}} \tag{3.41}$$

and

$$p_{I_L} = p^n_{i-1} - \frac{E_{i-1}}{c_{i-1}} \left(\frac{c_{i-1}c_{i+1}(p^n_{i-1} - p^n_{i+1}) + E_{i-1}c_{i+1}(u^n_{i+1} - u^n_{i-1})}{E_{i-1}c_{i+1} + E_{i+1}c_{i-1}} \right) \tag{3.42}$$

where the subscript I_L refers to the ghost interface on the left hand side of the real interface. Next, these values are copied to the ghost nodes on the left hand side of the interface:

$$U_L^*\big|_j = \begin{bmatrix} u_{I_L} \\ p_{I_L} \end{bmatrix}, \quad \mathbf{A}_j = \mathbf{A}_{i+1} \qquad i-4 \leq j \leq i. \tag{3.43}$$

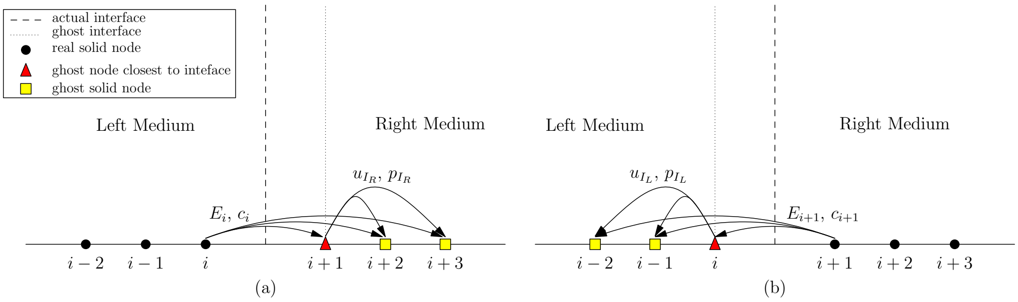

Figure 3.6: Schematic illustration of the definition of the ghost properties in DRGSM method, for **(a)** the ghost nodes on the right side of the interface, and **(b)** the ghost nodes on the left hand side of the interface

Figure 3.6 shows schematically how the ghost properties are copied to the ghost nodes on the right and left side of the interface.

3.5 Numerical Experiments

Numerical experiments below will show that DRGSM is able to eliminate the non-physical oscillations which occur for the GSM. However, comparing to the MGSM and GSM, this method is more complicated and involved. Numerical experiments will also show that the improvements are not so significant when compared to MGSM, despite the greater effort required.

In the following numerical experiments, all computations are carried out in non-dimensional form and the solid mediums on each side of the interface are considered to be homogeneous, isotropic, and linearly elastic solids.

3.5.1 Test Example 1: On Possible Non-Physical Oscillations on the Use of OGSM and the Critical ϑ Value

This experiment is designed to show the non-physical oscillations which may rise due to the use of the OGSM. Moreover, as a test example, it indicates broadly how the critical permissible ϑ value of 0.1 has been determined. The domain of the solution is $[0, 10]$ and the interface is located at $x_I = 5$. The initial velocity $u(x, 0) = 1$ for $x \in [0, 5]$ and zero otherwise, and the initial normal stress $p(x, 0)$ is zero for all x. The boundary conditions are $u(0, t) = 1$ and $u(10, t) = 0$.

Two sets of material properties are assumed:

1. $\rho_L = 1$, and $E_L = 1$ on the left hand side of the interface, and $\rho_R = 1.4$ and $E_R = 1.4$ on the right side are;
2. $\rho_L = 1$, and $E_L = 1$ on the left hand side of the interface, and $\rho_R = 5$ and $E_R = 5$ on the right side;

The first-order Godunov method is used as the solid solver for each solid medium with the spatial discretization of $\Delta x = 0.01$. The maximum CFL

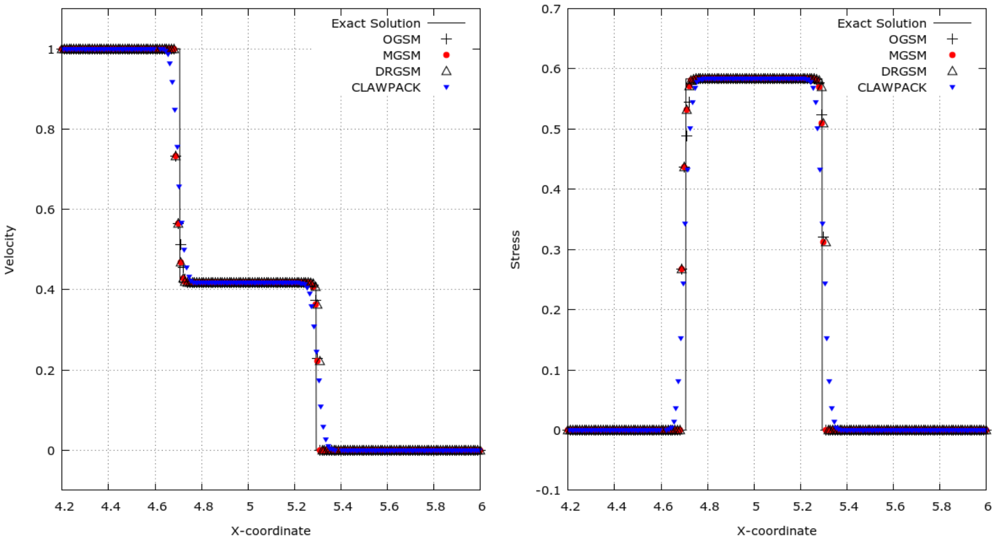

Figure 3.7: Test Example 1: Comparison of the velocity and stress profiles between the exact solution, OGSM, MGSM, DRGSM and CLAWPACK ($\rho_L = 1$, $E_L = 1$, $\rho_R = 1.4$, $E_R = 1.4$, and $t_f = 0.3$)

number [61] is considered to be ($c_{max}\Delta t/\Delta x = 0.98$).

Figure 3.7 to shows the velocity and stress profile for the first set of materials at $t_f = 0.3$, calculated using the OGSM, MGSM, and DRGSM. The results are compared against the analytical as well as the CLAWPACK [106] solution. The calculated value of ϑ (introduced in Section 3.4.4) for this problem when the OGSM is employed reaches a maximum value of 0.09 and remains below 0.1 (the proposed critical value ϑ_{crit}) for all time steps. The results for the OGSM concur well with the analysis and there is no observed oscillation in the velocity and stress predictions.

Figure 3.8 shows the solution obtained for the second set of data at $t_f = 0.3$. For almost all the time steps, the calculated value of ϑ when the OGSM is employed varies between 1.0 and 0.1. Thus, it exceeds the proposed critical value of 0.1 employed to avoid any non-physical oscillation.

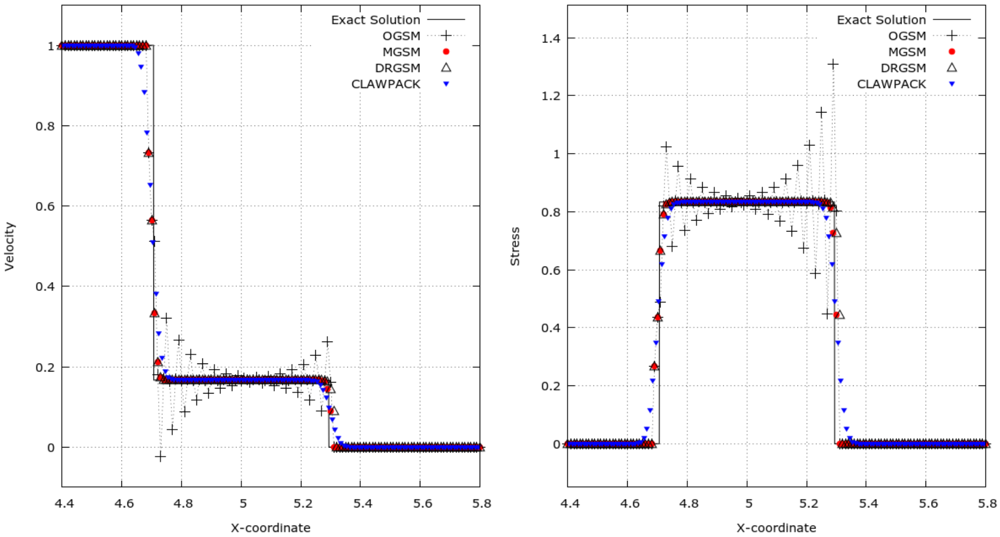

Figure 3.8: Test Example 1: Comparison of the velocity and stress profiles between the exact solution, OGSM, MGSM, DRGSM, and CLAWPACK ($\rho_L = 1$, $E_L = 1$, $\rho_R = 5$, $E_R = 5$, and $t_f = 0.3$)

In Figure 3.8, the employment of OGSM has lead to severe non-physical oscillation in the stress and velocity distributions. However, these oscillations are completely removed when either MGSM or DRGSM is employed. It is interesting to note that the MGSM and DRGSM, in Figures 3.7 and 3.8, enable a better concurrence with the analytical solution compared to the solution from CLAWPACK [106].

This test indicates the applicability of the ϑ-criterion as well as the maximum permissible value of ϑ. It shows how the combination of the material properties of the interacting solids can lead to non-physical oscillations when the OGSM is employed. We have carried out numerous other tests for various material properties and shock conditions and found that the proposed critical value of $\vartheta \approx 0.1$ serves as a good guide to determine if the application of the OGSM will likely lead to non-physical oscillations.

3.5.2 Test Example 2: On the Effect of the Incident Wave

This experiment is designed to show the non-physical oscillations which may rise due to the effect of an incident wave on the interface when one applies the OGSM. Moreover, it indicates the robustness of the ϑ-criterion and the applicability of the $\vartheta_{crit} \approx 0.1$.

The domain of the solution is $[0, 10]$ and the interface is located at $x_I = 5$. The material properties of the mediums are $\rho_L = 1$ and $E_L = 1$ on the left hand side of the interface, and $\rho_R = 5$ and $E_R = 5$ on the right side. The spatial discretization is $\Delta x = 0.5$ and the maximum CFL number is 0.99. The initial condition for this problem is $p(x, 0) = u(x, 0) = 0$. The boundary conditions are p(10,t)=0 and

$$p(0,t) = \begin{cases} t/t_r & 0 \leq t \leq t_r \\ 1 & \text{otherwise} \end{cases} \tag{3.44}$$

where two cases of the reference time $t_r = 0.1$ and $t_r = 0.2$ are considered. The solution is obtained for the final time $t_f = 8$. Figure 3.9 shows the stress and velocity profiles with the reference time of $t_r = 0.2$ in eqn (3.44). The ϑ parameter, when the OGSM is employed, is always below $\vartheta_{crit} \approx 0.1$ for all the time steps, except for only three time steps that reaches a maximum of 0.5 at $t = 5$ when the wave impacts on the interface. After

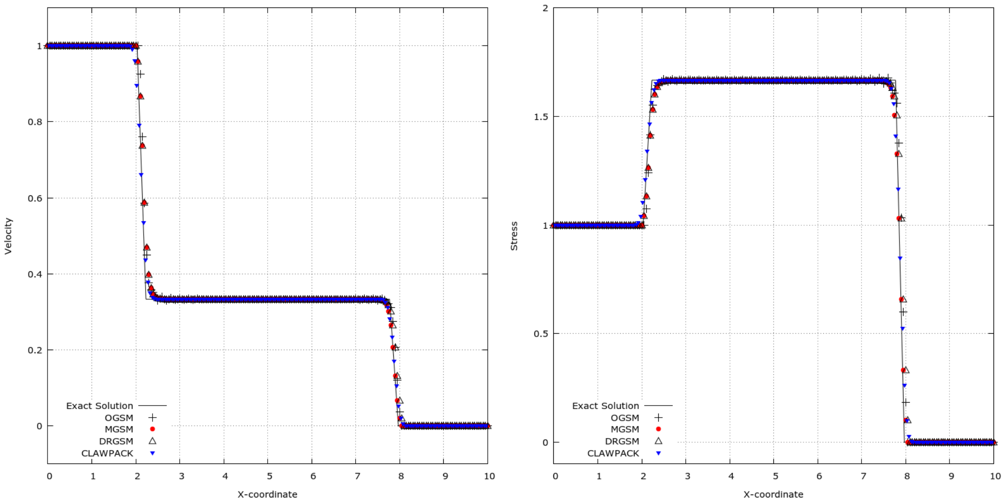

Figure 3.9: Test Example 2: Comparison of the velocity stress profiles between the exact solution, OGSM, MGSM, DRGSM, and CLAWPACK ($\rho_L = 1$, $E_L = 1$, $\rho_R = 5$, $E_R = 5$, the final time $t_f = 8$, and reference time of $t_r = 0.2$.)

these three time steps, ϑ quickly drops below $\vartheta_{crit} \approx 0.1$. Although there are no apparent non-physical oscillations in the OGSM solutions of velocity and stress profile, the above mentioned three time steps have led to a perceptible numerical error in the velocity and stress profile when compared against the exact solution. The MGSM and DRGSM solutions remain stable, and have a good agreement with the analytical solution as well as CLAWPACK.

Figure 3.10 shows the stress and velocity profiles with the reference time of $t_r = 0.1$ in eqn (3.44). The ϑ parameter, when the OGSM is employed, is always below $\vartheta_{crit} \approx 0.1$ for all the time steps until $t = 5$ when the wave impacts on the interface. Then, it spikes to 0.5 and then increases to 0.55 and slowly descends below $\vartheta_{crit} \approx 0.1$ after 11 time steps. This figure indicates severe oscillations in the stress and velocity

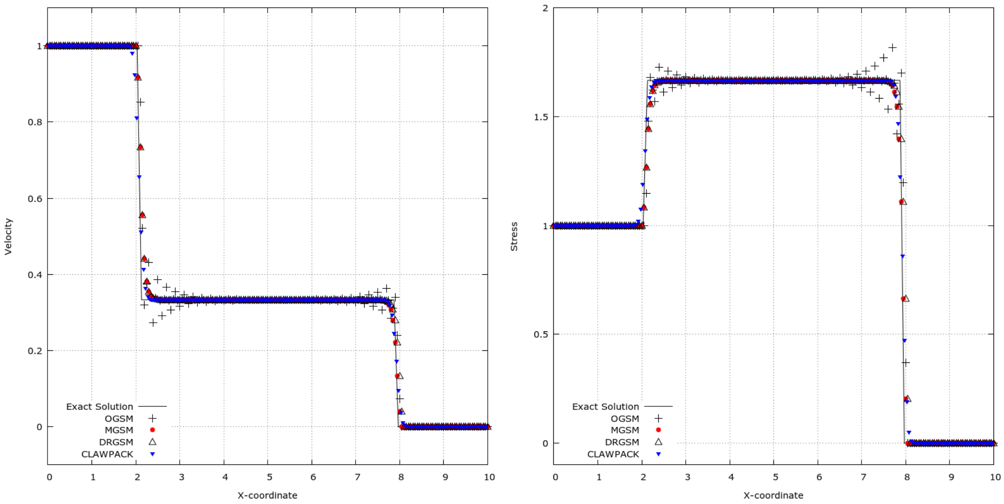

Figure 3.10: Test Example 2: Comparison of the velocity and stress profiles between the exact solution, OGSM, MGSM and DRGSM ($\rho_L = 1$, $E_L = 1$, $\rho_R = 5$, $E_R = 5$, the final time $t_f = 8$, and reference time of $t_r = 0.1$.)

profiles when the OGSM is employed. The MGSM and DRGSM solutions remain stable. Moreover, they concur well with analytical solution and CLAWPACK. These test examples show the importance of the impacting wave, on the interface, on the non-physical oscillations that may rise due to the employment of the OGSM. Moreover, it indicates the applicability and robustness of the ϑ-criterion. It is worth mentioning that we have carried out many more tests for various material properties and various types of waves impacting the interface and found that the proposed critical value of $\vartheta \approx 0.1$ serves as a good guide to determine if the OGSM leads to oscillations.

3.5.3 Test Example 3: On the Effect of Solver

This numerical experiment is designed to compare the effect of the solver on the results obtained by OGSM and MGSM. The domain of the solution is $[0, 10]$ and the interface is located at $x_I = 5$. The initial velocity and stress $u(x, 0)$ is 1 for $x \in [0, 5]$ and zero otherwise. The boundary conditions are $p(0, t) = 1$ and $p(10, t) = 0$. The material properties on the left hand side of the interface are $\rho_L = 1$, and $E_L = 1$, and on the right side are $\rho_R = 5$ and $E_R = 10$. The spatial discretization is $\Delta x = 0.01$. The solution is obtained for $t_f = 0.3$. Firstly, the first-order Godunov is used as the solver. Next, the second-order MUSCL solver [102, 107] is used. Then, the obtained results are compared for these two solvers.

It is noticed that the maximum calculated value of ϑ for this problem is close to 1.0 and far exceeds the $\vartheta_{crit} \approx 0.1$. It can be seen, in Figure 3.11, that using OGSM leads to non-physical oscillations in the stress and velocity profiles. Furthermore, it is noticed that using the higher order method in fact intensifies the non-physical oscillations associated with the OGSM method.

It is clear that the order of the numerical solver does not affect the inherent characteristics of the OGSM. Figure 3.12 shows that even as the order of accuracy of the solver is increased, the MGSM continues to remain stable with a solution which concurs well with the analysis.

Finally, when no GSM is used (i.e. the boundary conditions are applied

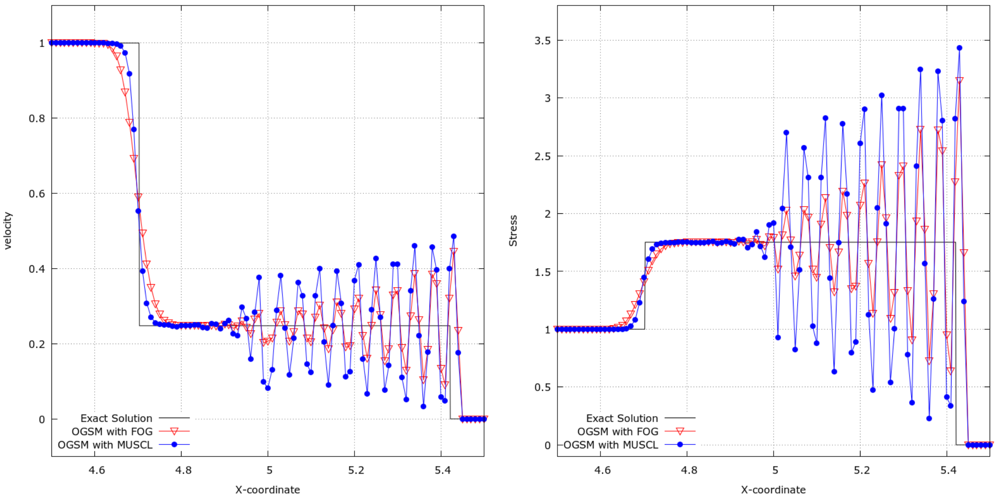

Figure 3.11: Test Example 3: Velocity and normal stress profiles obtained using OGSM (at $t_f = 0.3$).

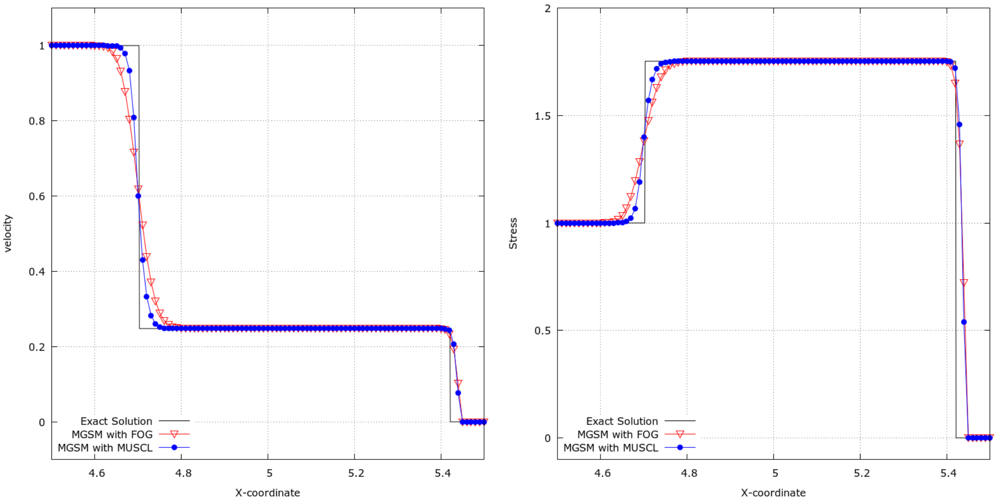

Figure 3.12: Test Example 3: Velocity profile obtained using MGSM (at $t_f = 0.3$).

directly) with the specified CFL number, both the first order Godunov and the MUSCL solver will become completely unstable. The order of maximum numerical error for velocity and normal stress will be 10`E`11 to 10`E`12.

3.5.4 Under the Special Case of Acoustic Impedance Matching Conditions

The acoustic impedance or the characteristic acoustic impedance is a material property defined as

$$Z = \rho c. \tag{3.45}$$

If the acoustic impedance of two different materials is the same, the incident wave at the interface of the materials in contact should just pass through, without any reflection at the interface [16].

Moreover, for elastic solid-solid interactions under the acoustic impedance matching conditions, if the ϑ value is calculated analytically, it is found that $\vartheta = 0$ regardless of the shock wave conditions hitting the interface. Therefore, it is interesting to test the validity of the OGSM as applied to the two numerical problems with matched acoustic impedance shown below in Test Exmple 3. Likewise, it would be interesting to see how the MGSM and DRGSM perform.

The material properties of the two mediums are $\rho_L = 1$ and $E_L = 1$ for the left solid and $\rho_R = 2$ and $E_R = 0.5$ for the right medium. Hence, both the left and right mediums have a unit acoustic impedance. The domain of the solution

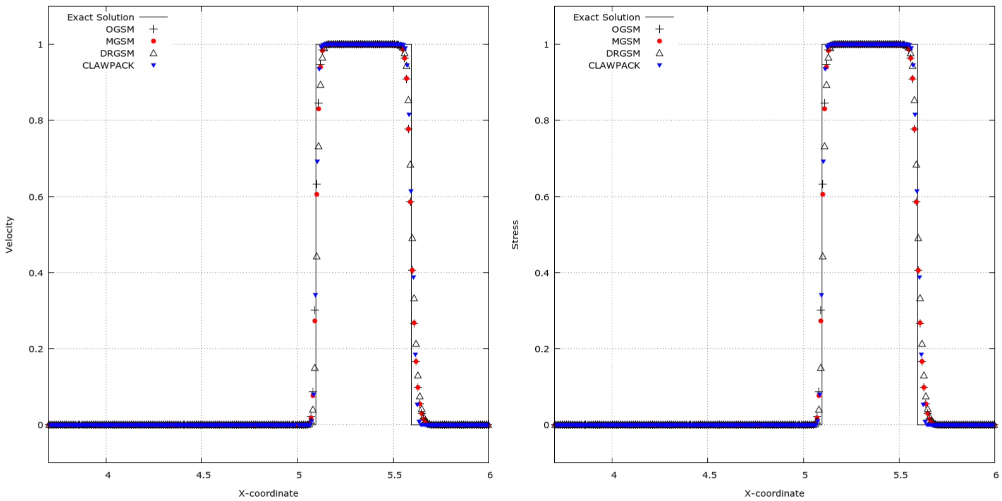

Figure 3.13: Test Example 4: Velocity and stress profile obtained using a MUSCL solver together with OGSM, MGSM, DRGSM, and a second order CLAWPACK solver (at $t_f = 1.2$).

is $x \in [0, 10]$ and the interface is at $x_I = 5$. GSMs are applied and a second order MUSCL solver is used to solve for the elastic solid governing equation.

Test Example 4: A unit pulse hitting the interface

The initial conditions for this case are:

$$u(x,0) = p(x,0) = \begin{cases} 1 & 4 \leq x \leq 5 \\ 0 & \text{otherwise} \end{cases},$$

and the boundary conditions case are $p(0,t) = p(10,t) = 0$. The solution is obtained for $t_f = 1.2$. The grid size is $\Delta x = 0.01$.

The calculated value of ϑ remains identically zero for all the time steps, which is less than $\vartheta_{crit} \approx 0.1$. From Figure 3.13, it is clear that all the wave energy passes through unimpeded and that no wave is reflected at the interface. All the proposed GSMs remain stable and are actually successful, in properly capturing

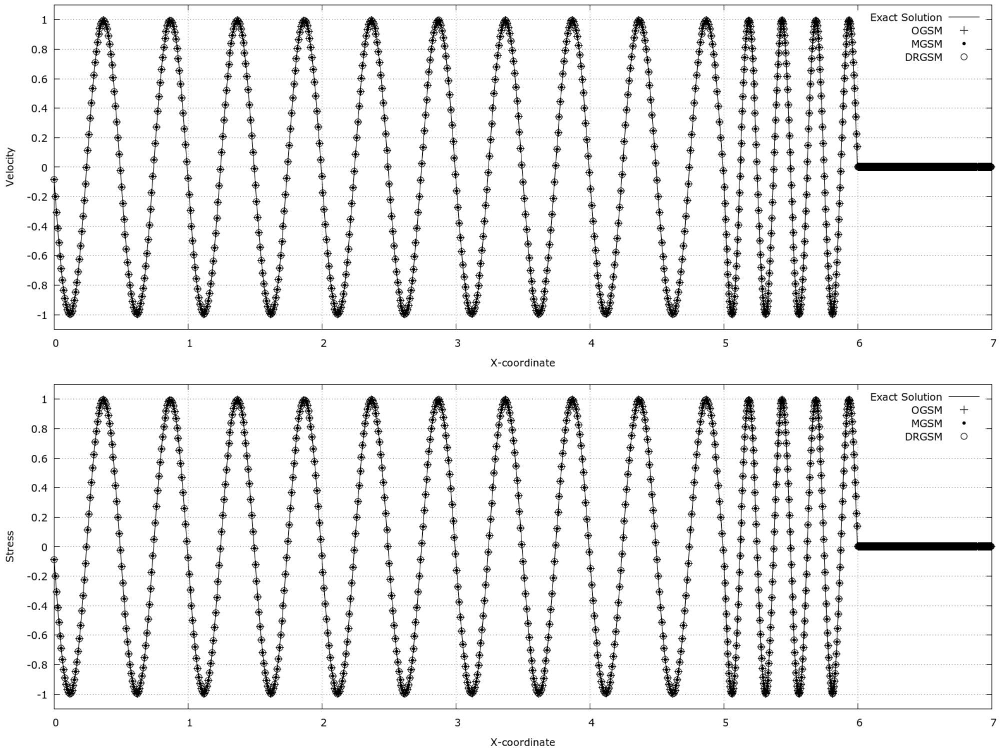

Figure 3.14: Test Example 5: Velocity and stress profile obtained using a MUSCL solver together with OGSM, MGSM, and DRGSM (at $t_f = 7$).

the solid-solid interaction, in this acoustic impedance matching test.

Test Example 5: A sinusoidal wave hitting the interface

The initial conditions for this case are $p(x, 0) = u(x, 0) = 0$, and the boundary conditions for this case are $p(0, t) = sin(4\pi t)$ and $p(10, t) = 0$. The grid size is $\Delta x_L = 0.02$ and $\Delta x_R = 0.01$, for the left and right medium, respectively. The solution is obtained for $t_f = 7$.

In this experiment, the calculated value of ϑ remains identically zero for all the time steps, which is less than $\vartheta_{crit} \approx 0.1$. Figure 3.14 clearly indicates that no non-physical oscillation is observed for any of the proposed GSMs. Furthermore, it is noted that all the wave energy passes through and no wave is reflected at the interface. The proposed GSMs are successful in properly capturing the solid-solid interaction.

3.5.5 Test Example 6: On a general wave propagation

The material properties of the interacting mediums are $\rho_L = 1$ and $E_L = 1$ for the left solid and $\rho_R = 4$ and $E_R = 2$ for the right medium. The initial conditions for this case are $p(x,0) = u(x,0) = 0$. The boundary conditions for this case are

$$p(0,t) = \begin{cases} 0.2 & t \leq 1 \\ 0.8t - 0.6 & 1 < t \leq 2 \\ 1 & 2 < t \end{cases}.$$

$$p(10,t) = 0$$

GSMs are applied and second order MUSCL solver is used to solve for the elastic solid governing equation. The grid size is $\Delta x = 0.04$, the CFL number is 0.98, and the solution is obtained for $t_f = 8$.

The calculated value of ϑ for this experiment is either less than 0.1 or close to zero for almost all time steps, except only for only five time steps at $t = 5$ that reaches a maximum of 0.31 which is greater than $\vartheta_{crit} \approx 0.1$. Since the shocks which hit the interface are not very strong and there is supposedly adequate numerical viscosity to damp out these non-physical oscillations, ϑ quickly falls below $\vartheta_{crit} \approx 0.1$ for the rest of the temporal calculations. Figure 3.15 at $t_f = 8$ shows that although the oscillations are no longer apparent, the numerical inaccuracies introduced when ϑ exceeds 0.1 at the mentioned time steps, have

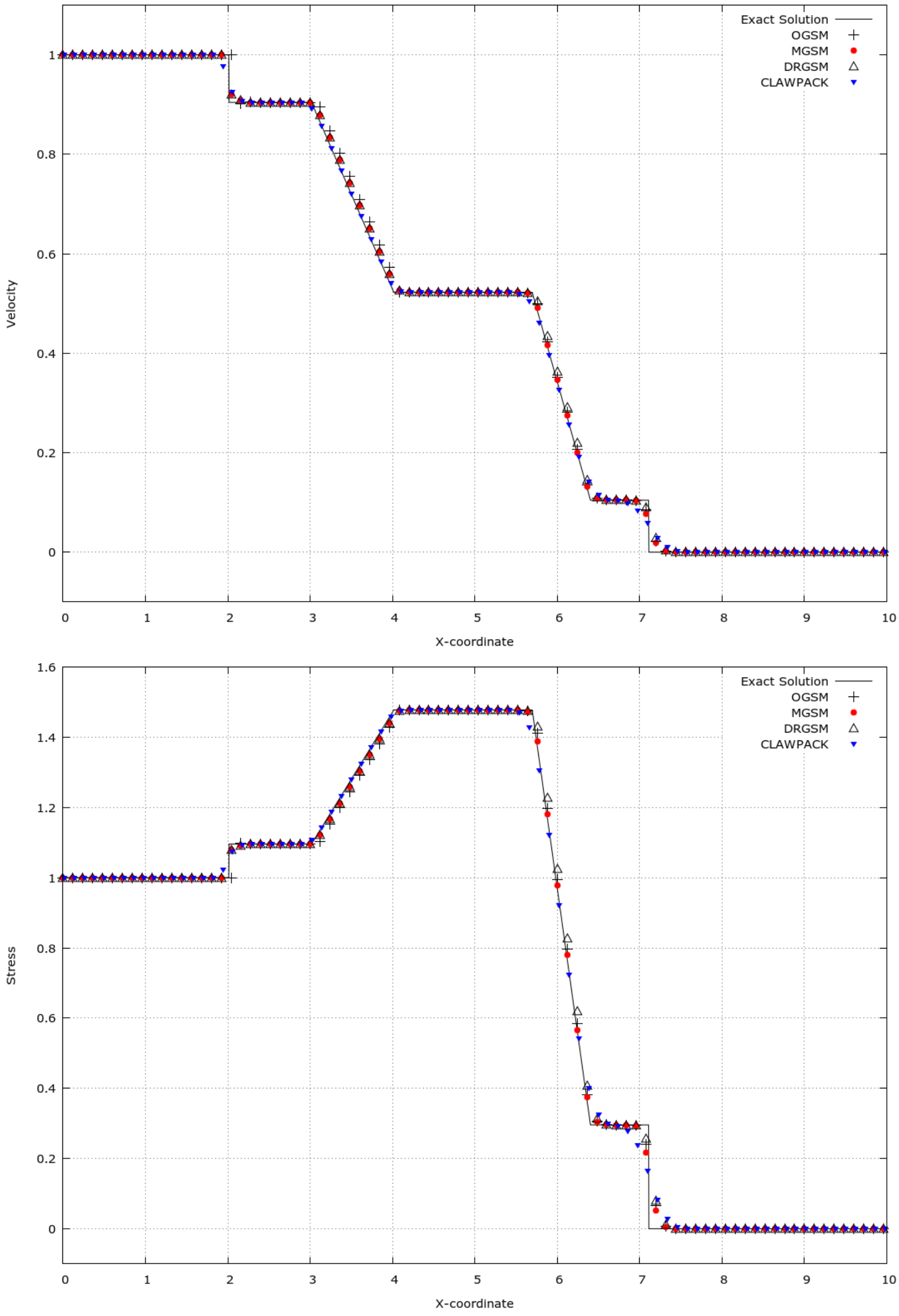

Figure 3.15: Test Example 6: Velocity and stress profile obtained using a MUSCL solver together with OGSM, MGSM, DRGSM, and CLAWPACK (at $t_f = 8$) with the grid size $\Delta x = 0.04$. Only, every third grid point is plotted to show the difference between the OGSM and MGSM results.

led to slightly less accurate solution than the MGSM (where no oscillation is found throughout) in comparison to the analytical solution. In this figure, where the DRGSM is employed, it can provide more accurate results for the reflected waves similar to MGSM compared to the OGSM. Still, the DRGSM can result in a slightly yet perceptible time lead as the wave passes through the interface (see Figure 3.15). Moreover, in the vicinity of large discontinuities in the solution, it is observed that all the GSMs concur slightly better with the exact solution compared to CLAWPACK.

3.6 Conclusion for Chapter 3

Three variants of the ghost solid method were developed for the elastic-elastic solid-solid interactions. It was discussed that these methods are all considerably simple to implement, and they keep the solid solver intact.

It was shown that the Original Ghost Solid Method (OGSM) is the simplest variant of the GSMs to implement. No Riemann problem at the interface needs to be solve for this method. However, it was discussed that the OGSM is a highly problem related method which can, and will, lead to large numerical errors. Various cases that OGSM can fail were studied. The source of these errors were studied, and subsequently, ϑ-criterion was proposed as a means to detect these errors, for all these cases. This criterion also serves as a measure of reliability of the OGSM results. It was discussed that if the ϑ values remains below an empirical critical value of $\vartheta_{crit} = 0.1$, the results obtained using the OGSM are considered reliable. Otherwise, the result may suffer from large numerical errors.

Undoubtedly, depending on the reliability requirements, one can impose a more stringent limit for this criterion instead of the proposed value of $\vartheta_{crit} = 0.1$.

It was also discussed that using a higher order elastic solid solver cannot eliminate the large numerical errors due to the OGSM. In fact, the use of a higher order solver will lead to more pronounced numerical errors caused by the OGSM. It was argued that increasing the accuracy of the solver, can reduce the stability of the solver due to the Godunov theorem.

The Modified Ghost Solid Method (MGSM) and the Double Riemann Ghost Solid Method (DRGSM) were developed. These methods were shown to be reliable alternatives for the OGSM. They were shown to be able to successfully and robustly remove the large numerical errors that would manifest in the form of non-physical oscillations. They are not problem related and they remain stable in all the cases that the implementation of the OGSM would result in instability and large errors in the solution. However, it is worthwhile to mention that the MGSM required solving a Riemann problem at the interface at each time step, while the DRGSM requires solving two Riemann problems at each time step. This adds to the complexity of these methods, as compared to the OGSM.

The special case of acoustic impedance matching of the solids was studied. It was shown, for this special case, all the proposed variants of the GSM remain stable and the results closely agree with the analytical solution. It was found that the ϑ-value remains identically zero which makes the OGSM stable. For the case of acoustic impedance matching of the *fluids*, it was previously observed that the OGFM can lead to non-physical oscillations at the interface. Our studies show that the ϑ-value for the acoustic matching of the fluids reaches a maximum of 1.0 which is ten times larger than the prescribed value. Hence, the OGFM fails. However, for the acoustic impedance matching of the solids, ϑ is identically zero. So, the ϑ-criterion successfully explains the difference of the behavior of the OGSM and OGFM. In other words, this criterion shows that acoustic impedance matching is not necessarily the cause of the numerical errors. However, a combination of factors can lead to large numerical errors. Regardless, of the combination of factors which lead to numerical errors, ϑ-criterion can successfully detect these errors.

Chapter 4

Two Dimensional Elastic-Elastic Solid Interactions

In this chapter[1], by using the techniques developed in Chapter 3, in the normal direction of the interface, one can readily extend to multi-dimensional GSM-based algorithms. One should note, however, that there are additional boundary conditions, more specifically the slip and the no-slip boundary conditions along the interface not applicable for the 1-D problem.

---

[1] Part of this chapter has been presented in the 2D section of the journal paper, "*The ghost solid method for the elastic solid-solid interface*" [101] by Kaboudian and Khoo.

4.1 Governing Equation

The governing equation for an isotropic, linearly elastic solid, in a Cartesian frame of reference, can be formulated as the following, in the conservative form.

$$\frac{\partial U}{\partial t} + \frac{\partial F(U)}{\partial x} + \frac{\partial G(U)}{\partial y} = 0, \tag{4.1}$$

Here,

$$U = \begin{bmatrix} \rho u_x \\ \rho u_y \\ \sigma_{xx} \\ \sigma_{yy} \\ \sigma_{xy} \end{bmatrix} \qquad F(U) = \begin{bmatrix} \sigma_{xx} \\ \sigma_{xy} \\ \rho\alpha^2 u_x \\ (\alpha^2 - 2\beta^2)\rho u_x \\ \rho\beta^2 u_y \end{bmatrix} \qquad G(U) = \begin{bmatrix} \sigma_{xy} \\ \sigma_{yy} \\ (\alpha^2 - 2\beta^2)\rho u_y \\ \rho\alpha^2 u_y \\ \rho\beta^2 u_x \end{bmatrix} \tag{4.2}$$

where, ρ is the density, u_x and u_y are velocity at of each point in x and y direction, respectively; σ_{xx} and σ_{yy} are the normal components of the stress tensor in x and y direction; σ_{xy} is the tangential component of the stress and α and β are the longitudinal and transverse wave speeds, respectively. These are

$$\alpha = \sqrt{\frac{2\mu + \lambda}{\rho}} \qquad \beta = \sqrt{\frac{\mu}{\rho}} \tag{4.3}$$

where μ and λ are the Lamé constants.

Equation (4.1) can be written in the normal-tangential frame of reference, (η-ξ), as

$$\frac{\partial U}{\partial t} + \frac{\partial F(U)}{\partial \eta} + \frac{\partial G(U)}{\partial \xi} = 0. \tag{4.4}$$

Here, the variables η and ξ are used to denote normal and tangential coordinates (see Figure 4.1). Under this framework,

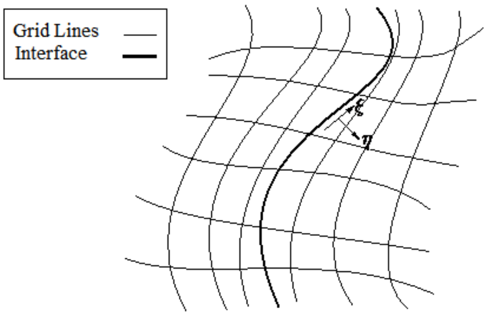

Figure 4.1: η-ξ frame of reference

$$U = \begin{bmatrix} \rho u \\ \rho v \\ \sigma_{\eta\eta} \\ \sigma_{\xi\xi} \\ \sigma_{\xi\eta} \end{bmatrix} \qquad F(U) = \begin{bmatrix} \sigma_{\eta\eta} \\ \sigma_{\xi\eta} \\ \rho\alpha^2 u \\ (\alpha^2 - 2\beta^2)\rho u \\ \rho\beta^2 v \end{bmatrix} \qquad G(U) = \begin{bmatrix} \sigma_{\xi\eta} \\ \sigma_{\xi\xi} \\ (\alpha^2 - 2\beta^2)\rho v \\ \rho\alpha^2 v \\ \rho\beta^2 u \end{bmatrix} \tag{4.5}$$

where u is the velocity in the normal direction (η), v is the velocity in the tangential direction (ξ), and $\sigma_{\eta\eta}$, $\sigma_{\xi\xi}$, and $\sigma_{\xi\eta}$ are the stress components in the normal-tangential coordinate reference frame.

4.2 No-Slip and Perfect-Slip Conditions at the Interface

Different boundary conditions can arise at the interface. We shall only discuss the no-slip and perfect-slip boundary conditions.

4.2.1 No-Slip Condition at the Interface

If the two solids cannot slide at the interface and in the absence of any gap at the interface, then a no-slip boundary condition is appropriate.

The no-gap-formation at the interface implies the continuity of the normal velocity u at the interface

$$u_{I_L} = u_{I_R} = u_I. \tag{4.6}$$

Moreover, it means that the normal component of the traction can be non-zero, and equal for both solids. Consequently, the boundary force balance implies

$$\sigma_{\eta\eta_{I_L}} = \sigma_{\eta\eta_{I_R}} = \sigma_{\eta\eta_I}. \tag{4.7}$$

The no-sliding between the two solids suggests that the relative tangential velocity is zero at the interface. Hence, the tangential velocity v will be continuous across the interface

$$v_{I_L} = v_{I_R} = v_I. \tag{4.8}$$

It also implies that the tangential component of the traction can be non-zero and equal for both solids. Subsequently, boundary force balance leads to

$$\sigma_{\xi\eta_{I_L}} = \sigma_{\xi\eta_{I_R}} = \sigma_{\xi\eta_I}. \tag{4.9}$$

4.2.2 Perfect-Slip Condition at the Interface

For this interfacial boundary condition, no gap is allowed to be formed at the interface. However, the solids can slide against each other.

Similar to the previous section, the requirement of an absence of gap at the interface leads to conditions identical to (4.6) and (4.7) for the normal velocity (u) and the stress component (p). However, allowing the solids to slide, without any friction at the interface, will render conditions (4.8) and (4.9) inapplicable.

4.2.3 Coupled and Uncoupled Variables

Consider a variable χ. The subscripts I_L and I_R are used to indicate if an interfacial value is calculated on the left or right side of the interface, respectively. If due to the boundary conditions at $\mathbf{x}$, there exists a relation κ such that

$$\kappa(\chi_{I_L}, \chi_{I_R}) = 0, \tag{4.10}$$

then χ is considered to be a coupled variable across the interface at that point. Otherwise, it is uncoupled.

4.3 On the 2D OGSM

Here, the extension of the OGSM method given in Section 3.4.2 is presented. Similar to its 1D counterpart, it can be easily applied in practice. Following Fedkiw [2, 88], for the coupled variables one has to copy the values of the real nodes to the ghost nodes in the same region just like for the one-dimensional setting. Variables which are not coupled across the interface, such as material properties, are generally discontinuous and need to be extrapolated across the interface into the ghost nodes.

4.3.1 The OGSM for the No-Slip Condition at the Interface

Conditions (4.6), (4.7), (4.8), and (4.9) must be satisfied at the interface for the values of u, $\sigma_{\eta\eta}$, v, and $\sigma_{\xi\eta}$. Moreover, the Cauchy equation of motion must hold which constraints the admissible values of $\sigma_{\xi\xi}$. As such, the variable U can be considered as a coupled variable. To define the ghost values U_L^* and U_R^*, one has to simply copy the values of U^n at each time step from the closest real node, on the same side of the interface, to the corresponding ghost node.

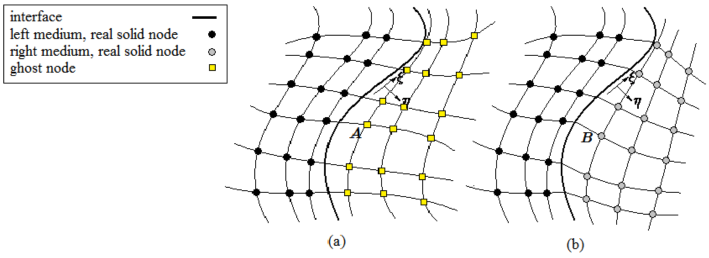

(a) (b)

Figure 4.2: (a) presence of real and ghost solid nodes on the left hand side and the right hand side of the interface, respectively and (b) presence of real solid nodes on both sides of the interface

In Figure 4.2, consider the ghost node A on the right hand side of the interface. In order to define the ghost values at this node, one has to first find the closest real node, B. As soon as this node is found, one can use a simple copy to define the ghost values as

$$U_R^*|_A = U_B. \tag{4.11}$$

To circumvent a lengthy search process, it is possible to define the location of the ghost nodes such that they coincide with real solid nodes. In this way, only a simple copy is necessary for defining the ghost values.

4.3.2 The OGSM for the Perfect-Slip Condition at the Interface

According to section 4.2.2, for this case, only the conditions (4.6) and (4.7) need to be satisfied at the interface. As such, the only coupled variables are u and $\sigma_{\eta\eta}$. Hence, at the time step $t = t^n$ only the values of u^n and $\sigma_{\eta\eta}^n$ need to be copied from the closest real node to the ghost node. The values of v^n, $\sigma_{\xi\xi}^n$, and $\sigma_{\xi\eta}^n$, as well as the material properties need to be extrapolated from the real nodes, across the interface, into the ghost nodes.

4.4 On the 2D MGSM

This is the extension of MGSM in 1-D which was developed in Section 3.4.3. One has to construct and solve an appropriate Riemann problem to determine the values of the coupled variables at the interface to be copied to the ghost nodes. In addition, special attention needs to be paid to $\sigma_{\xi\xi}$, the normal component of the stress tensor, which is in the tangential direction of the interface. Similar to OGSM, the uncoupled variables are extrapolated across the interface into the ghost nodes.

The interfacial points are Lagrangian points and their locations are known at each time step. The locus of the interfacial points forms a curve. If the coordinates of the interfacial points are (X_I, Y_I) and S is the parametrization variable used to parametrize the curve, the unit normal to the interface (N) is given by

$$N = (\frac{\partial Y_I}{\partial S}\mathbf{i} - \frac{\partial X_I}{\partial S}\mathbf{j})/\sqrt{\frac{\partial X_I}{\partial S}^2 + \frac{\partial Y_I}{\partial S}^2} \tag{4.12}$$

where $\mathbf{i}$ and $\mathbf{j}$ are the unit vectors in x-y coordinate system.

Considering node A (see Figure 4.3), which is just bordering the interface, we have the $U_L = U_A$. Next, we search for the nodes B and C on the other side of the interface, which are bordering the right side of the interface, such that they are closest to the normal η exiting node A, and each one is on either side of it. Interpolation between U_B and U_C is required to calculate the value U on the right side of the interface, on the normal η, according to the distance of B and C from η. This interpolated value will be used as U_R. Wang et al [94] have provided a correction algorithm for the values on the real side, specially for critical problems such as shock impedance matching for compressible flow. However, our critical tests in shock impedance matching indicate that such corrections are not quite essential for the elastic solid-solid interactions. Otherwise, one may adopt [94] which has been shown to be reasonably robust.

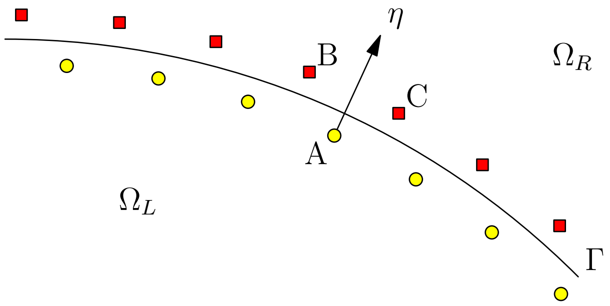

Figure 4.3: Schematics of the real nodes on both sides of the interface to define the Riemann problem

Next, we shall define the following Riemann problem in the perpendicular direction to the interface,

$$\begin{aligned} &\frac{\partial U}{\partial t} + \frac{\partial F(U)}{\partial \eta} = 0 \\ &U(\eta, t = t^n) = \begin{cases} U_L^n & \eta < 0 \\ U_R^n & \eta > 0 \end{cases} \end{aligned} \quad . \tag{4.13}$$

4.4.1 On the No-Slip Condition at the Interface and MGSM

By integrating the characteristics equations of the Riemann problem (4.13), and applying the conditions (4.6) and (4.7), we obtain

$$u_I = \frac{1}{\rho_L \alpha_L + \rho_R \alpha_R} \left(\sigma_{\eta\eta_L} - \sigma_{\eta\eta_R} + \rho_L \alpha_L u_L + \rho_R \alpha_R u_R \right), \tag{4.14}$$

$$\sigma_{\eta\eta_I} = \frac{1}{\rho_L\alpha_L + \rho_R\alpha_R}\left[\rho_L\alpha_L\sigma_{\eta\eta_R} + \rho_R\alpha_R\sigma_{\eta\eta_L} + \rho_L\alpha_L\rho_R\alpha_R\left(u_L - u_R\right)\right], \tag{4.15}$$

$$v_I = \frac{1}{\rho_L\beta_L + \rho_R\beta_R}\left(\sigma_{\xi\eta_L} - \sigma_{\xi\eta_R} + \rho_L\beta_L v_L + \rho_R\beta_R v_R\right), \tag{4.16}$$

and

$$\sigma_{\xi\eta_I} = \frac{1}{\rho_L\beta_L + \rho_R\beta_R}\left[\rho_L\beta_L\sigma_{\xi\eta_R} + \rho_R\beta_R\sigma_{\xi\eta_L} + \rho_L\beta_L\rho_R\alpha_R\left(v_L - v_R\right)\right]. \tag{4.17}$$

Integrating the zero characteristic of the equation (4.13) on the left side results in

$$q_{I_L} = q_L + \frac{\gamma_L}{\alpha_L^2}(p_I - p_L). \tag{4.18}$$

However, if it is integrated on the right hand side, one can get

$$q_{I_R} = q_R + \frac{\gamma_R}{\alpha_R^2}(p_I - p_R). \tag{4.19}$$

Using the obtained values of u_I, v_I, p_I, q_{I_L}, q_{I_R} and τ_I, one can then construct U_{I_L} and U_{I_R} as

$$U_{I_L} = \begin{bmatrix} u_I \\ v_I \\ p_I \\ q_{I_L} \\ \tau_I \end{bmatrix} \quad \text{and} \quad U_{I_R} = \begin{bmatrix} u_I \\ v_I \\ p_I \\ q_{I_R} \\ \tau_I \end{bmatrix}. \tag{4.20}$$

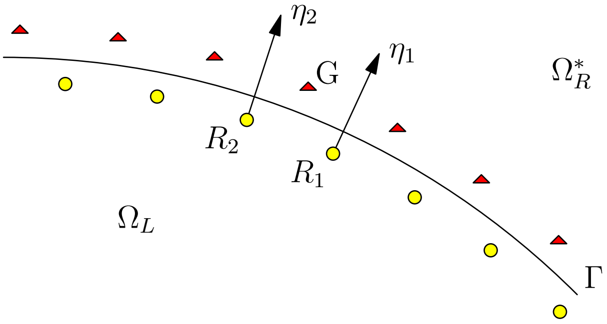

Figure 4.4: The Riemann values on the normals η_1 and η_2 are interpolated to define the values over the ghost node G.

Once values of U_{I_L} are calculated, one can define the ghost nodes by interpolating the values on the normals to the ghost nodes on the right hand side of the interface. For example to define the values on the node G in Fig. 4.4, we interpolate the values of U_{I_L} on η_1 and η_2 to determine U_G, based on its distance from the normals. Material properties of node R_1 and R_2 are extrapolated to the ghost node G. In a similar manner, U_{I_R} values will be copied to the proper ghost nodes on the left side of the interface.

4.4.2 On the Slip Condition at the Interface and MGSM

Here, only the conditions (4.6) and (4.7) must be satisfied for this type of interface condition. Hence, only the values of u and p are coupled.

Similar to Section (4.4.1), u_I and $\sigma_{\eta\eta_I}$ are identical to Eqns. (4.14) and (4.15), respectively. Moreover, the zero characteristic of Eqn. (4.13) are integrated on the left and right side of the interface to obtain results identical to Eqns. (4.18) and (4.19).

The values of u_I and $\sigma_{\eta\eta_I}$ are then copied to the ghost nodes on the right hand side and left hand side of the interface which are closest to the normal line that exits at the point where they are calculated. In a similar manner, $\sigma_{\xi\xi_{I_L}}$ and

$\sigma_{\xi\xi_{I_R}}$ values will be copied to the proper ghost nodes on the right side and the left side of the interface, respectively.

The values of uncoupled variables, v, $\sigma_{\xi\eta}$, and material properties are extrapolated across the interface, accordingly.

4.5 Numerical Experiments

4.5.1 Test Example 1: 2D Experiment-1

In this section, a numerical experiment is devised to compare OGSM and MGSM for a 2D problem. The setup of the experiment is such that it is identical to a 1D problem, in the normal direction of the interface. The results are calculated in the x-y coordinate. However, they are converted to ξ-η directions and then replotted for ease of comparison to the 1-D solution, also to ascertain the viability of the 2-D solution.

The primary interest is in studying the robustness of GSMs for capturing interface interactions. The solution domain is chosen as $\Omega = \{(x,y)|x \in [0,10] \text{ and } y \in [-5,6]\}$, however, the results are only plotted for the region $y \in [0,1]$ to eliminate the effects of top and bottom boundary conditions on the solution. The interface is defined by the line $y = 5.5 - x$. The boundary conditions at the left and right boundaries are

$$u_x(0,y) = u_y(0,y) = u_x(10,y) = u_y(10,y) = 0,$$

and the initial conditions are

$$u(x,y,0) = \sigma_{\eta\eta}(x,y,0) = \begin{cases} 1 & (5.5 - \sqrt{2}/2 - x) \leq y \leq (5.5 - x) \\ 0 & \text{otherwise} \end{cases}$$

$$\forall (x,y) \in \Omega, \quad v(x,y,0) = \sigma_{\xi\xi}(x,y,0) = \sigma_{\xi\eta}(x,y,0) = 0.$$

The material properties of the left medium are $\rho_L = 1$, $\alpha_L = 1$, and $\beta_L = 0.3$; and those of the right medium are $\rho_R = 5$, $\alpha_L = 1$, and $\beta_L = 0.3$.

A second order MUSCL solver together with a grid size of $\Delta x = \Delta y = 0.05$ and CFL number of 0.58 is employed for solving the elastic solid equation in each medium. The solution is obtained at $t_f = 1$. Both the OGSM and MGSM are tested for no-slip and perfect slip conditions at the interface.

The calculated value of ϑ for this test is close to 1 for almost all the time steps which is greater than $\vartheta_{crit} \approx 0.1$. As such, this will lead to non-physical oscillations for the OGSM.

In Figures 4.5 and 4.6, the velocity and stress profiles obtained using OGSM and MGSM for the no-slip condition at the interface, respectively, are shown. It is clear that quantities of computed u, $\sigma_{\eta\eta}$ and $\sigma_{\xi\xi}$ suffer from non-physical oscillations when the OGSM is used which lends support to the proposed ϑ-criterion. It can be seen that the MGSM has successfully removed these mentioned oscillations.

Next, Figures 4.7 and 4.8 show the velocity and stress profiles obtained using OGSM and MGSM for the slip condition at the interface. It can be observed that the computed u, $\sigma_{\eta\eta}$ and $\sigma_{\xi\xi}$ suffer from non-physical oscillations when the OGSM is employed. It is noticed, however, the MGSM does not suffer from any

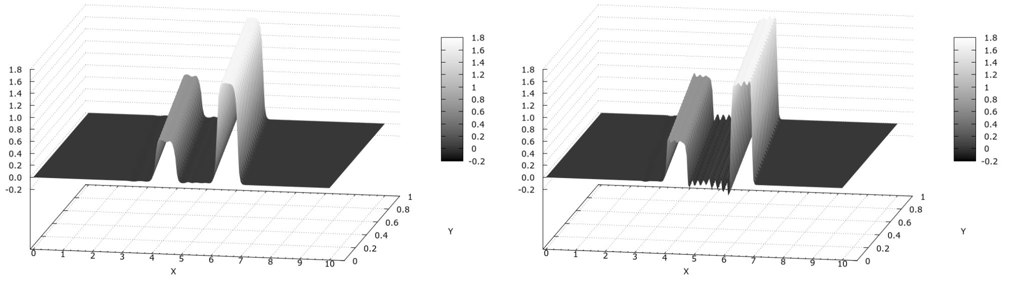

(a) $\sigma_{\eta\eta}$ using MGSM (d) $\sigma_{\eta\eta}$ using OGSM

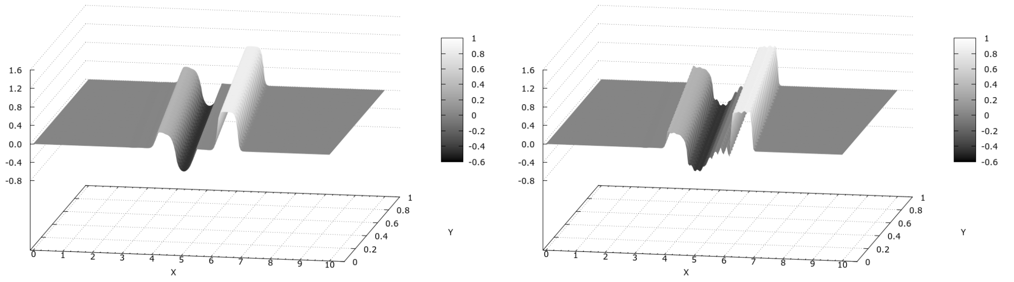

(b) $\sigma_{\xi\xi}$ using MGSM (e) $\sigma_{\xi\xi}$ using OGSM

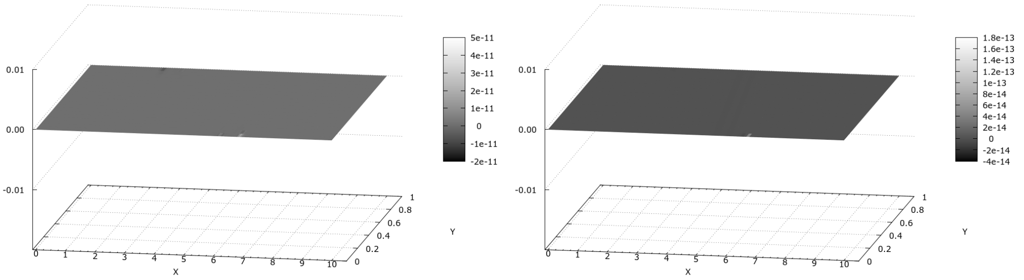

(c) $\sigma_{\xi\eta}$ using MGSM (f) $\sigma_{\xi\eta}$ using OGSM

Figure 4.5: Test Example 1: Comparison of the stress component results obtained using OGSM and MGSM for no-slip condition ($t_f = 1$)

of these oscillations.

It is apparent that both methods, for both the no-slip and the slip interface conditions, can predict the zero value of v and $\sigma_{\xi\eta}$ reasonably well. However, it should be noted that due to the construct of the experiment, all of these values are consistently zero in the entire domain. Hence, minimum error is incurred while still using the OGSM (zero values were copied to the ghost nodes for both MGSM and OGSM). This situation will differ in a general problem.

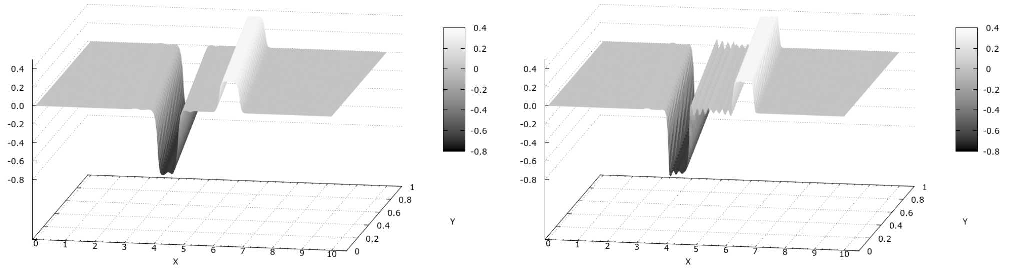

(a) u using MGSM (c) u using OGSM

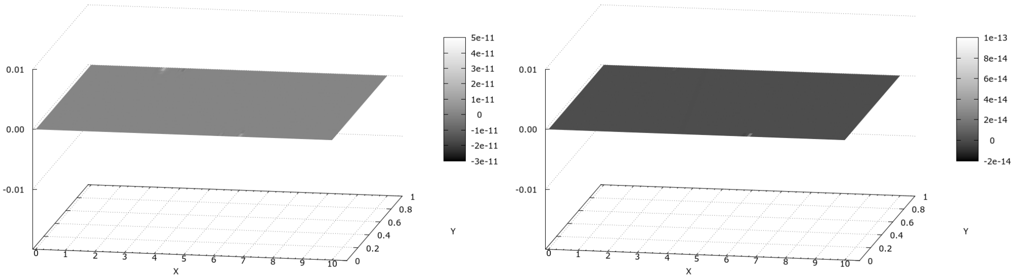

(b) v using MGSM (d) v using OGSM

Figure 4.6: Test Example 1: Comparison of the velocity component results obtained using OGSM and MGSM for no-slip condition ($t_f = 1$)

Finally, Figure 4.9 compares the 2D results against the analytic equivalent 1D solution, along the normal direction to the interface. It can be seen when the MGSM is employed, the numerical results agree with the analytical solution to a much greater extent. However, the numerical results when the OGSM is employed suffer from severe non-physical oscillations close to the interface. These non-physical oscillations are rectified when the MGSM is employed.

4.5.2 Test Example 2: 2D Experiment-2

In this section, a numerical experiment is designed to study the robustness of the GSMs as well as their stability when they are applied to more complex geometry and stress wave interactions.

The solution domain is $\Omega = \{(x, y)|x \in [0, 10] \text{ and } y \in [0, 10]\}$ which com-

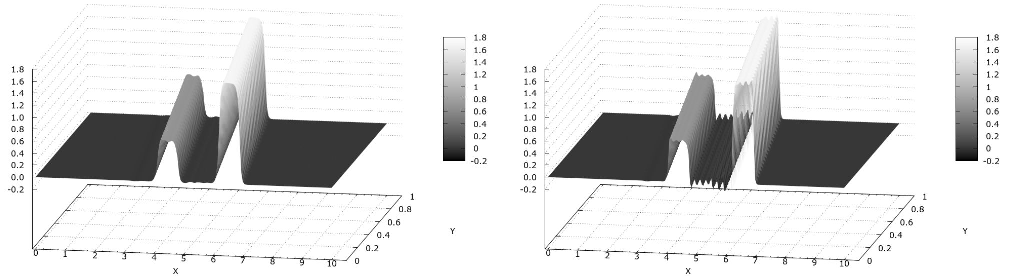

(a) $\sigma_{\eta\eta}$ using MGSM (d) $\sigma_{\eta\eta}$ using OGSM

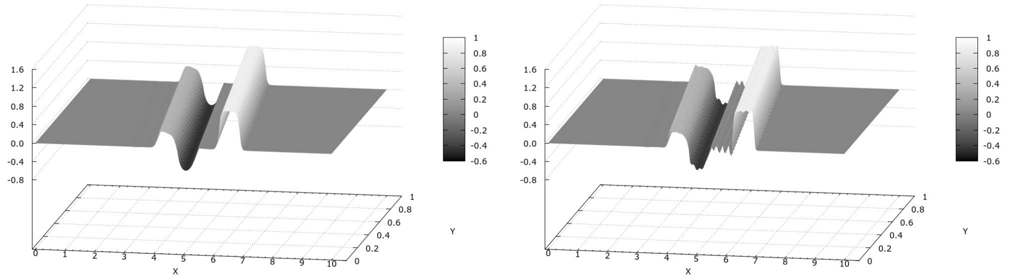

(b) $\sigma_{\xi\xi}$ using MGSM (e) $\sigma_{\xi\xi}$ using OGSM

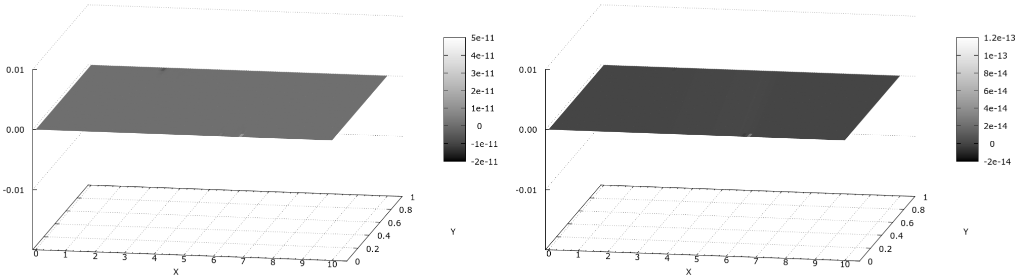

(c) $\sigma_{\xi\eta}$ using MGSM (f) $\sigma_{\xi\eta}$ using OGSM

Figure 4.7: Test Example 1: Comparison of the stress component results obtained using OGSM and MGSM for perfect slip condition ($t_f = 1$)

prises two solids

$$\Omega_1 = \{(x, y) | x < 5 \text{ and } y < (x + 1) \text{ and } y > (9 - x)\}$$

and

$$\Omega_2 = \Omega - \Omega_1.$$

The material properties are $\rho_1 = 5$, $\alpha_1 = 1$, $\beta_1 = 0.3$, $\rho_2 = 1$, $\alpha_2 = 1$, and $\beta_2 =$

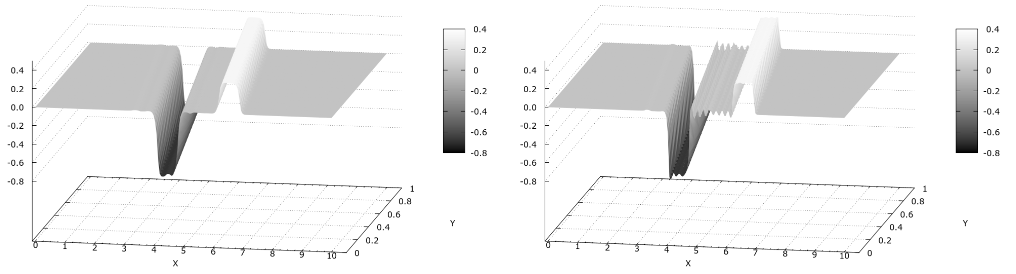

(a) u using MGSM

(c) u using OGSM

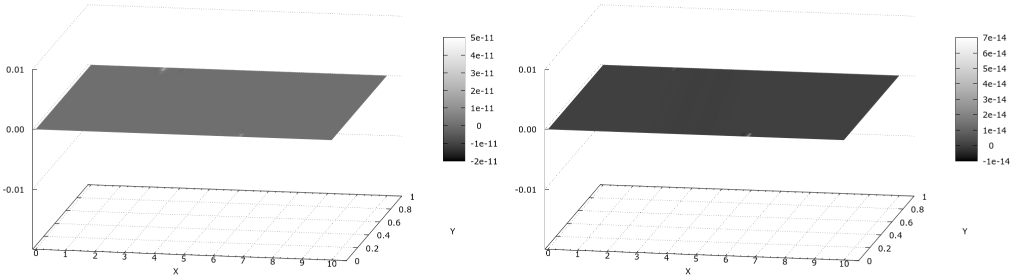

(b) v using MGSM

(d) v using OGSM

Figure 4.8: Test Example 1: Comparison of the velocity component results obtained using OGSM and MGSM for slip condition ($t_f = 1$)

0.3. The initial conditions $u_x = \sigma_{xx} = 1$ when $x \in [3, 4]$ and zero otherwise, and $u_y = \sigma_{yy} = \sigma_{xy} = 0$ everywhere in the domain. Fig. 4.10 shows the schematic of the problem setup. The dark shaded triangle shows Ω_1 and anywhere outside this triangle is Ω_2. The lightly shaded area represents the non-zero region of the initial condition. The arrow in this figure shows the initial direction of the incident wave.

On the left and right boundaries, free surface conditions are imposed, and on the top and bottom boundaries, symmetry conditions are assumed. No slip condition is assumed at the interface of the two solids. A second order MUSCL solver is used together with a grid size of $\Delta x = \Delta y = 0.01$ and a CFL number of 0.65. The solution is obtained for $t = 1.5$.

The calculated value of ϑ for this test is close to 1 for almost all the time

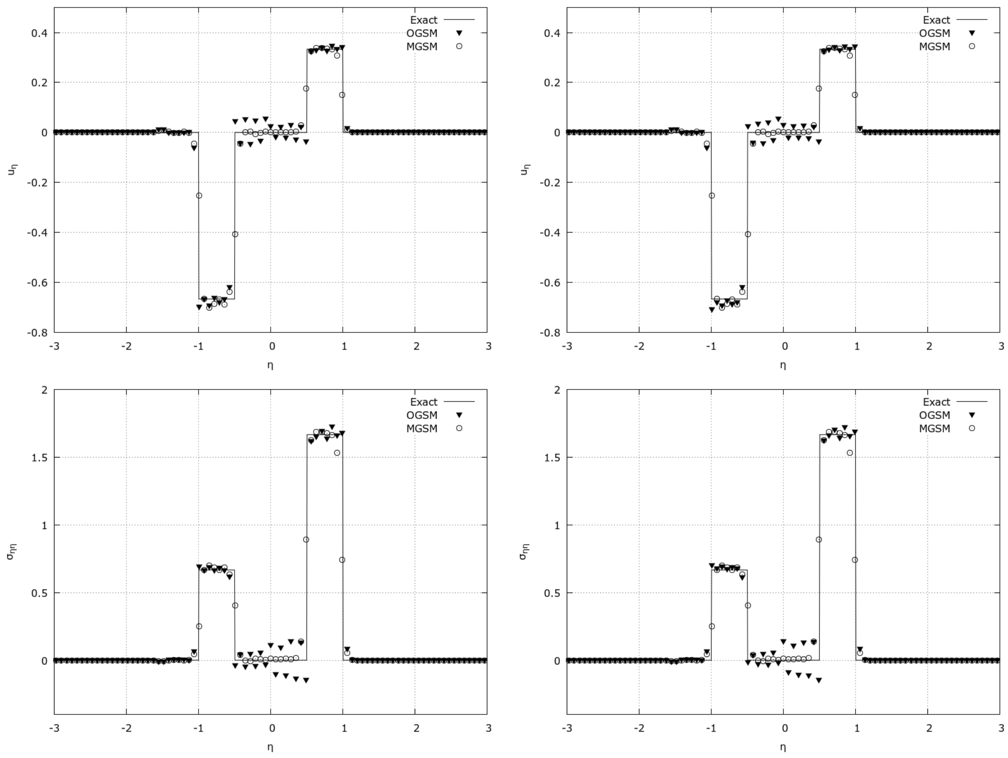

(a) No-Slip Condition

(b) Slip Condition

Figure 4.9: Test Example 1: Normal velocity and normal stress along the line $y = x - 2.5$ with respect to the normal coordinate, η. Results are obtained for $t_f = 1$.

steps which is greater than $\vartheta_{crit} \approx 0.1$. As such, this will lead to non-physical oscillations for the OGSM.

The problem setting provides $y = 5$ as the line of symmetry. Full calculations are carried out with no assumption of symmetry in the methods. Figure 4.11 shows that the MGSM gives a very stable and smooth solution for σ_{xy} while a good symmetry is preserved about $y = 5$. However, it is observed the OGSM is completely unstable. This further attests to the applicability and robustness of the MGSM in comparison to the OGSM when it is applied to more complex geometries and wave interactions.

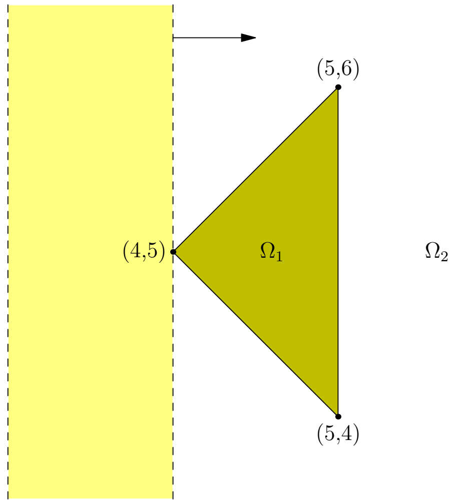

Figure 4.10: Test Example 2: Domain setup and the non-zero region of the initial condition.

4.5.3 Test Example 3: Circular wave interacting with a straight interface

This numerical example is designed to show the applicability of the MGSM in dealing with an expanding wave interacting with a straight interface. Furthermore, we will study the mesh convergence rate for the MGSM.

The material properties for this case are:

$$\rho(x) = \begin{cases} 1 & x < 7 \\ 5 & x > 7 \end{cases}, \qquad \alpha(x) = 1, \qquad \beta(x) = 0.3. \tag{4.21}$$

The initial conditions are

$$u(\mathbf{x}, 0) = v(\mathbf{x}, 0) = \sigma_{xy}(\mathbf{x}, 0) = 0 \quad \sigma_{xx} = \sigma yy = \begin{cases} 1 & (x - 6.5)^2 + y^2 < 1 \\ 0 & \text{otherwise} \end{cases}. \tag{4.22}$$

A schematics of the domain setup and the initial conditions can be seen in

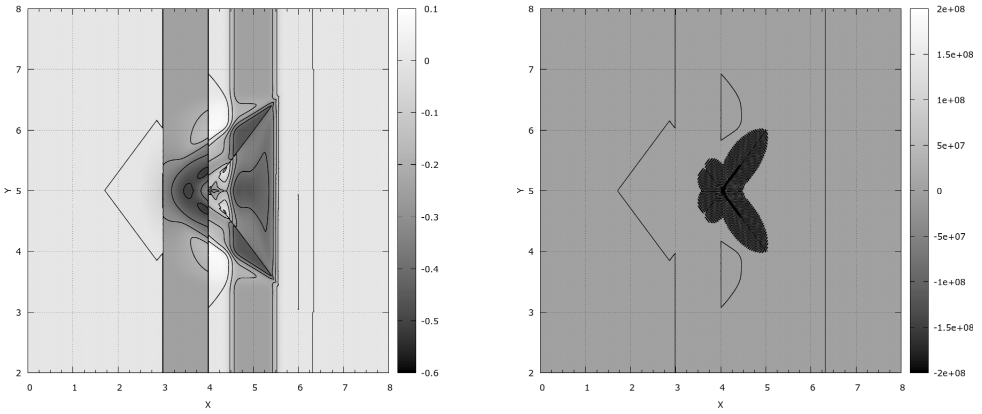

(a) MGSM (b) OGSM

Figure 4.11: Test Example 2: Contour plots of σ_{xy} when the MGSM and the OGSM are employed. Solution is obtained for $t = 1.5$.

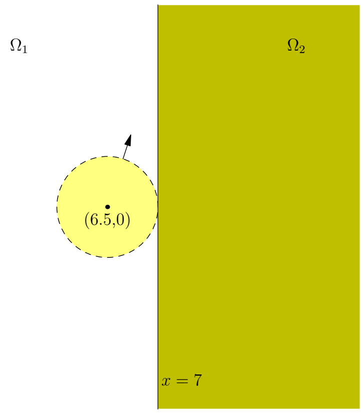

Figure 4.12: Test Example 3: Domain setup and the non-zero section of the initial condition

Fig. 4.12. This setup provides an axis of symmetry along the line $y = 0$. The CFL number is 0.55 and the results are obtained for $t_f = 1.0$. The mesh size in Figs. 4.13 to 4.14 is $\Delta x = \Delta y = 2.5 \times 10^{-2}$.

Fig. 4.13 shows the velocity contours for this problem, obtained using the MGSM method with no-slip conditions applied at the interface. As it can be seen the results have a perfect line of symmetry along the line $y = 0$ and the contours are smooth without any numerical oscillations or wiggles.

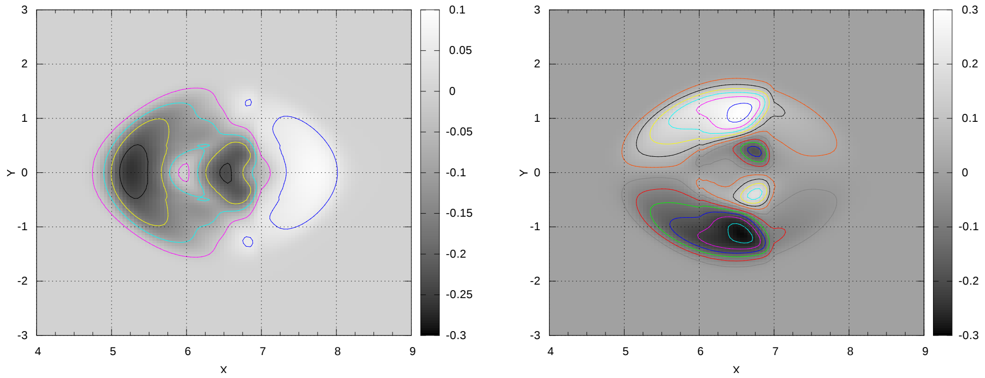

(a) u (b) v

Figure 4.13: Test Example 3: Contour plots of velocity u and v obtained using the MGSM method. The results are obtained for $t_f = 1.0$.

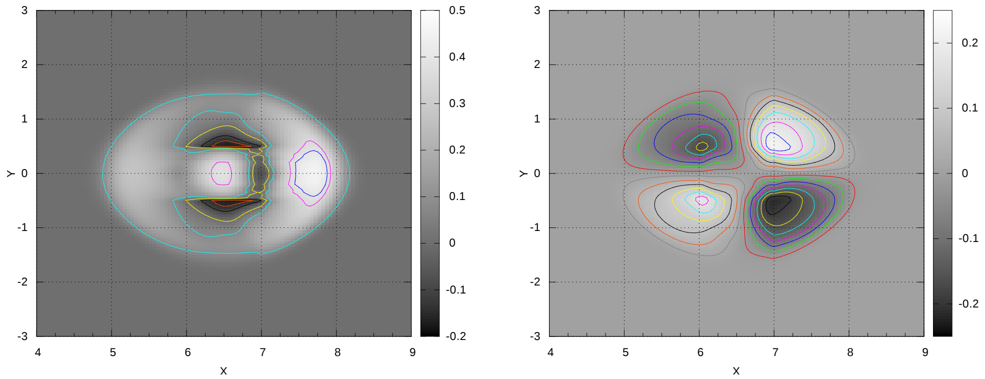

(a) σ_{xx} (b) σ_{xy}

Figure 4.14: Test Example 3: Contour plots of normal and tangential components of stress obtained using the MGSM method. The results are obtained for $t_f = 1.0$.

Fig. 4.14 shows the stress contours for the normal and tangential component of the stress obtained using the MGSM. One may notice that the symmetry along the line $y = 0$ is preserved while the solution remains smooth and free from numerical oscillations.

Fig. 4.15 shows the maximum numerical error for the calculated unknowns over the solution domain vs. various mesh sizes. As it can be seen the maximum error monotonically decreases with mesh refinement. However, the slope of the error line indicates a below first-order accuracy for this problem.

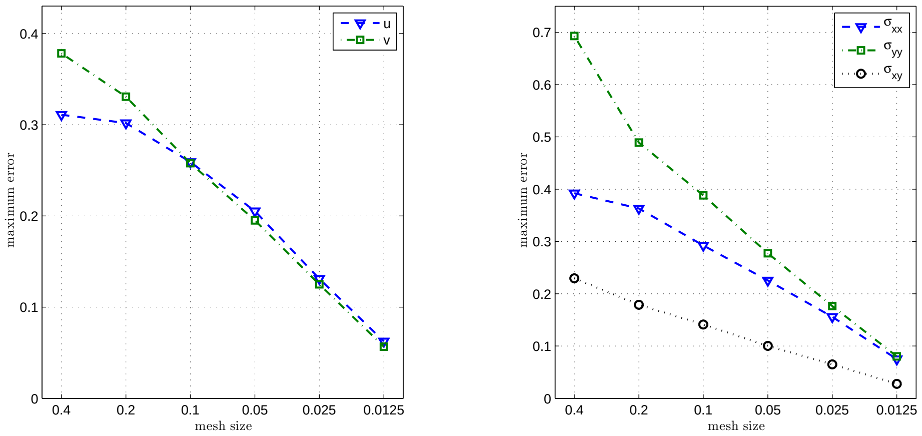

Figure 4.15: Test Example 3: Maximum numerical error for each variable at time $t_f = 1.0$ against various mesh sizes. The results are obtained using the MGSM method.

4.5.4 Test Example 4: Circular wave interacting with a straight interface

This case is very similar to the previous case with a small modification that the wave is expanding and hitting a denser material behind the wave. The density ratio between the material is slightly smaller compared to the previous case. Similar to the previous case, we will study the mesh convergence rate for the MGSM.

The material properties for this case are:

$$\rho(x) = \begin{cases} 3 & x < 6 \\ 1 & x > 6 \end{cases}, \qquad \alpha(x) = 1, \qquad \beta(x) = 0.3. \tag{4.23}$$

The initial conditions are

$$u(\mathbf{x},0) = v(\mathbf{x},0) = \sigma_{xy}(\mathbf{x},0) = 0 \quad \sigma_{xx} = \sigma yy = \begin{cases} 1 & (x-6.5)^2 + y^2 < 1 \\ 0 & \text{otherwise} \end{cases} . \tag{4.24}$$

A schematics of the domain setup and the initial conditions can be seen in Fig. 4.16. This setup provides an axis of symmetry along the line $y = 0$. The CFL number is 0.55 and the results are obtained for $t_f = 1.0$. The mesh size in Figs. 4.17 to 4.18 is $\Delta x = \Delta y = 2.5 \times 10^{-2}$.

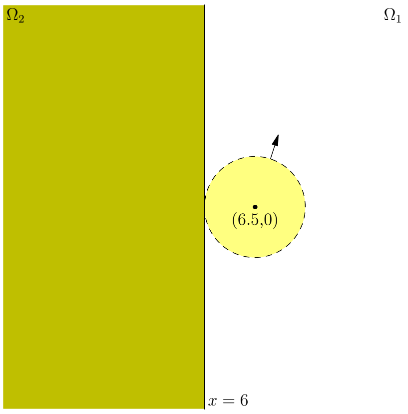

Figure 4.16: Test Example 4: Domain setup and the non-zero section of the initial condition

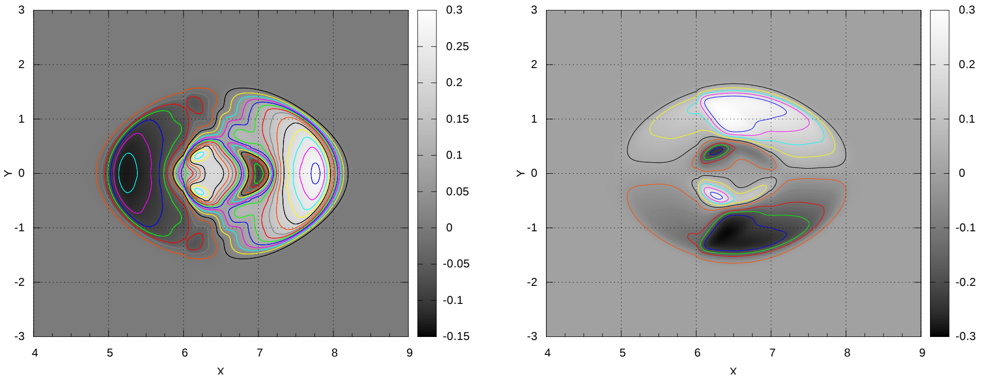

(a) u (b) v

Figure 4.17: Test Example 4: Contour plots of velocity u and v obtained using the MGSM method. The results are obtained for $t_f = 1.0$.

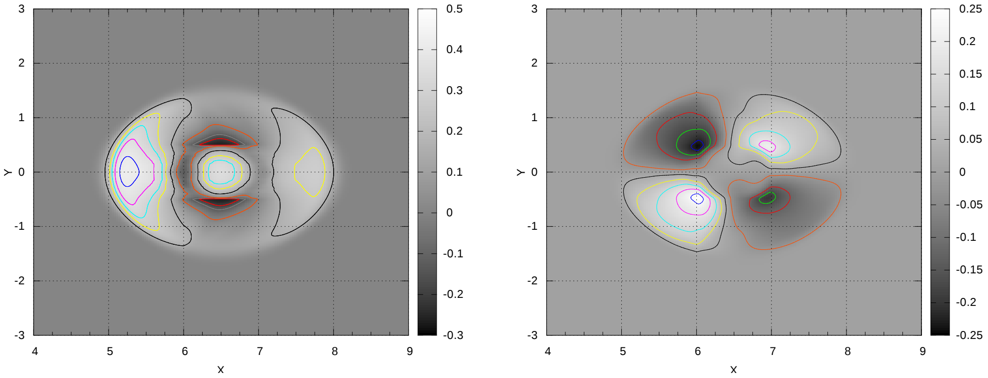

(a) σ_{xx} (b) σ_{xy}

Figure 4.18: Test Example 4: Contour plots of normal and tangential components of stress obtained using the MGSM method. The results are obtained for $t_f = 1.0$.

Figs. 4.17 and 4.18 show the contour plots of velocity and stress components, respectively. The results are obtained using the MGSM together with a FOG solid solver. It can be seen that the results show symmetry along the line $y = 0$. It can be seen the results are free from large numerical oscillations and have produced smooth contours of the solution.

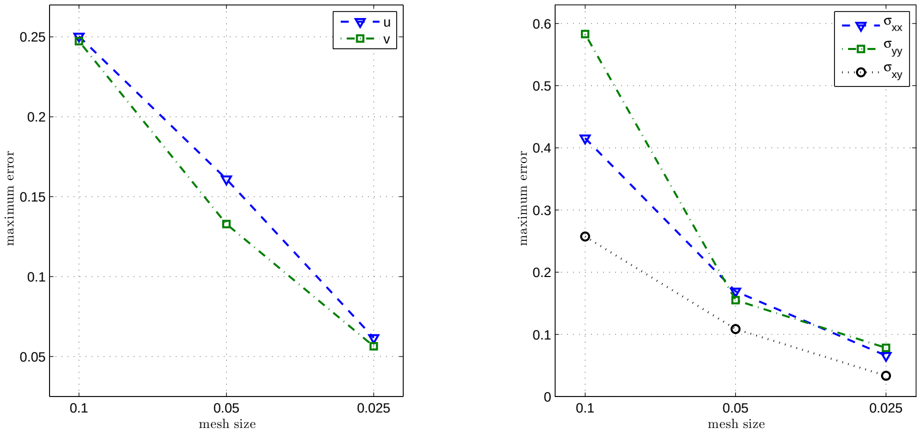

Figure 4.19: Test Example 4: Maximum numerical error for each variable at time $t_f = 1.0$ against various mesh sizes. The results are obtained using the MGSM method.

Fig. 4.19 shows the maximum error incurred in calculating the velocities and stresses, over the solution domain, when the MGSM is applied, against three mesh sizes. The slope of the error line indicates the MGSM results together with the FOG provide a first order method in two dimensional settings.

4.6 Conclusion for Chapter 4

The Original Ghost Solid Method (OGSM) and the Modified Ghost Solid Method (MGSM) for the elastic-elastic interactions at the solid-solid interface were presented in this chapter. The methods were developed for two types of interface conditions, namely the no-slip condition and the perfect slip condition.

It was discussed that the OGSM is simple to implement in the multi-dimensions. However, it can suffer from large numerical oscillations, in multi-dimensions, similar to the 1D settings. Moreover, it was shown that the MGSM can successfully eliminate these large numerical errors; although, implementation of this method can be more complicated compared to the OGSM. It was discussed that both OGSM and MGSM are simpler to implement as compared to the immersed interface method.

Moreover, ϑ-criterion was shown to be able to successfully predict the large numerical errors that can occur due to the use of the OGSM.

The robustness of the MGSM in dealing with more complex geometries, which may include sharp geometrical corners and complex wave interactions, was demonstrated through a numerical experiment. Convergence studies, carried in the numerical experiments presented in this chapter indicate that the MGSM monotonically converges to the analytical solution. Depending on the shape of the interface, and complexity of the waves, the accuracy of the overall numerical solution when combined with a first order solver, can be up-to first order accurate.

Chapter 5

One Dimensional Elastic-Plastic Solid Interactions

In this chapter, the one-dimensional elastic-plastic interaction is investigated. We start with the Original Ghost Solid Method (OGSM), to be followed by the Modified Ghost Solid Method (MGSM). The advantages and possible disadvantages of each of these methods are discussed and compared. Finally, the OGSM and MGSM are validated and compared using numerical experiments.

5.1 Governing Equation

The Cauchy equation of motion at any point inside a solid can be written, in tensor notation, as

$$\rho b_i + \sigma_{ji,j} - \rho a_i = 0 \tag{5.1}$$

where ρ is the density of the material, b is the body force, σ is the stress, and a is the acceleration. Assuming the body forces are negligible, equation (5.1), can be simplified to

$$\sigma_{ji,j} - \rho a_i = 0. \tag{5.2}$$

For the case of pure shear, in a one-dimensional setting, equation (5.2) can be further simplified to

$$\frac{\partial \sigma}{\partial x} - \rho \frac{\partial u}{\partial t} = 0. \tag{5.3}$$

In this work, for the closure of the system, modified Hook's law is employed as the constitutive equation. For 1D elastic-plastic solid, it can be written as

$$d\varepsilon = \frac{1+h}{E} d\sigma \tag{5.4}$$

where ε is the displacement in x-direction, and E is the modulus of elasticity, and $h = h(\kappa)$ is the called the plastic factor:

$$h = \begin{cases} 0, & \text{when} \quad |\sigma + d\sigma| \leq \kappa; \\ E/E_p(\kappa) - 1 & \text{when} \quad |\sigma + d\sigma| > \kappa; \end{cases} \tag{5.5}$$

where κ is the current yield. Substituting equation (5.4) into (5.3) to eliminate ε, we can obtain:

$$\frac{\partial \mathbf{U}}{\partial t} = \mathbf{A}\frac{\partial \mathbf{U}}{\partial x} \tag{5.6}$$

where

$$\mathbf{U} = \begin{bmatrix} u \\ \\ \sigma \end{bmatrix}, \qquad \mathbf{A} = \begin{bmatrix} 0 & 1/\rho \\ \\ E/(1+h) & 0 \end{bmatrix}. \tag{5.7}$$

Equation (5.6) is used as the governing equation for 1D elastic-plastic solid behavior.

5.2 The Elastic-Plastic Riemann Problem

The Riemann problem is given as

$$\frac{\partial \mathbf{U}}{\partial t} = \mathbf{A}\frac{\partial \mathbf{U}}{\partial x}, \qquad \mathbf{U}(x,0) = \begin{cases} \mathbf{U}_L & \text{when} \quad x < x_I \\ \\ \mathbf{U}_R & \text{when} \quad x > x_I \end{cases} \tag{5.8}$$

where x_I is a reference length for the problem. For the solid-solid interaction problem, x_I is considered as the location of the interface. The subscripts L and R refer to the values on the left and right of the interface, and the subscript I refers to the interfacial values.

The objective in solving the Riemann problem is to find the value of $\mathbf{U}_I = \mathbf{U}(x_I, 0)$. We can now solve this problem as illustrated in Figure 5.1.

Assuming that the left and right regions are homogeneous states, the simple wave solution can be found for equation (5.6), for which $\mathbf{U}$ is a function of

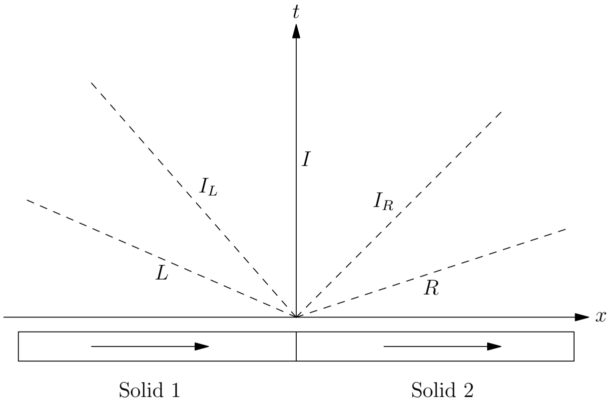

Figure 5.1: Riemann problem in (x, t) plain in the impact of two solid rods.

$c = x/t$ only. Therefore, we can rewrite equation (5.6) as:

$$(\mathbf{I} - c\mathbf{A})d\mathbf{U} = 0, \tag{5.9}$$

where c is a free parameter. However, the following equation must be satisfied so that equation (5.9) can maintain a non-trivial solution, $d\mathbf{U} = 0$:

$$\det(\mathbf{I} - c\mathbf{A}) = 0, \tag{5.10}$$

where “det” is the determinant operator. If we solve equation (5.10) for c we can obtain:

$$c(\kappa) = \pm\sqrt{\frac{E}{\rho[1 + h(\kappa)]}}. \tag{5.11}$$

The positive sign of the solution (5.11) is for the rightward running waves and the negative sign is for the leftward running waves. As such, in the leftward wave region, the information propagates along the characteristic $x/t = c_L(\kappa) = \sqrt{E/(\rho[1 + h(\kappa)])}$ of a rightward running wave. Therefore, in this region the following characteristic equation holds true:

$$du = \frac{d\sigma}{\rho_L c_L(\kappa)}. \tag{5.12}$$

Similarly, in the rightward wave region, the information propagates alongside the characteristic line $x/t = -c_R(\kappa) = -\sqrt{E/(\rho[1+h(\kappa)])}$. Hence, in this region, the following characteristic equation can be considered. That is,

$$du = -\frac{d\sigma}{\rho_R c_R(\kappa)}. \tag{5.13}$$

Now, we can integrate (5.12) from the state L to I_L as:

$$u_{I_L} = u_L + \int_{\sigma_L}^{\sigma_{I_L}} \frac{d\sigma}{\rho_L c_L(\kappa)}; \tag{5.14}$$

and (5.13) from R to I_R as:

$$u_{I_R} = u_R - \int_{\sigma_R}^{\sigma_{I_R}} \frac{d\sigma}{\rho_R c_R(\kappa)}. \tag{5.15}$$

Continuity and balance of force imply

$$u_{I_L} = u_{I_R} = u_I, \quad \sigma_{I_L} = \sigma_{I_R} = \sigma_I. \tag{5.16}$$

Therefore, Eqns. (5.14) and (5.15) can be rewritten as:

$$u_I = u_L + \int_{\sigma_L}^{\sigma_I} \frac{d\sigma}{\rho_L c_L(\kappa)}, \tag{5.17}$$

and

$$u_I = u_R - \int_{\sigma_R}^{\sigma_I} \frac{d\sigma}{\rho_R c_R(\kappa)}. \tag{5.18}$$

Using Eqns. (5.17) and (5.18), we can obtain:

$$\int_{\sigma_L}^{\sigma_I} \frac{d\sigma}{\rho_L c_L(\kappa)} + \int_{\sigma_R}^{\sigma_I} \frac{d\sigma}{\rho_R c_R(\kappa)} = u_R - u_L. \tag{5.19}$$

Equation (5.19) can be solved for σ_I using an iterative method (e.g. the Newton method [108]). Once σ_I is determined, either of the equations (5.17) or (5.18) can be used to calculate u_I.

The solution to the Riemann problem discussed here is used below in conjunction with the proposed numerical methods. A key issue is the assignment of the appropriate values for the leftward and rightward regions in the Riemann problem which will be discussed in more detail in Section 5.3.4.

5.3 GSM Based Algorithms

In this section, we shall discuss the GSM-based algorithms for the elastic-plastic interactions of solids. We will provide the broad outline of these methods.

5.3.1 Outline of various GSMs

Similar to Section 3.4.1, for the GSM-based algorithms, we shall assume that the solution at time $t = t^n$ is known, that is:

$$\begin{aligned}
&\frac{\partial \mathbf{U}}{\partial t} = \mathbf{A}\frac{\partial \mathbf{U}}{\partial x}, \\
&\mathbf{U}(x,t^n) = \begin{cases} \mathbf{U}_L^n(x) & \text{if} \quad x < x_I \\ \mathbf{U}_R^n(x) & \text{if} \quad x > x_I \end{cases}, \quad \mathbf{A}(x,t^n) = \begin{cases} \mathbf{A}_L^n(x) & \text{if} \quad x < x_I \\ \mathbf{A}_R^n(x) & \text{if} \quad x > x_I \end{cases}.
\end{aligned} \tag{5.20}$$

In the implementation, usually a band of 1 to 5 grid points is defined as ghost nodes in the neighborhood of the solid-solid interface. Note that the minimum number of required ghost nodes, which in a particular application may be only one ghost node or even more than 5 ghost nodes, depends on the computational stencil of the single medium solver which is employed. At each point, both ghost solid and real solid are present. We shall assume that the solid-solid interaction is between a left (subscript L) and a right (subscript R) medium. In the GSM-based algorithms for a multi-medium interaction problem, one has to solve for a 1-medium Riemann problem for each of the medium, at each time step. One is for the left solid medium with the following initial conditions

$$\begin{aligned}
&\frac{\partial \mathbf{U}}{\partial t} = \mathbf{A}\frac{\partial \mathbf{U}}{\partial x}, \\
&\mathbf{U}(x,t^n) = \begin{cases} \mathbf{U}_L^n(x) & \text{if} \quad x < x_I \\ \mathbf{U}_R^*(x) & \text{if} \quad x > x_I \end{cases}, \quad \mathbf{A}(x,t^n) = \begin{cases} \mathbf{A}_L^n(x) & \text{if} \quad x < x_I \\ \mathbf{A}_R^*(x) & \text{if} \quad x > x_I \end{cases}.
\end{aligned} \tag{5.21}$$

Here, the $*$ sign is used to represent the ghost solid status at $t = t^n$. Equation (5.21) solves the elastic-plastic problem from the first grid node on the left to the ghost node(s) on the right side of the interface. Similarly, the other Riemann problem for the right solid medium is given as:

$$\begin{aligned} &\frac{\partial \mathbf{U}}{\partial t} = \mathbf{A}\frac{\partial \mathbf{U}}{\partial x}, \\ &\mathbf{U}(x,t^n) = \begin{cases} \mathbf{U}_L^*(x) & \text{if} \quad x < x_I \\ \mathbf{U}_R^n(x) & \text{if} \quad x > x_I \end{cases}, \quad \mathbf{A}(x,t^n) = \begin{cases} \mathbf{A}_L^*(x) & \text{if} \quad x < x_I \\ \mathbf{A}_R^n(x) & \text{if} \quad x > x_I \end{cases}. \end{aligned} \tag{5.22}$$

Equation (5.22) solves for the elastic-plastic problem, from the ghost node on the left of the interface to the last node on the right. It is essential to properly define the ghost values, at the nodes on the left and right side of the interface, for the solution at the real nodes in the equations (5.21) and (5.22) so as to converge to the solution of the multi-medium elastic-plastic problem.

Depending on the method used to define the ghost values on the ghost nodes, two variations of the GSMs are introduced for the elastic-plastic interface.

5.3.2 Coupled and Uncoupled Variables

Consider a variable χ. The subscripts I_L and I_R are used to indicate if an interfacial value is calculated on the left or right side of the interface, respectively. If due to the boundary conditions at $\mathbf{x}$, there exists a relation Γ such that

$$\Gamma(\chi_{I_L}, \chi_{I_R}) = 0, \tag{5.23}$$

then χ is considered to be a coupled variable across the interface at that point. Otherwise, it is uncoupled.

For example, due to continuity at the interface, we have

$$u_{I_L} = u_{I_R}; \tag{5.24}$$

and, due to the balance of force at the interface, we have

$$\sigma_{I_L} = \sigma_{I_R}. \tag{5.25}$$

Therefore, u and σ are considered to be coupled variables. However, modulus of elasticity (E), density (ρ), the plastic factor (h), and the current yield (κ) are not connected through boundary conditions across the interface. Hence, they are considered as uncoupled variables.

5.3.3 On the Original GSM for the elastic-plastic interface

Similar to Section 3.4.2, this method follows the pioneering works by Fedkiw et. al. [2, 88] on the ghost fluid method. Here, the coupled variables, namely the local real solid velocity (u) and stress (σ), are simply copied to the corresponding ghost solid nodes from the real nodes at that location. The uncoupled variables, namely modulus of elasticity (E), density (ρ), the plastic factor (h), and the current yield (κ) are extrapolated from the real solid nodes to the ghost solid nodes, on the other side of the interface. For illustration, see Fig. 5.2. By assuming that the interface lies between the nodes i and $i + 1$, and depending on the single medium solver employed, considering a band of 1 to 5 ghost nodes, on each side of the interface, this method can be formulated as:

$$\begin{aligned} &\mathbf{U}_L^*(x_j) = \mathbf{U}_j^n, \quad \mathbf{A}_j^* = \mathbf{A}_i + 1, \quad i - 4 \leq j \leq i \\ &\mathbf{U}_R^*(x_j) = \mathbf{U}_j^n, \quad \mathbf{A}_j^* = \mathbf{A}_i, \quad i + 1 \leq j \leq i + 5\,. \end{aligned} \tag{5.26}$$

Figure 5.2 schematically illustrates the process of defining the ghost nodes on the right and left hand side of the interface.

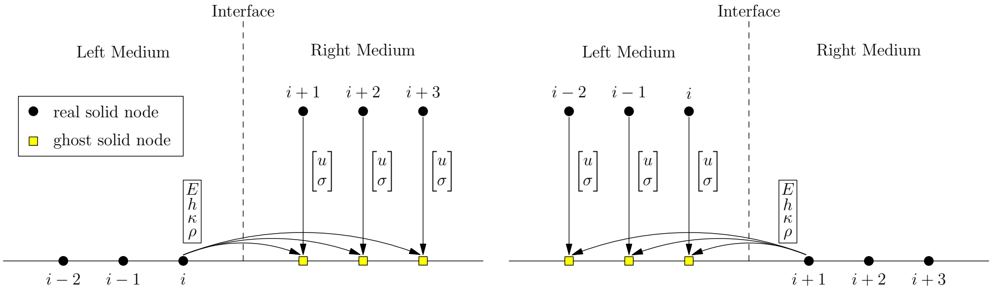

Figure 5.2: Schematics of the original ghost solid method.

As was discussed earlier, in Section 3.4.2, the simplicity of this method lies in that no Riemann problem needs to be solved at the interface to define the value of the ghost nodes. Moreover, no system of equations needs to be solved along with the solid solver in comparison to methods such as the Immersed Interface Method [51]. However, similar to the elastic-elastic interactions, as will be discussed below, under certain conditions it can, and usually will, result in large numerical errors.

5.3.4 On the Modified GSM for the elastic-plastic interface

Here, we take the modulus of elasticity, density, the plastic factor, and the current yield as uncoupled variables and are copied from the real solid nodes to its corresponding ghost solid nodes on the other side of the interface (see Figure 5.3). We shall define the coupled variables, over the ghost nodes ($\mathbf{U}^*$ values), such that the interfacial values predicted by the left and right single mediums (Eqns. (5.21) and (5.22)) will be identical to the interfacial values which are calculated by the multi-medium problem (5.20).

Similar to Section 5.2, we assume u_I and σ_I are interfacial values. Consider the left medium together with the ghost nodes on the right side of the interface. On the left side of the interface, for the rightward running waves, we have:

$$u_I = u_L + \int_{\sigma_L}^{\sigma_I} \frac{d\sigma}{\rho_L c_L(\kappa)}; \tag{5.27}$$

and in the rightward region, for the leftwards running waves we have:

$$u_I = u_R^* - \int_{\sigma_R^*}^{\sigma_I} \frac{d\sigma}{\rho_L c_L(\kappa)}. \tag{5.28}$$

Our objective is to define u_R^* and σ_R^* such that the interfacial values, u_I and σ_I, obtained from Eqns. (5.27) and (5.28) are identical to the solution obtained from Eqns. (5.17) and (5.18). To achieve this objective, we assume that the u_I and σ_I are the solution of the Eqns. (5.17) and (5.18). Then, we shall define u_R^* and σ_R^* such that this solution also satisfies Eqns. (5.27) and (5.28).

It is noted that the Eqns. (5.17) and (5.27) are identical. So, if u_I and σ_I are the solution of the Eqns. (5.17) and (5.18), then, this solution automatically satisfies Eqn. (5.27). It can be seen, if $u_R^* = u_I$ and $\sigma_R^* = \sigma_I$, this solution also satisfies Eqn. (5.27) automatically.

Next and similarly, consider the right medium together with the ghost nodes on the left side of the interface. On the left side of the interface, for the rightward running waves, we have:

$$u_I = u_L^* + \int_{\sigma_L^*}^{\sigma_I} \frac{d\sigma}{\rho_R c_R(\kappa)}; \tag{5.29}$$

and in the rightward region, for the leftwards running waves, we have:

$$u_I = u_R - \int_{\sigma_R}^{\sigma_I} \frac{d\sigma}{\rho_R c_R(\kappa)}. \tag{5.30}$$

We shall aim to define u_L^* and σ_L^* such that the interfacial values, u_I and σ_I, obtained from Eqns. (5.29) and (5.30) are identical to the solution obtained from Eqns. (5.17) and (5.18). To achieve this objective, we assume that the u_I and σ_I are the solution of the Eqns. (5.17) and (5.18). Then, we shall define u_L^* and σ_L^* such that this solution also satisfies Eqns. (5.29) and (5.30).

It is noted that the Eqns. (5.18) and (5.30) are identical. So, if u_I and σ_I are the solution of the Eqns. (5.17) and (5.18), then this solution automatically satisfies Eqn. (5.30). It can be seen that if $u_L^* = u_I$ and $\sigma_L^* = \sigma_I$, this solution also satisfies Eqn. (5.29) automatically.

Now, assuming that the interface lies between the nodes i and $i + 1$, the interfacial values of velocity and stress can be approximated by assuming that

$$\mathbf{U}_L = \mathbf{U}_i^n, \quad \mathbf{U}_R = \mathbf{U}_{i+1}^n, \tag{5.31}$$

and similarly

$$\mathbf{A}_L = \mathbf{A}_i^n, \quad \mathbf{A}_R = \mathbf{A}_{i+1}^n. \tag{5.32}$$

Using the values in (5.31) and (5.32), the solution for the multi-medium Riemann problem, provided in Section 5.2, can be obtained. Subsequently, using the interfacial values $\mathbf{U}_I$, the ghost nodal values can be fully defined as:

$$\begin{array}{lll} \mathbf{U}_L^*(x_j) = \mathbf{U}_I, & \mathbf{A}_L^*(x_j) = \mathbf{A}_{i+1}, & i-4 \le j \le i \\ \mathbf{U}_R^*(x_j) = \mathbf{U}_I, & \mathbf{A}_R^*(x_j) = \mathbf{A}_i, & i+1 \le j \le i+5 \end{array}. \tag{5.33}$$

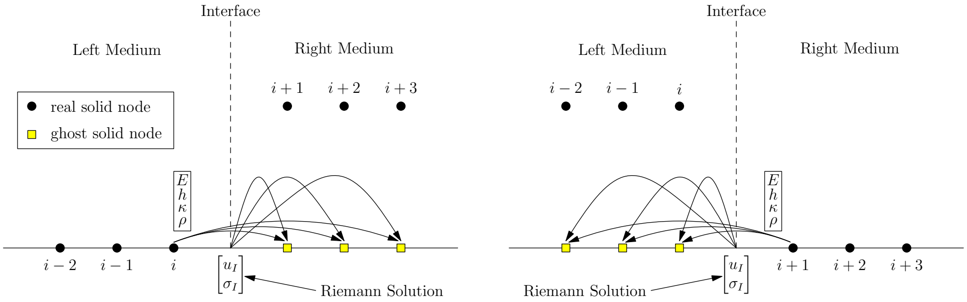

Figure 5.3: Schematic illustration of the MGSM.

Figure 5.3 illustrates this method schematically. Similar to the elastic-elastic interactions, only a single Riemann problem is solved to define the ghost nodes, both on the left and right side of the interface.

By numerical experiment, it will be shown that this method can greatly decrease or eliminate the non-physical oscillations seen for the OGSM. The only disadvantage of the this method vis-a-vis the OGSM is that it involves solving for a Riemann problem at the interface, at each time step.

5.3.5 On the error due to the OGSM and MGSM and their stability

Here, we will follow the analysis which was introduced in Section 3.4.4. It was discussed, if the leading numerical error is traced to the implemented GSMs, the instability of the numerical solution will be associated with, or caused by the use of the GSMs. We shall follow the Lax-Richtmyer stability analysis [104, 105].

We shall assume that the largest due to the use of the GSMs may occur right at the interface. This is due to the fact the effects of using GSMs occur in the cut cells. In Section 5.3.4, we compared the U_I from the MGSM calculation vis-a-vis the multi-medium solution. As such, the error incurred due the use of the MGSM, if the exact solution of the Riemann problem is used, will be theoretically zero. Consequently, the stability of the solution will be unconditionally associated with the stability of the single medium solver employed; i.e. $||E^n||_\infty$ will not be determined via the use of MGSM. Similarly, one can conclude, if an approximate Riemann solver is used for calculating the interfacial values with the MGSM, the stability of the solution will be determined via both the approximate Riemann solver and the single medium solver employed together with the MGSM.

On the other hand, when the OGSM is employed, the interfacial values which are calculated from the left and right mediums are not necessarily identical to those of the exact solution of the multi-medium problem. Here, the maximum error in interfacial velocity with the OGSM is:

$$||E_{u_I}||_\infty = \max\{|u_I - u_{IR}|, |u_I - u_{IL}|\}. \tag{5.34}$$

Similarly, the maximum error due to OGSM, in the stress at the interface is:

$$||E_{\sigma_I}||_\infty = \max\{|\sigma_I - \sigma_{IR}|, |\sigma_I - \sigma_{IL}|\}. \tag{5.35}$$

Here, the index I denotes the interfacial value of the exact solution of the multi-medium problem. The subscript IL and IR refer to the interfacial values obtained from the left and right single medium solutions, respectively.

To obtain u_{IL} and σ_{IL} the equations

$$u_{IL} = u_L + \int_{\sigma_L}^{\sigma_{IL}} \frac{d\sigma}{\rho_L c_L(\kappa)}, \tag{5.36}$$

and

$$u_{IL} = u_R - \int_{\sigma_R}^{\sigma_{IL}} \frac{d\sigma}{\rho_L c_L(\kappa)}. \tag{5.37}$$

must be solved simultaneously. Similarly, to determine u_{IR} and σ_{IR} we need to simultaneously solve

$$u_{IR} = u_L + \int_{\sigma_L}^{\sigma_{IR}} \frac{d\sigma}{\rho_R c_R(\kappa)}, \tag{5.38}$$

and

$$u_{IR} = u_R - \int_{\sigma_R}^{\sigma_{IR}} \frac{d\sigma}{\rho_R c_R(\kappa)}. \tag{5.39}$$

As can be seen, the error incurred in (5.34) and (5.35) has strictly no upper bound. As such, this unbound error can lead to instabilities, if the OGSM is employed. In other words, $||E^n||_\infty$ may be associated with the error incurred by the OGSM. One may observe these large errors either in the form of spurious oscillations, extreme deviation from the analytical solution, or complete instability in the solution. One can be tempted to use higher order single medium solvers to rectify these errors. However, due to the Godunov theorem [102], higher order schemes tend to switch to lower order schemes, specifically a first order one, to avoid the spurious oscillations. Consequently, the use of higher order schemes cannot successfully address the large numerical errors and instabilities due to the use of the OGSM.

It is noted that when

$$||E_{u_I}||_\infty = ||E_{\sigma_I}||_\infty = 0, \tag{5.40}$$

the errors associated with the OGSM are minimized. By comparing (5.40) with (5.34) and (5.35), one can get the conditions

$$u_{IR} = u_{IL} = u_I, \quad \text{and} \quad \sigma_{IR} = \sigma_{IL} = \sigma_I, \tag{5.41}$$

which are the error minimizing conditions. If the conditions in (5.41) are satisfied, the errors in (5.34) and (5.35) will be identically zero. Thus, the stability of the problem becomes synonymous with the stability of the solid solver employed for the single medium. These conditions and their stability characteristics can be used as reference and guide to predict the stability of the (more general)

OGSM. To quantify, a much simpler dimensionless parameter, ϑ, is proposed and applicable for both the velocity and stress:

$$\vartheta = \max\left(\frac{|u_{IL} - u_{IR}|}{|u_{IL}| + |u_{IR}|}, \frac{|p_{IL} - p_{IR}|}{|p_{IL}| + |p_{IR}|}\right). \tag{5.42}$$

The ϑ value quantifies how close the numerical solution is to the conditions in (5.41). The range of ϑ is $[0, 1]$. Our extensive numerical tests indicate that the maximum permissible value of ϑ, before clearly perceptible non-physical oscillations are observed, is $\vartheta_{crit} \approx 0.1$. The above discussion not only explains the origin/reason for possible large numerical errors, but also provides a means forward to determine when the OGSM results are reliable. For the latter, one can establish beforehand if ϑ is within the permissible range to ensure the numerical errors are kept to an acceptable level as time progresses. If at any time step, ϑ exceeds the maximum permissible value, the OGSM can no longer be considered as a suitable approach. One may use an alternative GSM at that particular time step. Subsequently, if the value of ϑ drops below 0.1, the OGSM can be reinstated for use due to its simplicity.

It is worthwhile to mention that a more stringent limit for ϑ_{crit} can be used depending the accuracy desired. Moreover, the calculation of ϑ is not computationally expensive, as the first order fluxes may be readily available to calculate ϑ, specially if a TVD solver is used.

5.4 Numerical Experiments

In this section, various numerical experiments are presented to study various aspects of the original and modified GSMs. In our experiments, it is assumed that the materials obey either a linearly elastic, linearly plastic, work hardening stress-strain relationship given by

$$E = \begin{cases} E_0 & \text{when} \quad \sigma < \kappa \\ E_p & \text{when} \quad \sigma \geq \kappa \end{cases}, \tag{5.43}$$

where E_0 is the elastic modulus, E_p is the plastic modulus during plastic loading, σ is the current stress, and κ is the current yield stress; or, the solid materials obey the linearly elastic, power-law work-hardening plastic stress strain relationship given by

$$\frac{1}{E_p(\kappa)} = \frac{\alpha}{E}\left(\frac{\kappa}{\kappa_0}\right)^{\alpha-1} \tag{5.44}$$

where κ is the current yield stress and κ_0 is the initial yield stress of the material; and α is a material parameter.

5.4.1 Test Example 1: On the possible large numerical errors due to the use of the OGSM

It was earlier seen when OGSM is employed to apply the interface conditions, at the elastic-elastic interface, large errors can occur as non-physical oscillations. Elastic-plastic deformations can transform energy into plastic deformation. If OGSM is employed to model the elastic-plastic solid-solid interface, under certain situations it can lead to large errors. However, due to the dissipative nature of the elastic-plastic phenomenon, the errors may or may not manifest in the form of uncontrolled large non-physical oscillations. This example is designed to show that when using the OGSM with elastic-plastic model, the large numerical errors can be in the form large deviations from the solution and not numerical oscillations.

The domain of the solution is $[-5, 5]$ and the interface is located at $x_I = 0$. The initial velocity is $u(x, 0) = 1$ when $x \in [-5, 0]$ and is zero otherwise. The initial normal stress $\sigma(x, 0) = 0$ everywhere in the domain. The boundary conditions are $u(-5, t) = 1$ and $u(5, t) = 0$. The grid size is $\Delta x = 0.01$ and CFL=0.95.

We assume the solid materials obey the linearly elastic, power-law work hardening relation, given by Eqn. (5.44).

Four sets of material properties are assumed:

1. Set #1.1: $\rho_L = E_L = 1$, on the left side of the interface, and $\rho_R = E_R = 1.4$ on the right side; the elastic limit for the left and right medium is considered to be $\kappa_L = \kappa_R = 10$.

2. Set #1.2: $\rho_L = E_L = 1$, on the left side of the interface, and $\rho_R = E_R = 1.4$ on the right side; the elastic limit for the left and right medium is considered $\kappa_L = \kappa_R = 0.5$.

3. Set #1.3: $\rho_L = E_L = 1$, on the left side of the interface, and $\rho_R = E_R = 5$ on the right side; the elastic limit for the left and right medium is considered to be $\kappa_L = \kappa_R = 10$.

4. Set #1.4: $\rho_L = E_L = 1$, on the left side of the interface, and $\rho_R = E_R = 1.4$ on the right side; the elastic limit for the left and right medium is considered $\kappa_L = \kappa_R = 0.75$.

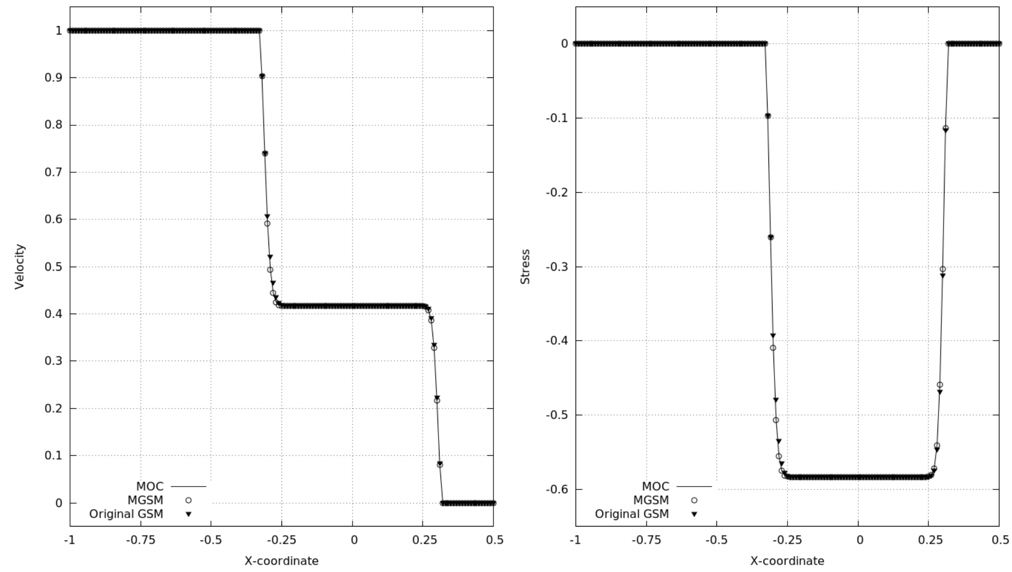

Figure 5.4: Test Example Set #1.1: velocity and stress profile. Solution is obtained for $t_f = 0.3$.

Figure 5.4 shows the velocity and stress profile at $t_f = 0.3$ for the first material set (Set #1.1). Under this setting, there will only be elastic-elastic interactions as the stress does not reach the yield stress. The maximum observed ϑ value is $\vartheta_{max} = .02$, at the 4th time step which is well below the prescribed/suggested critical value of $\vartheta_{crit} = 0.1$. No significant numerical error is observed in the stress profile when either OGSM or MGSM is applied, when the results are compared against the Method-of-Characteristics[1] (MOC) which is a semi-analytical solution.

---

[1] For more information on the Method-of-Characteristics (MOC), one can consult the article by Sarra A. Scott [109], the books by Courant et al [110] and by F. John [111], the tech report by Evans [112], the handbooks by Polianin [113, 114], or the classroom notes by M. Delgado [115]. As such, the detailed calculation is not repeated here.

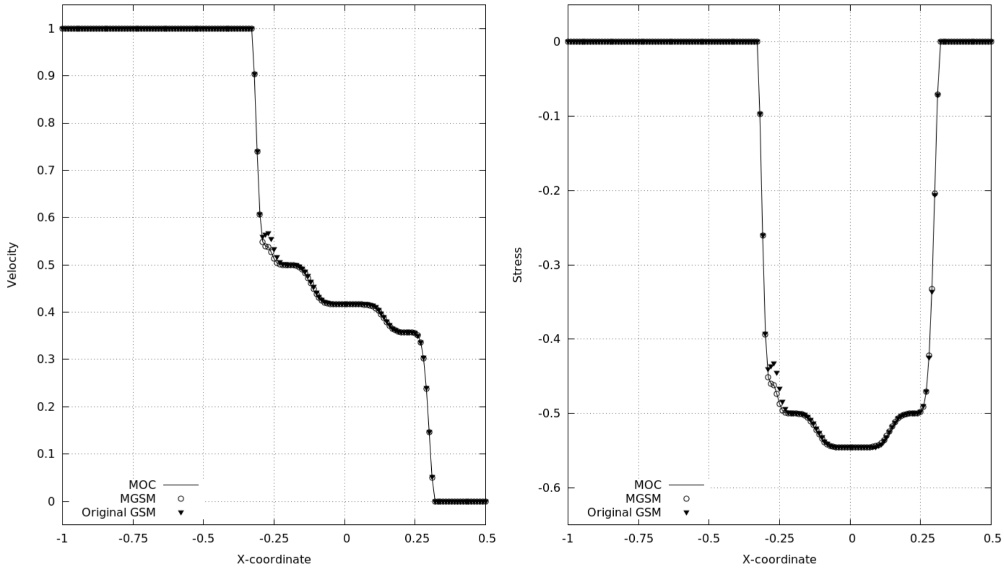

Figure 5.5: Test Example Set #1.2: velocity and stress profile. Solution is obtained for $t_f = 0.3$.

Figure 5.5 shows the velocity and stress profile for the second set of materials (Set #1.2), and the solution is obtained for $t_f = 0.3$. In this setting, plastic deformation is observed as the stress exceeds the yield stress in both the left and right mediums. It is found that $\vartheta_{max} = .07$ occurs at the third time step and is still 30% below the prescribed critical value of $\vartheta_{crit} = 0.1$. No critical instability is observed. However, it can be seen that MGSM still performs better in predicting the reflected plastic wave from the interface for both the stress and velocity profile when compared against the profiles obtained by the Method-of-Characteristics (MOC).

Figure 5.6 shows the velocity and stress profile for the third set of materials (Set #1.3), and the solution is obtained for $t_f = 0.2$. The maximum observed ϑ-value is $\vartheta_{max} = 1$ at the 3rd and 4th time steps which is ten times larger than the maximum permissible value of $\vartheta_{crit} = 0.1$. All the stress values remain below the yield stress of the materials in the left and right medium, and hence,

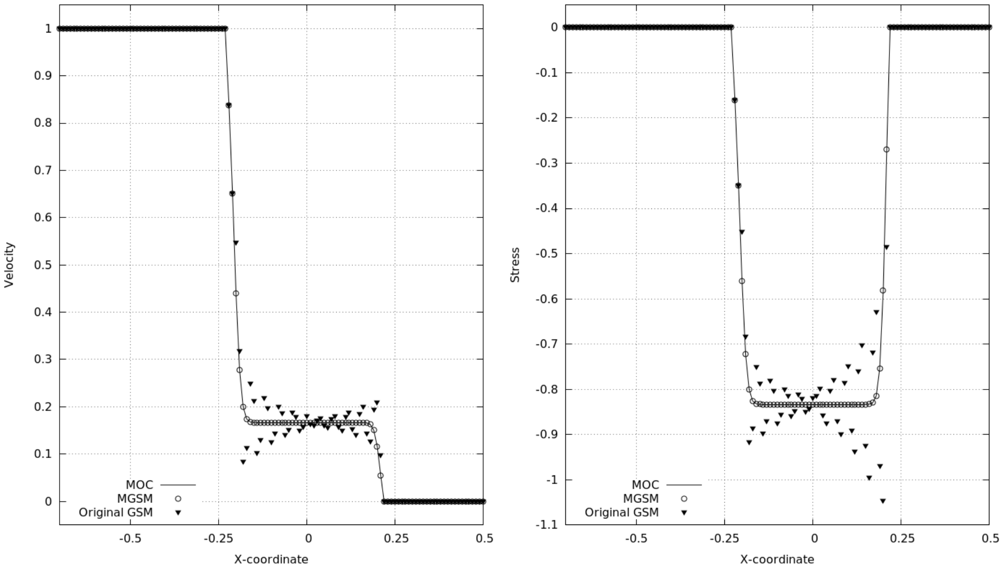

Figure 5.6: Test Example Set #1.3: velocity and stress profile. Solution is obtained for $t_f = 0.2$.

the deformation is elastic in both mediums. It can be seen that the OGSM has led to large deviation in the velocity and stress profile from the semi-analytical solution while the MGSM has remained stable and accurate.

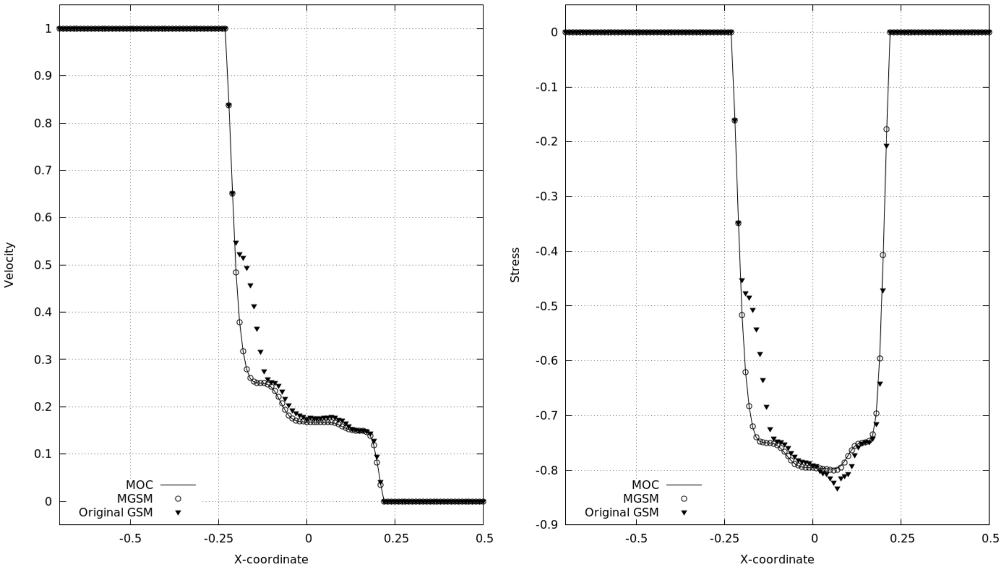

Figure 5.7: Test Example Set #1.4: velocity and stress profile. Solution is obtained for $t_f = 0.2$.

Figure 5.7 shows the velocity and stress profile for the fourth set of materials

(Set #1.4), and the solution is obtained for $t_f = 0.2$. The maximum observed ϑ-value is $\vartheta_{max} = 0.36$ at the 3rd time step which is well above the maximum permissible value of $\vartheta_{crit} = 0.1$. The stress at the interface is above the yield stress in both the left and right mediums, and hence causes a plastic wave to propagate in both mediums. It can be seen that the OGSM has caused large errors in both the velocity and stress profiles while MGSM remains stable and provides results which agree well with the Method-of-Characteristics (MOC). Although, it seems that the errors in OGSM predictions for the elastic-plastic case are not as large as the elastic-elastic interaction case, when the ϑ values are well above the prescribed maximum permissible value ϑ_{crit}, the numerical predictions of the OGSM have shown clear deviations from the semi-analytical results. Whether the numerical errors are in the form of the form of physical oscillations or deviations from the physical solution, the ϑ-criterion can successfully predict these errors.

5.4.2 Test Example 2: On the possible numerical oscillations due to OGSM

When OGSM is employed for the elastic-plastic interface, it can cause large errors in the form of numerical oscillations. This test is designed to show an elastic wave impacting on the interface and hence causing elastic-plastic deformation in both mediums. Propagation of elastic-plastic waves is studied in both mediums in this experiment. In this example, the large numerical errors due to the OGSM occur in the form of oscillations (observed as time progresses) and general instabilities in the solution.

Domain of the solution is $[-4, 4]$ and the interface is located at $x_I = 0$. The initial condition are $u(x, 0) = \sigma(x, 0) = 0$, everywhere in the domain. The boundary conditions are $\sigma(-4, t) = -u(-4, t) = 3$ and $\sigma(4, t) = u(4, t) = 0$. The mesh size is assumed to be $\Delta x = 0.05$ and the CFL=0.99.

We shall assume the solid materials obey the linearly elastic, power-law work hardening relation, given by Eqn. (5.44). We consider two material sets:

1. Set #2.1: $\rho_L = E_L = 1$, on the left side of the interface, and $\rho_R = 12$ and $E_R = 8$ on the right side; the elastic limit for the left and right medium is considered to be $\kappa_L = \kappa_R = 10$.
2. Set #2.2: $\rho_L = E_L = 1$, on the left side of the interface, and $\rho_R = 12$ and $E_R = 8$ on the right side; the elastic limit for the left and right medium is considered to be $\kappa_L = \kappa_R = 3$; $\alpha_L = \alpha_R = 3$.

In this way, the material Set #2.1 will only undergo elastic-elastic interactions, as a control set, while the second material Set #2.2 experiences elastic-plastic interactions.

Figure 5.8 shows the velocity and stress profile for the Set #2.1 at the time of $t_f = 5.5$. The predicted stresses are well below the yield stress. Hence, the interaction at the interface is completely elastic. The maximum ϑ value is 1.0 at $t = 4.06$. After the incident wave impacts on the interface the ϑ value remains above the critical value of 0.1 and oscillates between 0.26 and 1. As it can be seen the results obtained using the OGSM are unstable, with very large numerical errors in the form of large amplitude oscillations observed in the stress

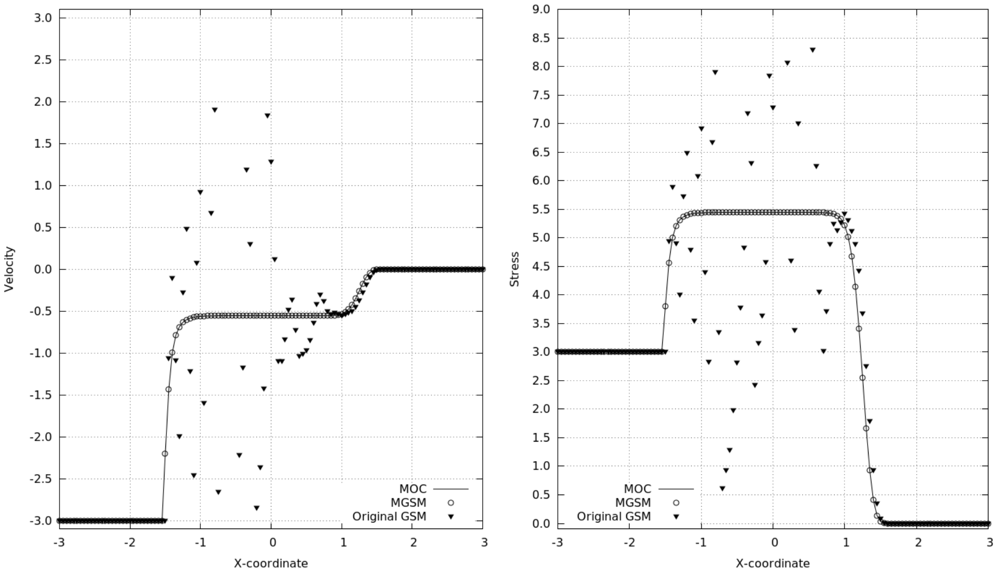

Figure 5.8: Test Example Set #2.1: velocity and stress profile. Solution is obtained for $t_f = 5.5$.

an velocity at the interface as time progresses, while the MGSM remains stable and concurs well with the MOC. In this case, the use of the OGSM has rendered the results completely unreliable.

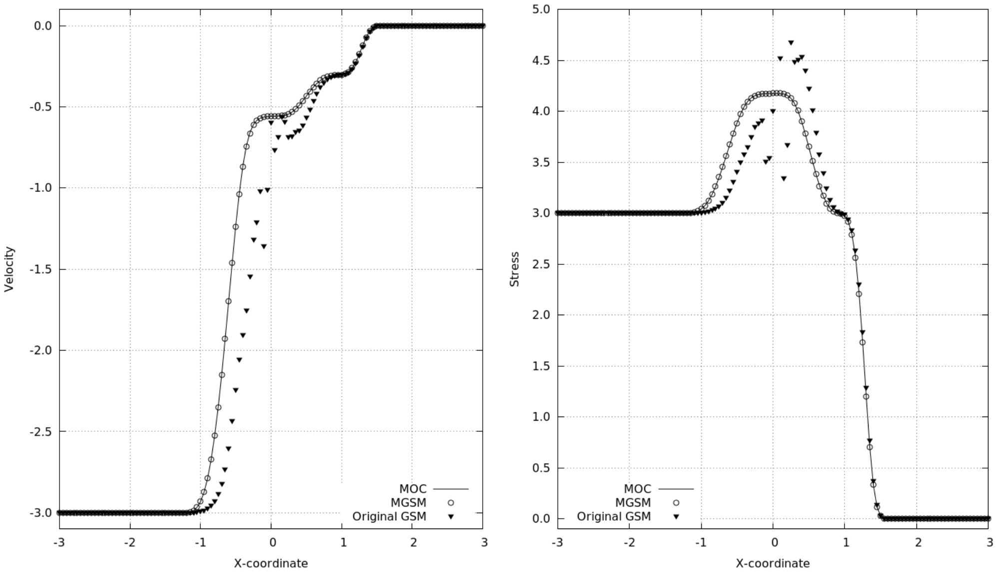

Figure 5.9: Test Example Set #2.2: velocity and stress profile. Solution is obtained for $t_f = 5.5$.

Figure 5.9 shows the velocity and stress profile for the Set #2.2 at the time of $t_f = 5.5$. In this scenario, the stress values at the interface exceed the elastic limit and a plastic wave is formed at the interface which propagates to the left and right medium. The ϑ value exceeds the prescribed maximum permissible value of 0.1 by reaching 0.57 at $t = 4.06$, and continues to grow until it reaches a maximum of 1.0 at $t = 4.8$. As it can be seen the results obtained using the OGSM suffer from large numerical errors in both the stress and velocity profiles, which is consistent with the predictions of the ϑ-criterion. In particular, the numerical errors in the stress profile manifest as oscillations too. These large errors make the OGSM results practically unreliable. It is also noticed that the MGSM remains stable and the results obtained agree very well with the method of characteristics (MOC). As it was earlier discussed in Section 5.3.5, in this case the stability of the MGSM is synonymous as the stability of the elastic-plastic solver employed in the problem.

5.4.3 Test Example 3: Loading history discontinuity and the performance of GSMs

There can be occasions whereby a discontinuity in a problem is only due to different loading histories, e.g. parts of the solid can undergo work hardening.

In this experiment, the solids are assumed to obey the linearly elastic, power-law work hardening relation, given by Eqn. (5.44). The material properties are:

$$\text{Left Solid:}\begin{cases}\rho = 1.0\\ E = 1.0\\ \alpha = 3\\ \kappa_0 = 1.0\end{cases}\qquad \text{Right Solid:}\begin{cases}\rho = 1.0\\ E = 1.0\\ \alpha = 3\\ \kappa_0 = 0.9\end{cases}.$$

The initial conditions are:

$$u(x,0) = -\sigma(x,0) = \begin{cases}1.0, & x \in [-1.5, 0.5]\\ 0, & \text{otherwise}\end{cases}.$$

The interface is at $x_I = 0$ and the solids on the left and right side of it extend indefinitely in the left and right directions, respectively. The grid size is taken to be $\Delta x = 0.005$ and the CFL number is 0.96. The solution is obtained for $t_f = 2.0$.

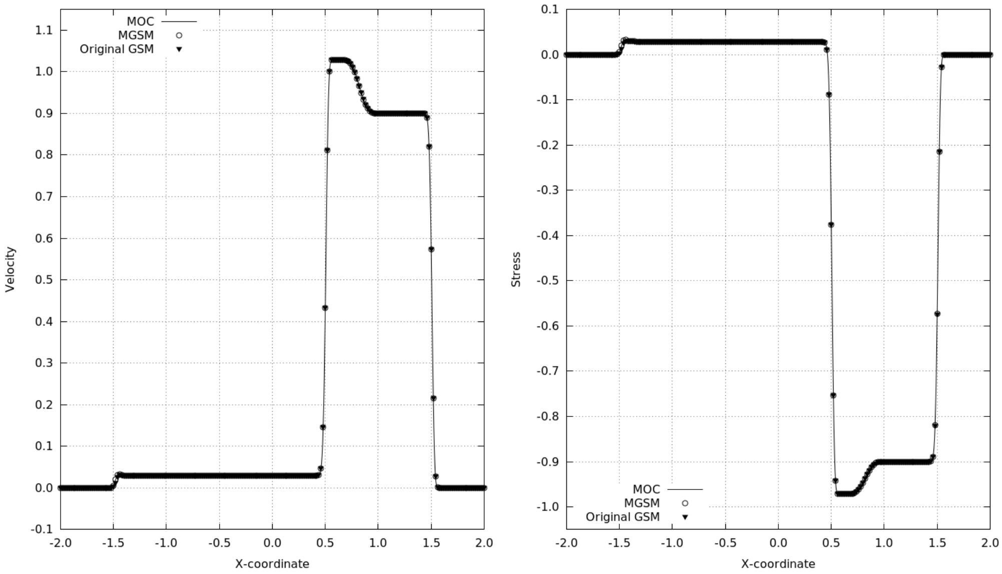

Figure 5.10: Test Example #3: velocity and stress profile. Solution is obtained for $t_f = 2.0$. For clarity, every second grid point is used for plotting.

In this numerical experiment, the rightward moving wave will cause elastic-plastic deformations in the right medium as the stress level is above the yield stress. It is observed that ϑ value reaches a maximum value of 0.01 which is well below the prescribed maximum permissible value of $\vartheta_{crit} = 0.1$. Figure 5.10 shows the velocity and stress profile in the domain at the time $t_f = 2.0$. As it can be seen, the GSMs can successfully apply the interface conditions without causing any additional numerical errors which confirms the predictions by the ϑ-stability criterion. The results obtained by both GSMs agree with the (semi-analytical) results obtained using the MOC.

5.4.4 Test Example 4: Under the special case of acoustic impedance matching conditions in the elastic-plastic region

In Section 3.5.4, the special case of acoustic impedance matching conditions was presented for the elastic-elastic interactions. In this section, the material properties are carefully chosen to achieve acoustic impedance matching conditions when one of the media undergoes plastic loading.

In this experiment, it is assumed that the materials obey a linearly elastic, linearly plastic, work hardening stress-strain relationship given by Eqn. (5.43). Two sets of problems are considered:

1. Set #4.1: The solution is obtained for $t_f = 0.35$ and the material proper-

ties are:

$$\text{Left Solid:}\begin{cases}\rho = 2.0\\ E_0 = 0.5\\ E_p = 0.4\\ \kappa = 2.0\end{cases}\qquad \text{Right Solid:}\begin{cases}\rho = 1.0\\ E_0 = 1.1\\ E_p = 1.0\\ \kappa = 0.1\end{cases}.$$

2. Set #4.2: the solution is obtained for $t_f = 0.2$ and the material properties are:

$$\text{Left Solid:}\begin{cases}\rho = 1.0\\ E_0 = 1.0\\ E_p = 0.8\\ \kappa = 2\end{cases}\qquad \text{Right Solid:}\begin{cases}\rho = 2.0\\ E_0 = 0.55\\ E_p = 0.5\\ \kappa = 0.1\end{cases}.$$

The initial conditions for both cases are:

$$u(x,0) = -\sigma(x,0) = \begin{cases}1 - 0.5x, & x \in [-0.2, 0]\\ 0, & \text{otherwise}\end{cases}. \tag{5.45}$$

The interface is located at $x_I = 0$ while the left and right solids extend indefinitely to the left and right, respectively. The grid size is $\Delta x = 0.001$, and the CFL number is assumed to be 0.99.

The wave is rightward moving. As it enters the right medium, Set #4.1 and #4.2 are designed such that the right solid undergoes plastic loading at the interface until the wave passes through. In the left medium, the stress levels

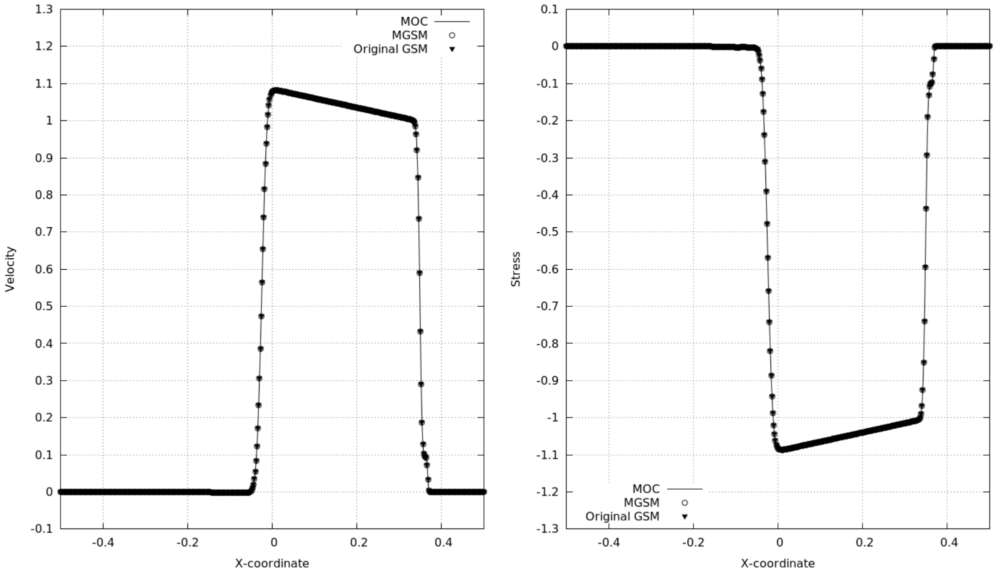

Figure 5.11: Test Example S #4.1: velocity and stress profile. Solution is obtained for $t_f = 0.35$. For clarity, every second grid point is used for plotting.

are well below the yield and the solid undergoes elastic unloading. The elastic acoustic impedance in the left medium matches the plastic acoustic impedance in the right medium. Hence, acoustic impedance matching conditions are achieved in this interaction.

Figure 5.11 shows the velocity and stress profile for Set #4.1. It can be seen the wave passes through without any reflection at the interface. The maximum observed ϑ in this setting is 0.0025 which is well below the maximum permissible limit of 0.1. It is observed that the OGSM remains stable in this setting.

Figure 5.12 shows the velocity and stress profile for set #4.2. It is observed the wave passes through without any reflection at the interface. The maximum observed ϑ in this setting is 0.0012 which is well below the maximum permissible limit of 0.1. It is observed that the OGSM remains stable under this setting.

From the above, it is clear that both GSMs are successful in predicting the acoustic impedance matching case and their results agree with the results

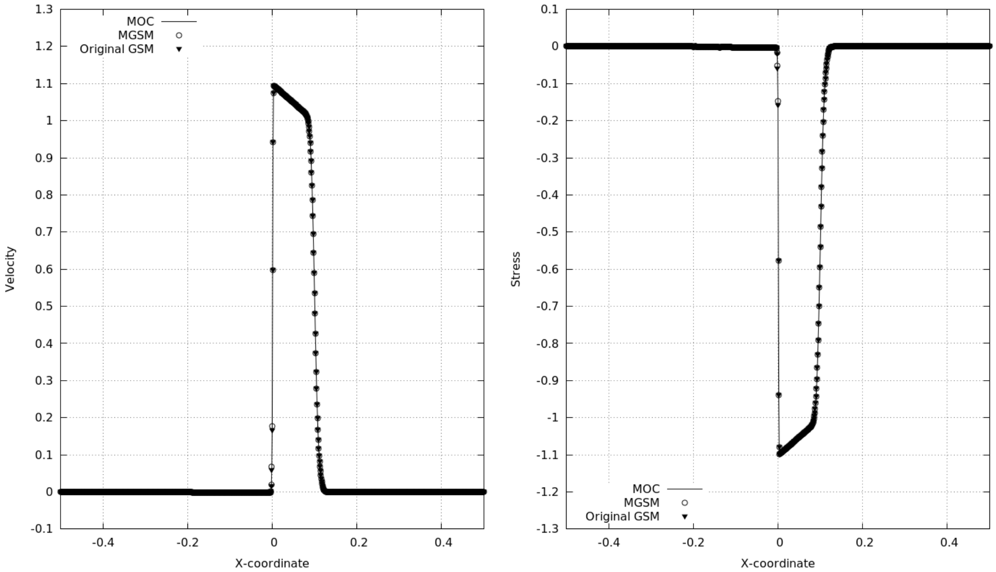

Figure 5.12: Test Example Set #4.2: velocity and stress profile. Solution is obtained for $t_f = 0.2$.

obtained using the MOC.

5.4.5 Test Example 5: On a general wave interacting with the interface in the elastic-plastic region

In this case, a general wave propagation problem is studied. We assume the solid materials obey linearly elastic, power-law work-hardening plastic stress strain relationship given by Eqn. (5.44). The material properties on the left and right side of the interface are:

$$\text{Left Solid:}\begin{cases}\rho = 1.0\\ E = 1.0\\ \alpha = 3\\ \kappa_0 = 1.5\end{cases}\qquad \text{Right Solid:}\begin{cases}\rho = 12.0\\ E = 8.0\\ \alpha = 3\\ \kappa_0 = 1.5\end{cases}.$$

The interface is located at $x_I = 0$ and the solution domain is $x \in [-4, 4]$. Zero initial conditions are assumed throughout the domain. The boundary conditions are:

$$\sigma(-4,t) = \begin{cases} 0.2, & t \leq 1 \\ 0.8t - 0.6, & 1 < t \leq 2 \\ 1.0, & t > 2 \end{cases}, \quad \text{and} \quad \sigma(4,t) = 0. \tag{5.46}$$

Grid size is $\Delta x = 0.01$ and the CFL number is 0.995. The solution is obtained for $t_f = 7.0$.

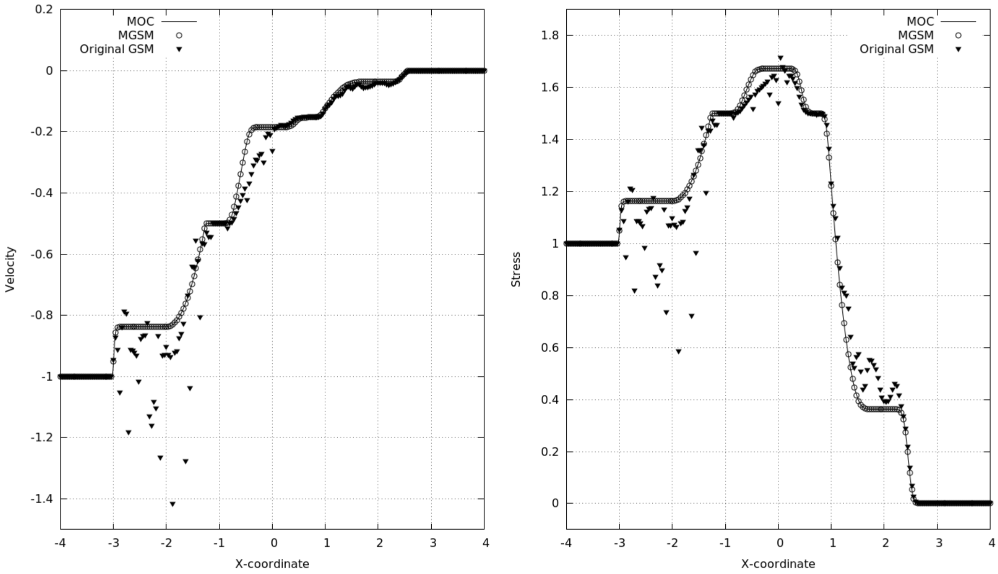

Figure 5.13: Test Example #5: velocity and stress profile. Solution is obtained for $t_f = 7.0$.

Figure 5.13 shows the stress and velocity profile. As soon as the rightward moving wave hits the interface, ϑ value exceeds the prescribed maximum permissible value of 0.1 and reaches 1.0 at $t = 4.00$. As it can be seen, the results obtained using the OGSM suffer significantly from the non-physical oscillations both in the velocity and stress profile while the MGSM results remain stable.

This confirms the predictions of the ϑ-criterion. Moreover, the MGSM results agree well with the results from the method of characteristics.

5.5 Conclusion for Chapter 5

The ghost solid methods for the elastic-plastic deformations are presented in this chapter. It is shown, under certain conditions, the OGSM can lead to large numerical errors which may or may not be in the form of non-physical oscillations. The ϑ-criterion was shown to successfully predict these errors in all settings. The MGSM has been shown to robustly perform and to be stable in all cases that the OGSM fails.

The OGSM and MGSM are also presented for the special case of the acoustic impedance matching conditions. Both exhibit robust performance, similar to that found for the elastic-elastic interactions in Chapter 3. It is also shown that, under these conditions, the ϑ-criterion successfully predicts the OGSM to remain stable.

Chapter 6

Two Dimensional Elastic-Plastic Solid Interactions

By using the techniques developed in Chapter 5, in the normal direction of the interface, one can readily extend to multi-dimensional GSM-based algorithms. One should note, however, that there are additional boundary conditions, more specifically the slip and the non-slip boundary conditions along the interface not applicable for the 1-D problem. We shall concentrate on the plain strain problem and develop our methods for the mentioned interface conditions.

6.1 Elastic-Plastic Loading Path

On the discussion on two dimensional elastic-plastic solid interaction, it is worthwhile to briefly review the fundamental theory of plasticity. We shall consider an isotropic work-hardening solid, which follows the von Mises' theory of plasticity [62]. Under plastic deformation, the deviatoric stress, $S_{kl} \equiv \sigma_{kl} - \frac{1}{3}\sigma_{mm}\delta_{kl}$, satisfies the von Mises' yield condition

$$\frac{1}{2}S_{kl}S_{kl} - \kappa^2 = 0, \tag{6.1}$$

where κ is the current yield stress. It is worthwhile to emphasize that although all three normal stresses, σ_{xx}, σ_{yy}, and σ_{zz} are present in our discussions, it is assumed there is no variation along the z-axis and hence the problem is still two dimensional. The plastic strain component increment is

$$\mathrm{d}\epsilon^p_{kl} = S_{kl}\mathrm{d}\chi, \tag{6.2}$$

where $\mathrm{d}\chi$ is a multiplier which is determined by the 1D simple shear curve. The plastic shear strain increment, $\mathrm{d}\gamma^p$, and the shear stress increment, $\mathrm{d}\tau$, are related by

$$\mathrm{d}\left(\frac{\gamma^p}{2}\right) = \frac{h}{2\mu}\mathrm{d}\tau, \qquad (h = \frac{\mu}{\mu_p} - 1), \tag{6.3}$$

where μ is the elastic shear modulus, $\mu_p = \mu_p(\tau)$ is the plastic shear modulus, which is the slope of the $\tau = \tau(\gamma)$ curve in the plastic range, and h is the plastic factor. One can determine $\mathrm{d}\chi$ by applying equations (6.1) and (6.2) to this shear problem. Then, equation (6.3) becomes:

$$\mathrm{d}\epsilon^p_{kl} = \frac{h}{2\mu}\frac{S_{kl}}{\kappa}\mathrm{d}\kappa. \tag{6.4}$$

The Ducker hypothesis, for truly plastic deformation, implies that the plastic strain components increment vector $\mathrm{d}\epsilon^p_{kl}$ is normal to the yield surface given by the equation (6.1) [116]. Moreover, the angle ψ between the vectors $\mathrm{d}S_{kl}$ and $\mathrm{d}\epsilon^p_{kl}$ is acute,

$$-\frac{\pi}{2} \leq \psi \leq \frac{\pi}{2}, \tag{6.5}$$

see Figure 6.1.

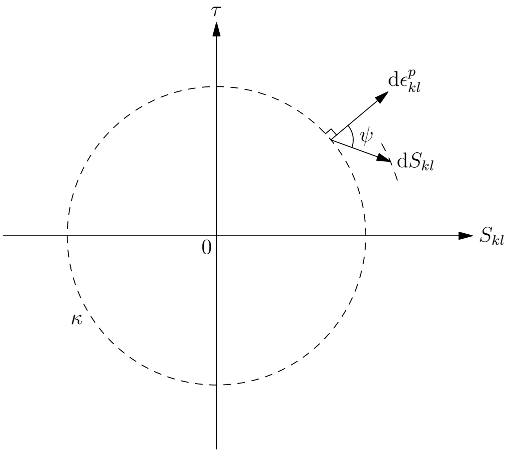

Figure 6.1: Schematics of Ducker's hypothesis

A challenge arising in the computation is to determine the angle ψ. Any angle that satisfies the equation (6.5) is physically admissible and hence the simplest one $\psi \equiv 0$ is chosen to carry out our analysis and discussion [62]. As a result, the direction of $\mathrm{d}S_{kl}$ will be normal to the yield surface. This implies that

$$\frac{\mathrm{d}S_{kl}}{S_{kl}} = \frac{\mathrm{d}\kappa}{\kappa}, \tag{6.6}$$

and consequently, equation (6.4) becomes

$$\mathrm{d}\epsilon^{p}_{kl} = \frac{h}{2\mu}\mathrm{d}S_{kl}. \tag{6.7}$$

For the materials under consideration, the volume change is elastic [62], thus

$$\mathrm{d}e^{p}_{kl} = \mathrm{d}\epsilon^{p}_{kl}, \tag{6.8}$$

where e_{kl} is the deviatoric strain, and $\mathrm{d}e_{kl}$ is its increment. Subsequently, the elastic-plastic constitutive equation becomes

$$\mathrm{d}e_{kl} = \mathrm{d}e^{e}_{kl} + \mathrm{d}e^{p}_{kl} = \frac{1+h}{2\mu}\mathrm{d}S_{kl}. \tag{6.9}$$

We shall use equation (6.9) as the constitutive equation in this chapter. Let us study the elastic-plastic loading path, in Figure 6.2, as an example. Initially, the yield surface radius is κ_i. The initial state of the loading is represented by the point i which is inside the yield surface. After loading, the system will reach

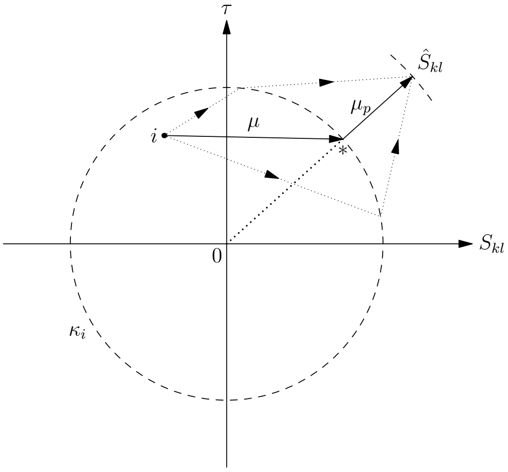

Figure 6.2: The schematics of an elastic-plastic stress loading path example.

a final state $\hat{S}_{kl}$ outside the yield surface κ_i. The above condition ensures that there is only a unique path, instead of otherwise many different paths, from i to $\hat{S}_{kl}$, i.e.,

$$S^i_{kl} \xrightarrow{\mu} S^*_{kl} \xrightarrow{\mu_p} \hat{S}_{kl}, \tag{6.10}$$

where the $*$ superscript shows the state on the initial yield surface κ_i, which is the intersection of a radial ray that passes through the origin and the final state $\hat{S}_{kl}$.

One can rewrite the von Misses yield equation (6.1) as

$$\frac{1}{3}[(p-r)^2 + (q-r)^2 - (p-r)(q-r)] + \tau^2 = \kappa^2, \tag{6.11}$$

where $p \equiv \sigma_{xx}$, $q \equiv \sigma_{yy}$, and $r \equiv \sigma_{zz}$ are the used for the normal stress components, and $\tau \equiv \sigma_{xy}$ is the shear stress component. The loading path problem can be discussed either in the S_{kl} space (Figure 6.2) or the $(p-r, q-r, \tau)$ space (Figure 6.3). In order to avoid confusion of indices of the computational cells and the stress component, we shall choose to study the loading path in the latter

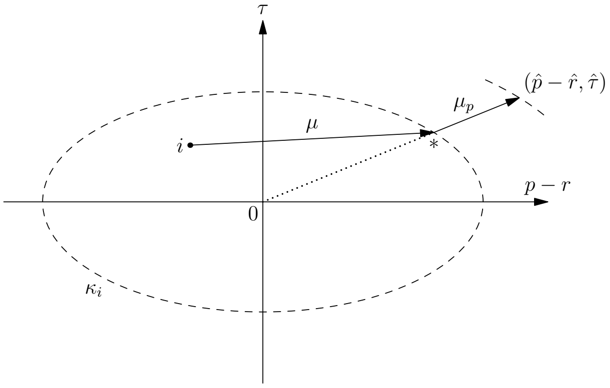

Figure 6.3: The schematics of elastic-plastic stress loading path in the $(p-r, \tau)$ space

system, $(p-r, q-r, \tau)$ space. As it can be seen in Figure 6.3 the yield surface is an ellipsoid. Consequently, the plastic loading path, from the above mentioned assumption, i.e., the direction of $(\mathrm{d}p - \mathrm{d}r, \mathrm{d}q - \mathrm{d}r, \mathrm{d}\tau)$, will no longer be in the normal to the ellipsoid yield surface. However, as the transformation from the S_{kl} to $(p-r, q-r, \tau)$ is linear, the plastic loading path will coincide with the ray that passes through the origin of the stress space [62]. If point i shows the initial state, the point $(\hat{p}-\hat{r}, \hat{q}-\hat{r}, \hat{\tau})$ shows the final state, then the point $*$ is the intersection of the yield surface κ_i and the ray that passes through the origin and the final state.

6.2 Governing Equation

The governing equations for plain strain problem of elastic-plastic solids are

$$\mathcal{A}\frac{\partial \mathbf{p}}{\partial t} = \frac{\partial \mathbf{f}}{\partial x} + \frac{\partial \mathbf{g}}{\partial y}, \tag{6.12}$$

where

$$\mathcal{A} = \begin{pmatrix} \rho & & & & & \\ & \rho & & & & \\ & & \frac{1}{3K} & & & \\ & & & \frac{1+h}{2\mu} & & \\ & & & & \frac{1+h}{2\mu} & \\ & & & & & \frac{1+h}{\mu} \end{pmatrix},$$

$$\mathbf{p} = \begin{pmatrix} u \\ v \\ p+q+r \\ p-r \\ q-r \\ \tau \end{pmatrix}, \qquad \mathbf{f} = \begin{pmatrix} p \\ \tau \\ u \\ u \\ 0 \\ v \end{pmatrix}, \qquad \mathbf{g} = \begin{pmatrix} \tau \\ q \\ v \\ 0 \\ v \\ u \end{pmatrix}.$$

In the above equation, K is the bulk modulus, and $\mathcal{A}$ is a diagonal matrix which its zeros are omitted for clarity. The third equation of the Eqn. (6.12) is obtained by assuming linear elastic changes of the volume (Section 6.1), while the fourth to sixth are derived from Eqn. (6.9) using the plain strain condition [62]. It is noted that the strain components do not appear explicitly in equation (6.12). Consequently, less computer storage is required.

Equation (6.12), can also be rewritten as:

$$\frac{\partial \mathbf{U}}{\partial t} = \mathbf{A}\frac{\partial \mathbf{U}}{\partial \eta} + \mathbf{B}\frac{\partial \mathbf{U}}{\partial \xi}, \tag{6.13}$$

where,

$$\mathbf{U} = \begin{pmatrix} u_\eta \\ u_\xi \\ \sigma_{\eta\eta} \\ \sigma_{\xi\xi} \\ \sigma_{rr} \\ \sigma_{\xi\eta} \end{pmatrix}, \quad \mathbf{A} = \begin{pmatrix} 0 & 0 & 1/\rho & 0 & 0 & 0 \\ 0 & 0 & 0 & 0 & 0 & 1/\rho \\ K + 4\mu/[3(1+h)] & 0 & 0 & 0 & 0 & 0 \\ K - 4\mu/[3(1+h)] & 0 & 0 & 0 & 0 & 0 \\ K - 4\mu/[3(1+h)] & 0 & 0 & 0 & 0 & 0 \\ 0 & \mu/(1+h) & 0 & 0 & 0 & 0 \end{pmatrix},$$

$$\mathbf{B} = \begin{pmatrix} 0 & 0 & 0 & 0 & 0 & 1/\rho \\ 0 & 0 & 0 & 1/\rho & 0 & 0 \\ 0 & K - 2\mu/[3(1+h)] & 0 & 0 & 0 & 0 \\ 0 & K + 2\mu/[3(1+h)] & 0 & 0 & 0 & 0 \\ 0 & K - 4\mu/[3(1+h)] & 0 & 0 & 0 & 0 \\ \mu/(1+h) & 0 & & 0 & 0 & 0 \end{pmatrix}.$$

Here, η and ξ are the normal and tangential directions to the interface (see Figure 6.4).

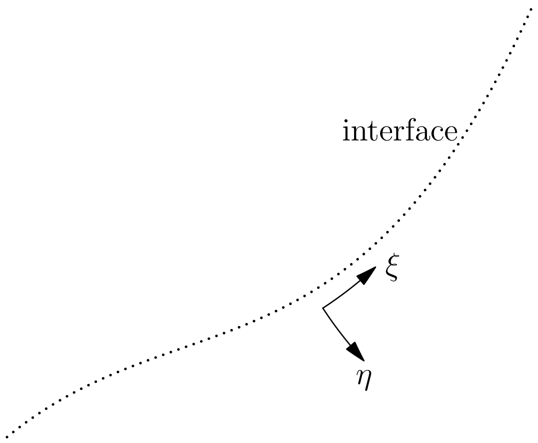

Figure 6.4: Schematic of η-ξ coordinate system

6.3 No-Slip and Perfect-Slip Conditions at the Interface

Different boundary conditions can arise at the interface. Similar to Chapter 4, we shall only discuss the no-slip and perfect-slip boundary conditions.

6.3.1 No-Slip Condition at the Interface

If the two solids cannot slide at the interface and in the absence of any gap at the interface, then a no-slip boundary condition is appropriate.

The no-gap-formation at the interface implies the continuity of the normal velocity u_η at the interface

$$u_\eta^{I_R} = u_\eta^{I_R} = u_\eta^{I}, \tag{6.14}$$

where the superscripts I_L and I_R are used to indicate if an interfacial value is calculated on the left or right side of the interface, respectively, while a superscript I is used to denote the case whereby these values are identical.

Moreover, the no-gap-formation condition means that the normal component of the traction can be non-zero, and equal for both solids. Consequently, the boundary force balance implies

$$\sigma_{\eta\eta}^{I_L} = \sigma_{\eta\eta}^{I_R} = \sigma_{\eta\eta}^{I}, \tag{6.15}$$

The no-sliding between the two solids suggests that the relative tangential velocity is zero at the interface. Hence, the tangential velocity u_ξ will be continuous across the interface

$$u_\xi^{I_L} = u_\xi^{I_R} = u_\xi^{I}. \tag{6.16}$$

It also implies that the tangential component of the traction can be non-zero and equal for both solids. Subsequently, boundary force balance leads to

$$\sigma_{\xi\eta}^{I_L} = \sigma_{\xi\eta}^{I_R} = \sigma_{\xi\eta}^{I}. \tag{6.17}$$

6.3.2 Perfect-Slip Condition at the Interface

For this interfacial boundary condition, no gap is allowed to be formed at the interface. However, the solids can slide against each other.

Similar to the previous section, the requirement of an absence of gap at the interface leads to conditions identical to (6.14) and (6.15) for the normal velocity (u) and the stress component (p). However, allowing the solids to slide, without any friction at the interface, will render conditions (6.16) and (6.17) inapplicable.

6.3.3 Coupled and Uncoupled Variables

Consider a variable χ. The superscripts I_L and I_R are used to indicate if an interfacial value is calculated on the left or right side of the interface, respectively. If due to the boundary conditions at $\mathbf{x}$, there exists a relation κ such that

$$\kappa(\chi^{I_L}, \chi^{I_R}) = 0, \tag{6.18}$$

then χ is considered to be a coupled variable across the interface at that point. Otherwise, it is uncoupled.

6.4 On the 2D OGSM

Here, we present the extension of the OGSM method given in Chapter 5. As earlier mentioned, the OGSM can be simply implemented in practice. Following the pioneering works by Fedkiw [2,88], one has to copy the coupled variable from the real nodes to the ghost nodes in the same region. Uncoupled variables, such as the material properties or loading history, must be extrapolated across the interface into the ghost nodes.

6.4.1 The OGSM for the No-Slip Condition at the Interface

Conditions (6.14), (6.15), (6.16), and (6.17) imply the variables u_η, $\sigma_{\eta\eta}$, u_ξ, and $\sigma_{\xi\eta}$ are coupled. Moreover, the Cauchy equation of motion restricts the admissible values of $\sigma_{\xi\xi}$ and σ_{rr} which makes these variables coupled. Consequently, vector $\mathbf{U}$ is a coupled variable, as each and every element of it is coupled. To define the ghost values $\mathbf{U}_L^*$ and $\mathbf{U}_R^*$, the values of $\mathbf{U}^n$ are copied from the closest real node, on the same side of the interface, to the corresponding ghost node, at each time step.

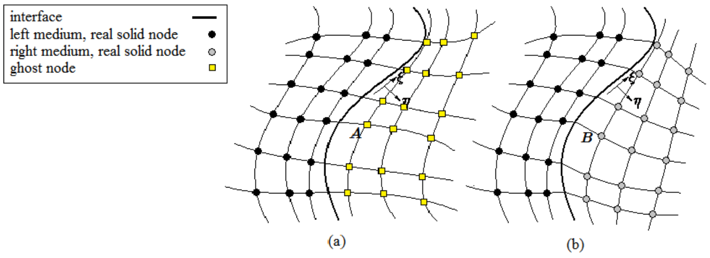

Figure 6.5: (a) presence of real and ghost solid nodes on the left hand side and the right hand side of the interface, respectively and (b) presence of real solid nodes on both sides of the interface

Consider a ghost node A on the right side of the interface. The closest real node on the same side of the interface is denoted as B (see Figure 6.5). To define the ghost values, one has to copy the coupled variables from B to A; that is

$$\mathbf{U}_R^*|_A = \mathbf{U}_B. \tag{6.19}$$

It is worthwhile to mention that one can define the location of the ghost solid nodes such that they coincide with real solid nodes. In this way, only a simple copy is necessary for defining the ghost values, and a lengthy search process can be avoided.

There are no boundary conditions to connect the material properties, as well as the loading history, on the left and right side of the interface. Hence, according to Section 6.3.3, they are the uncoupled variables. These variables are extrapolated from the real nodes, across the interface, over to the ghost nodes.

6.4.2 The OGSM for the Perfect-Slip Condition at the Interface

According to Section 6.3.2, for this case, only the conditions (6.14) and (6.15) need to be satisfied at the interface. As such, the only coupled variables are u_η and $\sigma_{\eta\eta}$. Hence, at each time step, only u_η and $\sigma_{\eta\eta}$ need to be copied from the closest real node to the ghost node. The values of u_ξ, $\sigma_{\xi\xi}$, σ_{rr}, and $\sigma_{\xi\eta}$, as well as the material properties and loading history need to be extrapolated from the real nodes, across the interface, into the ghost nodes.

6.5 On the 2D MGSM

This section is on the extension of MGSM in 1D which was developed in Section 5.3.4 to 2D. We shall extend the one dimensional MGSM in the normal direction to the interface. One has to define and solve an appropriate Riemann problem in the normal direction to the interface. Once the Riemann problem is solved and the interfacial values are obtained, the coupled variables will be copied from the interfacial solution, in the normal direction to the interface, to the ghost nodes which are along the normal to the interface. If a ghost node lies between two normals to the interface, the coupled variables can be interpolated between the interfacial values on the normals. The uncoupled variables will be extrapolated from the real nodes into the ghost nodes on the other side of the interface.

To define the Riemann problem, one needs to know the appropriate left and right values of the interface, namely $\mathbf{U}_L$ and $\mathbf{U}_R$. Moreover, the direction of the normal to the interface needs to be known at each point on the interface. For more information on how to determine the direction of the normal, $\mathbf{U}_L$ and $\mathbf{U}_R$, refer to Section 4.4.

Once $\mathbf{U}_L$ and $\mathbf{U}_R$ are determined, we shall define the following Riemann problem in the perpendicular direction to the interface,

$$\frac{\partial \mathbf{U}}{\partial t} = \mathbf{A}\frac{\partial \mathbf{U}}{\partial \eta}, \tag{6.20}$$

where

$$\mathbf{U}(\eta, t = t^n) = \begin{cases} \mathbf{U}_L^n & \eta < 0 \\ \mathbf{U}_R^n & \eta > 0 \end{cases}. \tag{6.21}$$

Characteristic analysis of the problem 6.20 leads to the following equation

$$\frac{\partial \mathbf{w}}{\partial t} - \Lambda \frac{\partial \mathbf{w}}{\partial \eta} = 0 \tag{6.22}$$

where

$$\mathbf{w}(\eta, t^n) = \begin{cases} \mathbf{w}_L^n & \eta < 0 \\ \mathbf{w}_R^n & \eta > 0 \end{cases} . \tag{6.23}$$

Here, $\mathbf{w}$ is the vector of eigen variables,

$$\mathbf{w} = \aleph \mathbf{U}, \tag{6.24}$$

where $\aleph$ is the left eigen matrix of $\mathbf{A}$:

$$\aleph = \begin{pmatrix} 0 & 0 & (2\mu - 3K)/(4\mu + 3K) & 0 & 1 & 0 \\ 0 & 0 & (2\mu - 3K)/(4\mu + 3K) & 1 & 0 & 0 \\ 0 & \sqrt{\rho\mu}/2 & 0 & 0 & 0 & 1/2 \\ 0 & -\sqrt{\rho\mu}/2 & 0 & 0 & 0 & 1/2 \\ \dfrac{(3K - 2\mu)\sqrt{\rho}}{2\sqrt{9K + 12\mu}} & 0 & \dfrac{3K - 2\mu}{3K + 4\mu} & 0 & 0 & 0 \\ \dfrac{(-3K + 2\mu)\sqrt{\rho}}{2\sqrt{9K + 12\mu}} & 0 & \dfrac{3K - 2\mu}{3K + 4\mu} & 0 & 0 & 0 \end{pmatrix} . \tag{6.25}$$

Hence, one can calculate $\mathbf{w}$ to be

$$\mathbf{w} = \begin{pmatrix} (2\mu - 3K)\sigma_{\eta\eta}/(4\mu + 3K) + \sigma_{rr} \\ (2\mu - 3K)\sigma_{\eta\eta}/(4\mu + 3K) + \sigma_{\xi\xi} \\ (\sigma_{\xi\eta} + u_\xi\sqrt{\rho\mu})/2 \\ (\sigma_{\xi\eta} - u_\xi\sqrt{\rho\mu})/2 \\ (3K - 2\mu)\left(3\sigma_{\eta\eta} + u_\eta\sqrt{\rho(9K + 12\mu)}\right)/(18K + 24\mu) \\ (3K - 2\mu)\left(3\sigma_{\eta\eta} - u_\eta\sqrt{\rho(9K + 12\mu)}\right)/(18K + 24\mu) \end{pmatrix}. \qquad (6.26)$$

Λ is the diagonal matrix of eigenvalues that is calculated by

$$\Lambda = \aleph\mathbf{A}\aleph^{-1}. \qquad (6.27)$$

The result of the above matrix operation is a diagonal matrix whose zeros which are not on the major diagonal are removed for clarity:

$$\Lambda = \begin{pmatrix} 0 & & & & & \\ & 0 & & & & \\ & & -\sqrt{\mu/\rho} & & & \\ & & & \sqrt{\mu/\rho} & & \\ & & & & -\sqrt{(K + 4\mu/3)/\rho} & \\ & & & & & \sqrt{(K + 4\mu/3)/\rho} \end{pmatrix}. \qquad (6.28)$$

The equations with positive eigenvalues correspond to leftward moving waves while the negative ones correspond to the rightward moving waves.

By integrating the characteristics equations (6.22) of the Riemann problem

(6.20), we have

$$\mathbf{w}^{I_L} = \mathbf{C}_{LL}(\mathbf{w}_L + \int_L^{I_L} d\mathbf{w}) + \mathbf{C}_{RL}(\mathbf{w}_R + \int_R^{I_L} d\mathbf{w}), \tag{6.29}$$

where $\mathbf{C}$'s are diagonal matrices. Each nonzero element of $\mathbf{C}_{LL}$ correspond to a negative or zero eigenvalue of the matrix Λ, whereas each nonzero element of $\mathbf{C}_{RL}$ corresponds to a positive eigenvalue, that is:

$$\mathbf{C}_{LL} = \begin{pmatrix} 1 &&&&& \\ & 1 &&&& \\ && 0 &&& \\ &&& 1 && \\ &&&& 0 & \\ &&&&& 1 \end{pmatrix}, \text{ and } \mathbf{C}_{RL} = \begin{pmatrix} 0 &&&&& \\ & 0 &&&& \\ && 1 &&& \\ &&& 0 && \\ &&&& 1 & \\ &&&&& 0 \end{pmatrix}. \tag{6.30}$$

The nonzero elements of the above matrices which are not on the major diagonal are omitted for clarity.

Similarly, one can obtain

$$\mathbf{w}^{I_R} = \mathbf{C}_{LR}(\mathbf{w}_L + \int_L^{I_R} d\mathbf{w}) + \mathbf{C}_{RR}(\mathbf{w}_R + \int_R^{I_R} d\mathbf{w}), \tag{6.31}$$

Each nonzero element of $\mathbf{C}_{LR}$ correspond to a negative eigenvalue of the matrix Λ, whereas each nonzero element of $\mathbf{C}_{RL}$ corresponds to a positive or zero eigenvalue, that is:

$$\mathbf{C}_{LR} = \begin{pmatrix} 0 & & & & & \\ & 0 & & & & \\ & & 0 & & & \\ & & & 1 & & \\ & & & & 0 & \\ & & & & & 1 \end{pmatrix}, \text{ and } \mathbf{C}_{RR} = \begin{pmatrix} 1 & & & & & \\ & 1 & & & & \\ & & 1 & & & \\ & & & 0 & & \\ & & & & 1 & \\ & & & & & 0 \end{pmatrix}. \quad (6.32)$$

6.5.1 On the No-Slip Condition at the Interface and MGSM

The integrations (6.29) and (6.31) together with the conditions (6.14) to (6.17) introduced in Section 6.3.1 one can solve for the $\mathbf{U}^{I_L}$ and $\mathbf{U}^{I_R}$. As the final loading conditions are unknown beforehand, one may need to use an iterative method to determine the correct loading path. This can be done by initially assuming the loading to be purely elastic. This way one can obtain the $\hat{\mathbf{p}}^{I_L}$ and $\hat{\mathbf{p}}^{I_R}$. Then, on each side of the interface, we can check if elastic-limit has been surpassed, i.e. if

$$\hat{\kappa} = \frac{1}{3}[(\hat{\sigma}_{\eta\eta} - \hat{\sigma}_{rr})^2 + (\hat{\sigma}_{\xi\xi} - \hat{\sigma}_{rr})^2 - (\hat{\sigma}_{\eta\eta} - \hat{\sigma}_{rr})(\hat{\sigma}_{\xi\xi} - \hat{\sigma}_{rr})] + \hat{\sigma}_{\eta\xi}^2 \leq \kappa^2 \quad (6.33)$$

is true, then the loading on that side is purely elastic. Consequently, $\hat{h} = 0$, and the integrals will have their usual close form.

If equation (6.33) is not satisfied on any side of the interface, then plastic deformation will occur on that side. Let us say the it is not satisfied on the left side of the interface. In this case, we need to first calculate the point $*$ which is:

$$\begin{aligned}(\sigma^*_{\eta\eta} - \sigma^*_{rr})^{I_L} &= \frac{(\hat{\sigma}_{\eta\eta} - \hat{\sigma}_{rr})^{I_L}}{\hat{\kappa}^{I_L}}\kappa_L \\ (\sigma^*_{\xi\xi} - \sigma^*_{rr})^{I_L} &= \frac{(\hat{\sigma}_{\xi\xi} - \hat{\sigma}_{rr})^{I_L}}{\hat{\kappa}^{I_L}}\kappa_L \\ (\sigma^*_{\xi\eta})^{I_L} &= \frac{\hat{\sigma}^*_{\xi\eta}}{\hat{\kappa}^{I_L}}\kappa_L\end{aligned} \quad , \tag{6.34}$$

where κ_L is the current yield surface, on the left side of the interface. Henceforth, the loading on the left side of the interface will be

$$\mathbf{w}_L \xrightarrow{\text{elastic } \mu_L} (\mathbf{w}^*)^{I_L} \xrightarrow{\text{plastic } \mu_L} \hat{\mathbf{w}}^{I_L} \ . \tag{6.35}$$

Next, the integration in (6.31) becomes

$$\int_{\mathbf{w}_L}^{\mathbf{w}^{I_L}} d\mathbf{w} = (\mathbf{w}^*)^{I_L} - \mathbf{w}_L + \int_{(\mathbf{w}^*)^{I_L}}^{\hat{\mathbf{w}}^{I_L}} d\mathbf{w}. \tag{6.36}$$

Using the above-mentioned integral in the integration (6.31), and resolving for the $\hat{\mathbf{w}}$, on the left and right side of the interface, one can get a better approximation for the interfacial values. By repeating this procedure, one can get a converged solution for $\mathbf{U}^{I_L}$ and $\mathbf{U}^{I_R}$.

It is worthwhile to mention that as the velocities u_η and u_ξ are calculated by solving the continuity equations and only depend on the density, it is not required to calculate the equivalent $*$-values for them and their current values can be used as they are, in the iterative solution for the $\mathbf{U}^{I_L}$ and $\mathbf{U}^{I_R}$.

Once the iterative solver is converged and the values of $\mathbf{U}^{I_L}$ and $\mathbf{U}^{I_R}$ are calculated, the $\mathbf{U}^{I_L}$ is copied to the ghost nodes on the right hand side of the interface which are closest to the normal line that exits the point where $\mathbf{U}^{I_L}$ was computed for. In a similar manner, $\mathbf{U}^{I_R}$ values will be copied to the proper ghost nodes on the left side of the interface.

6.5.2 On the Slip Condition at the Interface and MGSM

Here, only the conditions (6.14) and (6.15) must be satisfied for this type of interface condition. Hence, only u_η and $\sigma_{\eta\eta}$ are deemed as coupled variables.

Similar to Section 6.5.1, u_η^I and $\sigma_{\eta\eta}^I$ are identical to the values as obtained in the same section. Moreover, the zero characteristic of Eqn. (6.22) are integrated on the left and right side of the interface to obtain results identical to solutions obtained for $\sigma_{\xi\xi}^{I_L}$, $\sigma_{\xi\xi}^{I_R}$, $\sigma_{rr}^{I_L}$, and $\sigma_{rr}^{I_R}$.

The values of u_η^I and $\sigma_{\eta\eta}^I$ are then copied to the ghost nodes on the right hand side and left hand side of the interface which are closest to the normal line that exits at the point where they are calculated. In a similar manner, ($\sigma_{\xi\xi}^{I_L}$, $\sigma_{rr}^{I_L}$) and ($\sigma_{\xi\xi}^{I_R}$, $\sigma_{rr}^{I_R}$) values will be copied to the proper ghost nodes on the right side and left side of the interface, respectively.

The values of uncoupled variables, u_ξ, $\sigma_{\xi\eta}$, and material properties (including loading history) are extrapolated across the interface, accordingly.

6.6 Numerical Experiments

6.6.1 Test Example 1: Elastic-Plastic Interaction of Stress Waves Impacting on a Vertical Interface

In this numerical experiment, the accuracy and robustness of the OGSM and MGSM are compared. It will be shown that the multi-dimensional OGSM, similar to its one-dimensional counterpart can and will lead to non-physical oscillation.

The solution domain is chosen as $\Omega = \{(x, y)|x \in [0, 10] \text{ and } y \in [-5, 5]\}$. The interface is defined by the line $x = 5$. No-slip condition is assumed at the interface of the two solids.

The initial conditions are

$$u(x, y, 0) = \begin{cases} 1 & \text{where} \quad x < 5 \\ 0 & \text{where} \quad x > 5 \end{cases}, \tag{6.37}$$

and

$$v(x, y, 0) = p(x, y, 0) = q(x, y, 0) = r(x, y, 0) = \tau(x, y, 0) = 0. \tag{6.38}$$

The boundary conditions are $u(0, y, t) = 1$ and $v(0, y, t) = 0$ on the left boundary, $u(10, y, t) = v(10, y, t) = 0$ on the right boundary, and zero traction on the bottom and top boundaries of the domain.

The material properties of the left medium are $\rho_L = 1$, $K_L = 0.7$, $\mu_L = 0.8$, $(\mu_p) = 0.6$ and $\kappa_L = 0.7$ whereas the material properties for the right medium are $\rho_R = 3$, $K_R = 2$ $\mu_R = 2.5$, $(\mu_p)_R = 2.2$ and $\kappa_R = 0.7$.

The grid size is $\Delta x = \Delta y = 0.05$. A first order solver is employed and the CFL number is 0.9. The solution is obtained for $t = 0.45$. The calculated value

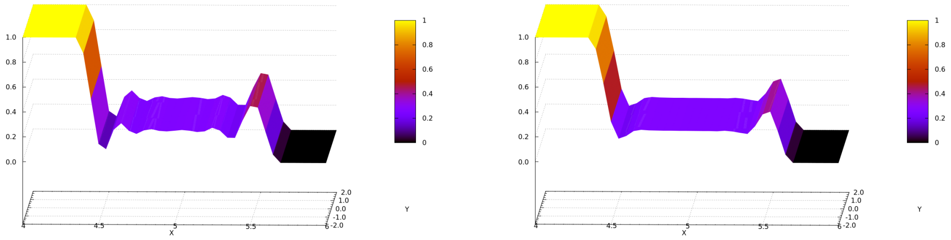

(a) u using the OGSM (e) u using the MGSM

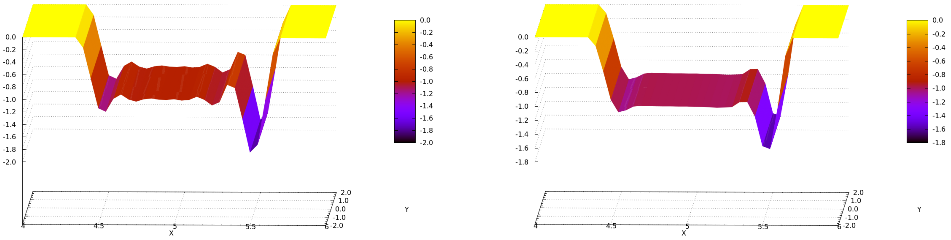

(b) σ_{xx} using the OGSM (f) σ_{xx} using the MGSM

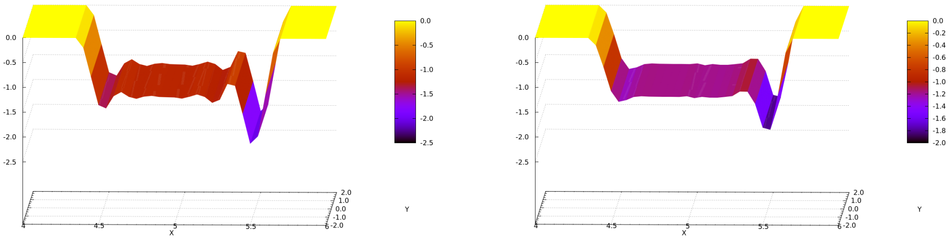

(c) $\sigma_{xx} + \sigma_{yy} + \sigma_{zz}$ using the OGSM (g) $\sigma_{xx} + \sigma_{yy} + \sigma_{zz}$ using the MGSM

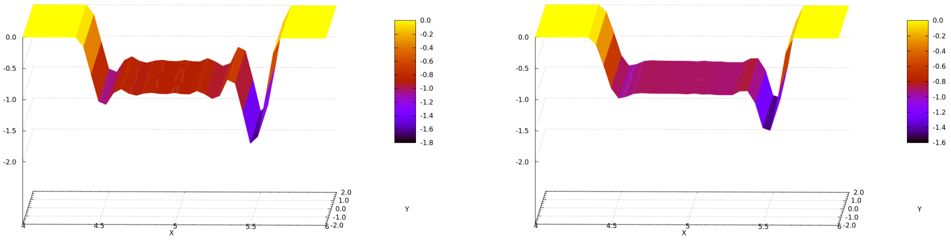

(d) $\sigma_{xx} - \sigma_{zz}$ using the OGSM (h) $\sigma_{xx} - \sigma_{zz}$ using the MGSM

Figure 6.6: Test Example 1: Comparison of the non-zero components of velocity and stress results, obtained using the OGSM and MGSM for non-slip condition at the interface for $t = 0.45$.

of ϑ for this test is close to 1.0 which is greater than $\vartheta_{crit} \approx 0.1$, for almost all the time steps. As such, this will lead to non-physical oscillations for the OGSM. Figure 6.6 compares the non-zero components of the velocity and stress results, obtained using the OGSM and MGSM for non-slip condition at the interface. The solution is obtained for $t = 0.45$. As it can be clearly seen the use of OGSM has lead to non-physical oscillations in the results of the velocity in x direction, u, and nonzero components of the stress as predicted by the ϑ-criterion. However, it is noticed that the MGSM has successfully removed these oscillations and remains stable.

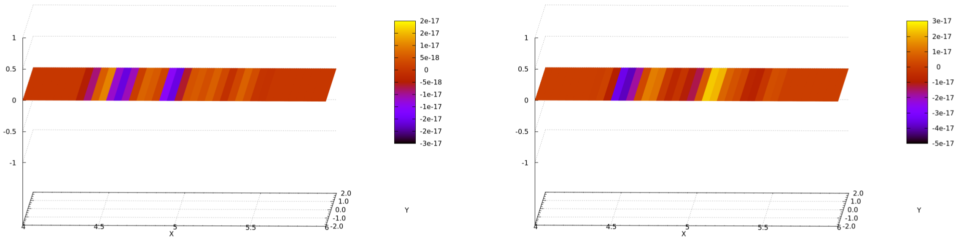

(a) v using the OGSM (d) v using the MGSM

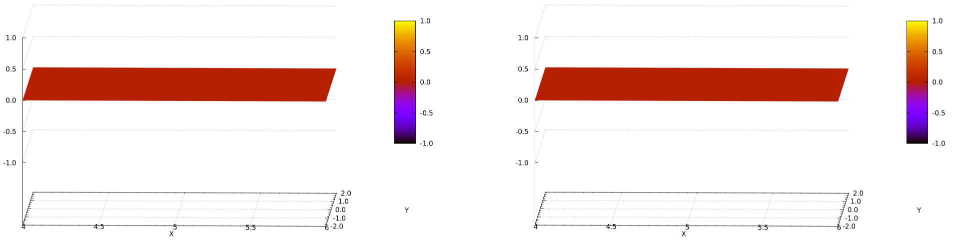

(b) $\sigma_{yy} - \sigma_{zz}$ using the OGSM (e) $\sigma_{yy} - \sigma_{zz}$ using the MGSM

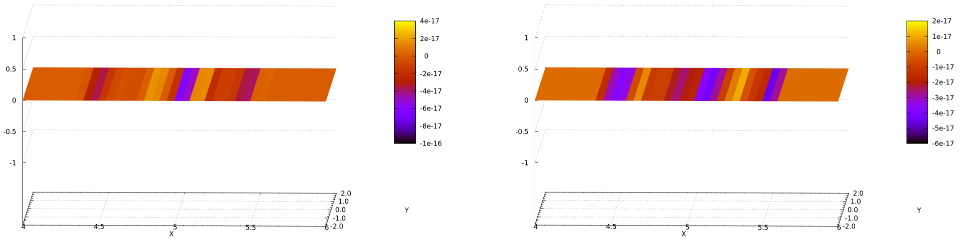

(c) σ_{xy} using the OGSM (f) σ_{xy} using the MGSM

Figure 6.7: Test Example 1: Comparison of the zero components of velocity and stress results, obtained using the OGSM and MGSM for non-slip condition at the interface for $t = 0.45$.

Figure 6.7 shows the component of velocity in the y direction, v, and the components of stress which are theoretically zero; they remain numerically close to zero (within the bounds of the numerical error), when either the OGSM or the MGSM is used. However, it is worthwhile to mention, this is not synonymous with the robustness or accuracy of the OGSM results, as the *non-zero* components suffer significantly from numerical oscillations.

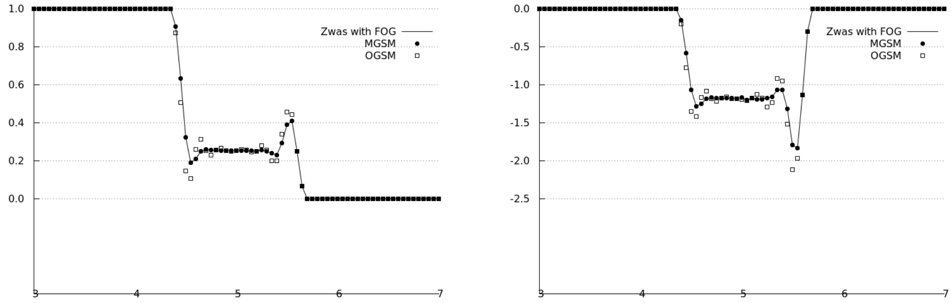

(a) u (c) $\sigma_{xx}+\sigma_{yy}+\sigma_{zz}$

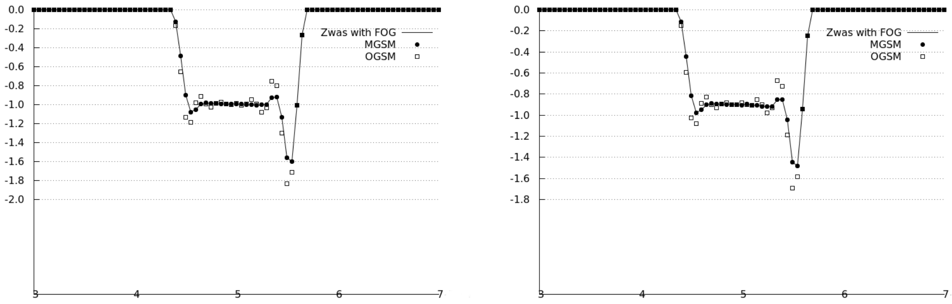

(b) σ_{xx} (d) $\sigma_{xx}-\sigma_{zz}$

Figure 6.8: Test Example 1: Comparison of the nonzero components of velocity and stress, with MGSM, OGSM, and Zwas with a first order Godunov type solver, along the $y = 0$ plane.

Figure 6.8 shows the comparison between the results obtained using the MGSM, OGSM, and Zwas method with a first order Godunov type elastic-plastic scheme [62]. It can be seen that MGSM provides an almost perfect agreement with the Zwas method. However, large deviations from the Zwas method is evident when the OGSM is employed.

These results support the robustness of the MGSM in comparison to the OGSM. Moreover, it shows that the ϑ-criterion can successfully predict the large numerical errors that may rise due to the use of the OGSM.

6.6.2 Test Example 2: Application of the GSMs to a More Complex Geometrical Setting

This experiment is designed to further show the robustness of the MGSM in dealing with more complex geometrical settings.

The solution domain is chosen as $\Omega = \{(x, y)|x \in [0, 10] \text{ and } y \in [-5, 5]\}$. The interface is a pentagon with its vertices located at the coordinates (6,0), (6.5,1), (7.5,0.5), (7.5,-0.5), and (6.5,-1). The pentagon is shown in Figure 6.9, where Ω_1 is the area outside of the pentagon which represents the first solid, and Ω_2 is the area confined by the boundaries of the pentagon which represents the second solid. Note that $\Omega_1 \cup \Omega_2 = \Omega$. A no-slip condition is assumed at the interface of the two solids.

The initial conditions are

$$u(x, y, 0) = p(x, y, 0) = \begin{cases} 1 & 5 < x < 6 \\ 0 & \text{otherwise} \end{cases}, \tag{6.39}$$

and

$$v(x, y, 0) = q(x, y, 0) = r(x, y, 0) = \tau(x, y, 0) = 0. \tag{6.40}$$

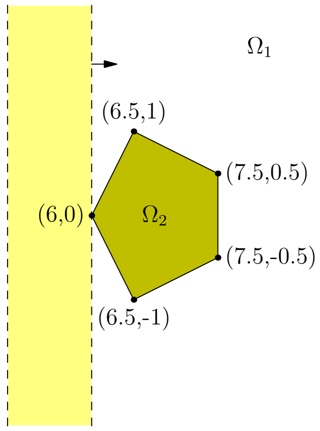

Figure 6.9: Test Example 2: A pentagonal setup is used for this problem

The boundary conditions are $u(0, y, t) = 1$ and $v(0, y, t) = 0$ on the left boundary, $u(10, y, t) = v(10, y, t) = 0$ on the right boundary, and zero traction on the bottom and top boundaries of the domain.

The material properties of the first solid as in Ω_1 are $\rho_L = 1$, $K_L = 0.7$, $\mu_L = 0.8$, $(\mu_p) = 0.6$ and $\kappa_L = 0.7$ whereas the material properties for the second solid on Ω_2 are $\rho_R = 3$, $K_R = 2$ $\mu_R = 2.5$, $(\mu_p)_R = 2.2$ and $\kappa_R = 0.7$.

The grid size is $\Delta x = \Delta y = 6.25 \times 10^{-3}$. A first order solver is employed and the CFL number is 0.51, and the solution is obtained for $t = 1.5$.

The setup of this experiment dictates the line $y = 0$ as an axis of symmetry. We expect to get increasingly symmetrical results w.r.t this line with a more accurate method.

The rightward moving wave causes elastic-plastic deformations in both of the interacting solids. The transmitted waves partly pass through the top edges of the pentagon and are partly reflected. These partial reflection of the waves create a complex wave pattern which needs to be accurately modeled.

The ϑ value remains below the prescribed permissible value of $\vartheta_{crit} = 0.1$.

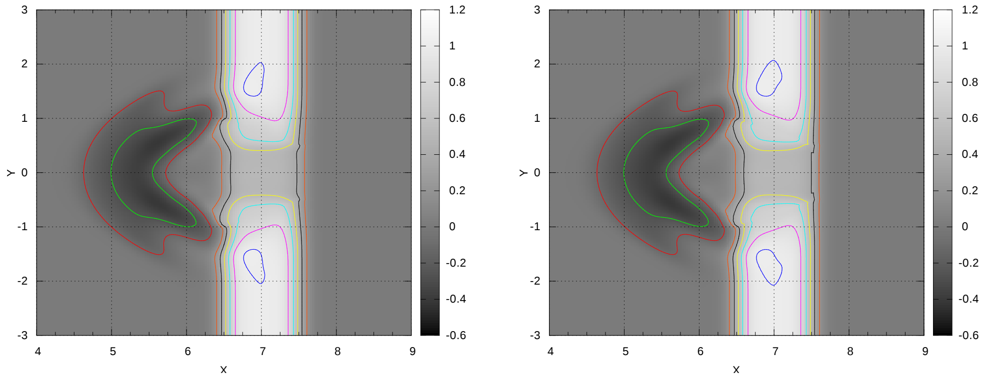

(a) u - MGSM (c) u - OGSM

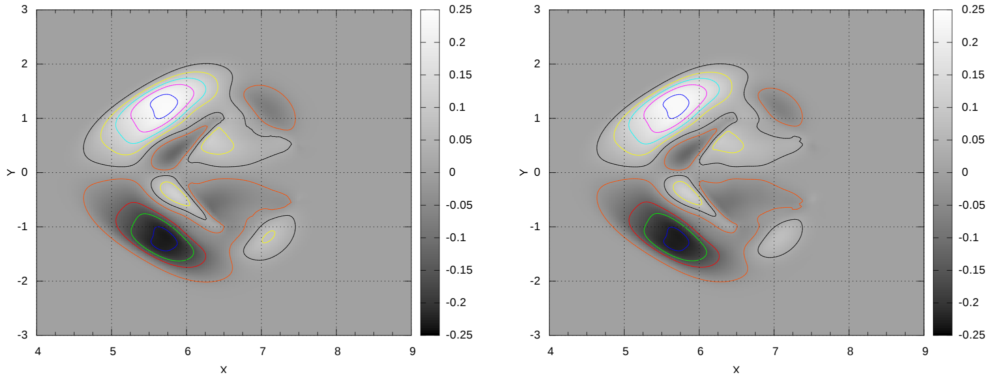

(b) v - MGSM (d) v - OGSM

Figure 6.10: Test Example 2: Contour plots of velocity u and v obtained using the MGSM and OGSM method. The results are obtained for $t_f = 1.5$.

We expect the results obtained using the OGSM to remain stable. Fig. 6.10 show the contours of u and v components of velocity obtained using the OGSM and MGSM. It is noted that the results obtained using OGSM and MGSM agree closely with the symmetrical nature of the problem. Fig. 6.11 shows contour plots of the stress components obtained using the OGSM and MGSM. It can be seen that both results maintain close symmetry along the line $y = 0$. However, it can be seen the stress contours obtained using the MGSM are sharper in comparison to the results of the OGSM which are slightly smeared close to the interface.

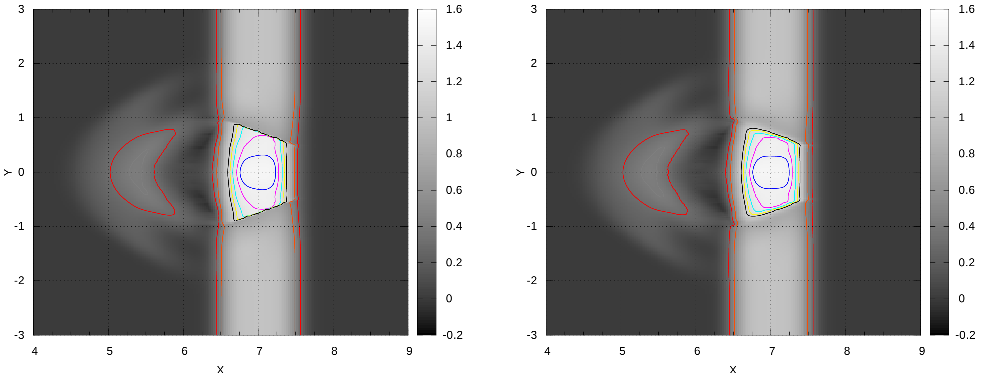

(a) σ_{xx} - MGSM (d) σ_{xx} - OGSM

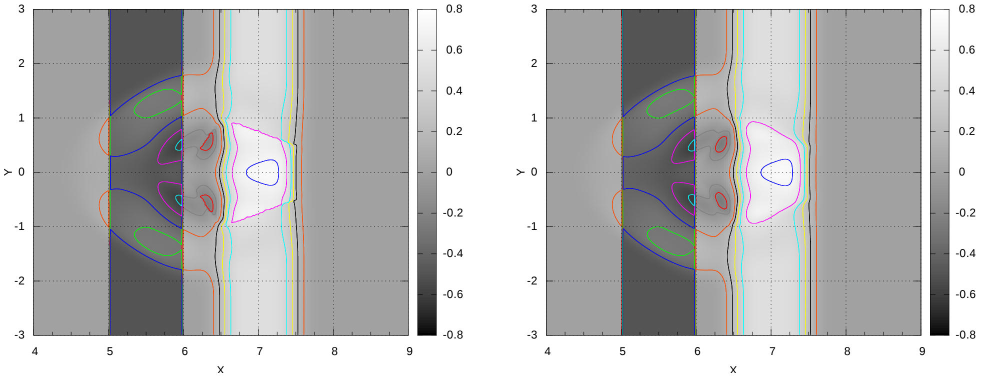

(b) σ_{yy} - MGSM (e) σ_{yy} - OGSM

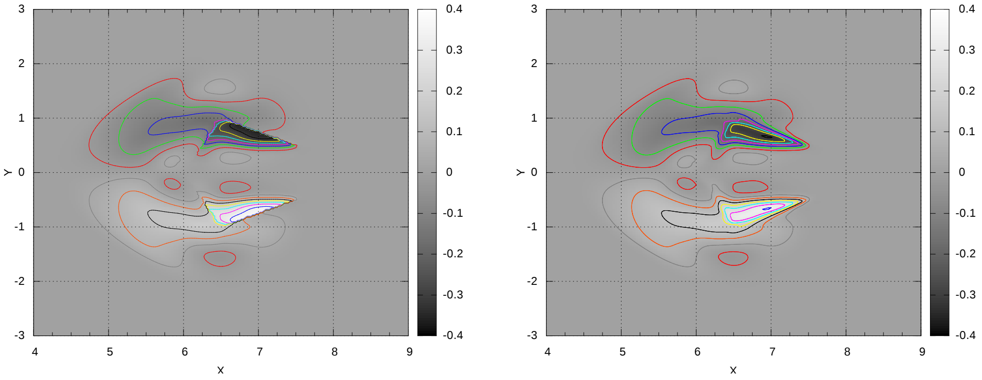

(c) σ_{xy} - MGSM (f) σ_{xy} - OGSM

Figure 6.11: Test Example 2: Contour plots of normal and tangential components of stress obtained using the MGSM and OGSM method. The results are obtained for $t_f = 1.5$.

Moreover, the geometrical setting of this problem, involves several sharp corners of the pentagon. It is noted, even in the presence of these sharp corners, the GSMs remain stable.

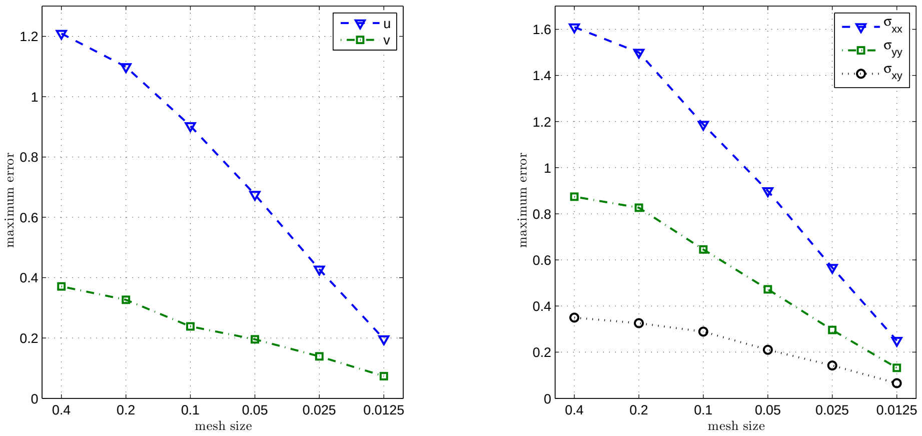

Figure 6.12: Test Example 2: Maximum numerical error for each variable at time $t_f = 1.0$ against various mesh sizes. The results are obtained using the MGSM method.

Fig. **??** shows the maximum error incurred in the calculations of the unknowns over the entire solution domain, against various mesh sizes, when the MGSM is employed. It is noted that the solution is monotonically converging. However, the order of accuracy less than first order ($O(\Delta x^{0.2})$).

This experiment attests to the robustness and viability of the MGSM in dealing with more complex geometries and wave interactions. Moreover, it shows that the ϑ-criterion is a reliable method to predict when the results of the OGSM are no-longer reliable.

6.6.3 Test Example 3: Wave interacting with a circular interface

This experiment is designed to test MGSM dealing with wave interacting with a circular interface. This will determine if the MGSM can be applied to curve interfaces. In the end, we will also provide the error analysis for this experiment.

The solution domain is chosen as $\Omega = \{(x, y)|x \in [0, 10] \text{ and } y \in [-5, 5]\}$. The interface is a unit circle with its center at (7.5,0). Ω_1 is the area outside the circle which represents the first solid, and Ω_2 is the area confined by the boundaries of the circle which represents the second solid. Note that $\Omega_1 \cup \Omega_2 = \Omega$. A no-slip condition is assumed at the interface of the two solids.

The material properties of the first solid as in Ω_1 are $\rho_L = 1$, $K_L = 0.7$, $\mu_L = 0.8$, $(\mu_p) = 0.6$ and $\kappa_L = 0.7$ whereas the material properties for the second solid on Ω_2 are $\rho_R = 5$, $K_R = 2$ $\mu_R = 2.5$, $(\mu_p)_R = 2.2$ and $\kappa_R = 0.7$.

The initial conditions for this case are:

$$u(\mathbf{x}, 0) = \sigma_{xx} = \begin{cases} 1 & 5 < x < 7 \\ 0 & \text{otherwise} \end{cases}, \quad v(\mathbf{x}, 0) = \sigma_{yy}(\mathbf{x}, 0) = \sigma_{xy}(\mathbf{x}, 0) = 0. \tag{6.41}$$

A schematics of the problem setup can be seen in Fig. 6.13. This setup provides for an axis of symmetry along the line $y = 0$.

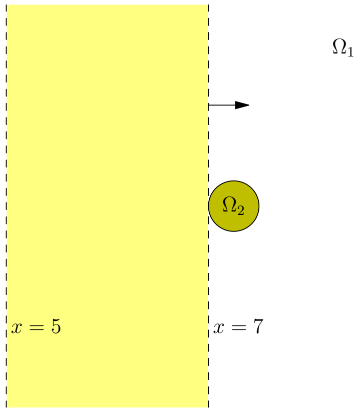

Figure 6.13: Test Example 3: Domain setup and the non-zero section of the initial condition

The grid size in this problem is $\Delta x = \Delta y = 5 \times 10^{-2}$. The CFL number used is 0.51. A FOG method is used together with the MGSM method at the circular interface. The solution is obtained for $t_f = 1.0$.

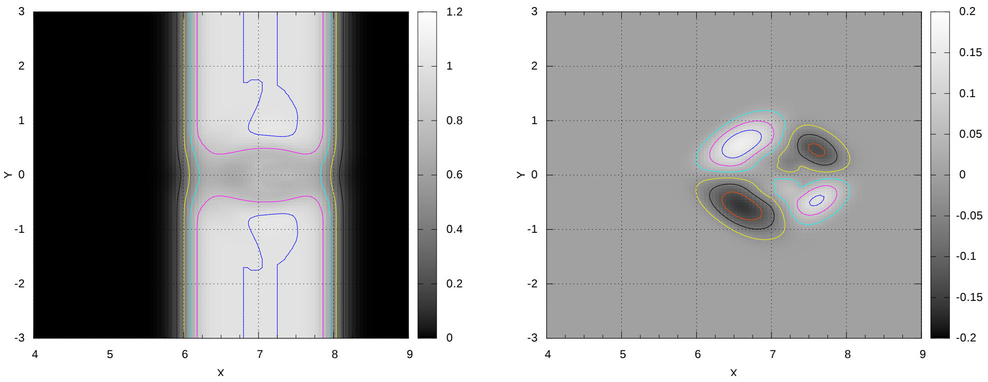

(a) u (b) v

Figure 6.14: Test Example 3: Contour plots of velocity u and v obtained using the MGSM method. The results are obtained for $t_f = 1.0$.

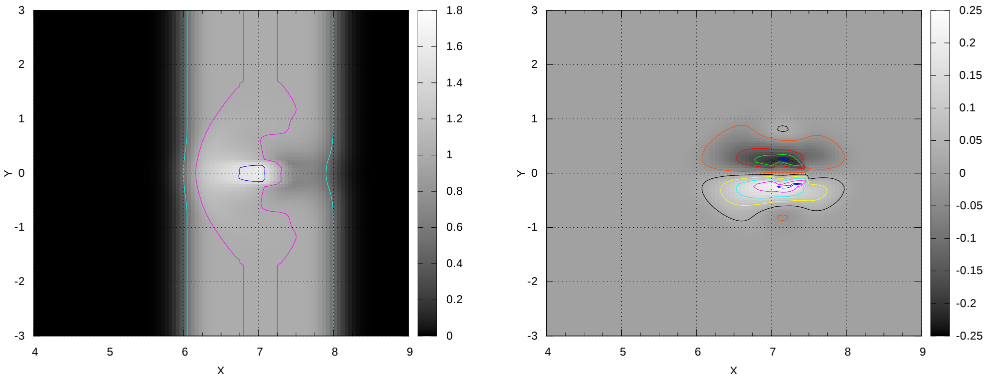

(a) σ_{xx} (b) σ_{xy}

Figure 6.15: Test Example 3: Contour plots of normal and tangential components of stress obtained using the MGSM method. The results are obtained for $t_f = 1.0$.

The rightward traveling wave hits the circular interface and partially passes through and partially is reflected the interface. The transmitted wave is later reflected on the other side of the circular interface, creating a complex interaction pattern. Figs. 6.14 and 6.15 show the velocity and stress contours obtained using the MGSM, respectively. It can be seen that the axis of symmetry, $y = 0$, is accurately maintained. The contour lines remain smooth without any numerical oscillations.

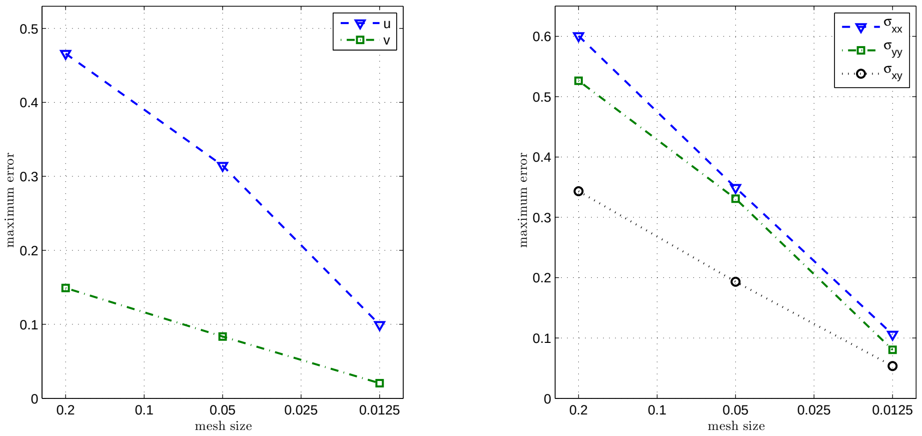

Figure 6.16: Test Example 3: Maximum numerical error for each variable at time $t_f = 1.0$ against various mesh sizes. The results are obtained using the MGSM method.

Fig. 6.16 shows the maximum numerical error incurred in calculating the velocity and stresses in the solution domain while the MGSM is applied for three different mesh sizes. As it can be seen the errors are monotonically decreasing with mesh refinement. The order of accuracy from the convergence rates is found to be almost $O(\Delta x^{0.5})$ which is less than a first order accuracy.

6.7 Conclusion for Chapter 6

In this chapter, two GSM-based algorithms were developed for the wave interaction at the solid-solid medium, with each medium governed by an isotropic elastic-plastic solid material. The OGSM method does not involve any Riemann solver to define the ghost values and hence is very easy to apply. However, it should be noted that the method can lead to severe non-physical oscillations in predicting the stress and velocity values. The ϑ-criterion was shown to be a reliable approach in predicting large numerical errors that may occur due to the OGSM. The MGSM developed in this chapter was shown to successfully and completely remove the non-physical oscillations seen when employing the OGSM. As such, no addition of numerical viscosity is necessary when the MGSM is employed. This also means that a larger possible time step can be used and the wave front will still be fairly sharp. It was also shown that MGSM can robustly be used in dealing with more complex geometries and wave interactions. Error analysis in these cases indicate that the MGSM results monotonically converge to the solution of the problem. When combined with a first order single medium solver, for the cases that we have studied, this accuracy is lower than first order.

Chapter 7

Conclusion

In this thesis, three variants of the ghost solid method were developed for the elastic-elastic and elastic-plastic solid-solid interactions. It was discussed that these methods are all considerably simple to implement, and they can be used together with a single medium solid solver of choice without the necessity to modify the single medium solid solver. These methods, when used along with their Ghost Fluid Method counterparts, potentially can provide for a coherent and consistent approach for simulating truly multi-medium problems which may involve several different layers of solids and fluids.

It was shown that the Original Ghost Solid Method (OGSM) is the most simple variant of the GSMs to implement. No Riemann problem at the interface needs to be solved. However, it was discussed that the OGSM is a highly problem related method which can, and will, lead to large numerical errors. Various cases for elastic-elastic and elastic-plastic solid-solid interactions were discussed and studied where OGSM fails and leads to large numerical errors. The source of these errors were studied, and subsequently, ϑ-criterion was proposed as a simple means to predict these errors, for all these cases. The ϑ-criterion also serves a yet more important purpose: it can be used as a measure of reliability of the OGSM results. It was discussed that if the ϑ-values remain below an empirical critical value of $\vartheta_{crit} = 0.1$, the results obtained using the OGSM are considered reliable. Otherwise, the result may suffer from large numerical errors. Undoubtedly, depending on the reliability requirements, one can impose a more stringent limit for this criterion instead of the proposed value of $\vartheta_{crit} = 0.1$. This criterion can be very useful, as OGSM is very simple to implement and can be extended into multi-dimensions. Moreover, it is not computationally expensive as no Riemann solver is required to be solved at the interface.

It was also discussed that using a higher order solid solver cannot eliminate the large numerical errors due to the OGSM. In fact, the use of a higher order solver will lead to more pronounced numerical errors caused by the OGSM. It was argued that increasing the accuracy of the solver, can reduce the stability of the solver due to the Godunov theorem.

The Modified Ghost Solid Method (MGSM) and the Double Riemann Ghost Solid Method (DRGSM) were developed. These methods were shown to be reliable alternatives for the OGSM. They were shown to be able to successfully and robustly remove the large numerical errors that would manifest in the form of non-physical oscillations. They are not problem related and remain stable in all the cases that the implementation of the OGSM would result in instability and large errors in the solution. However, it is worthwhile to mention that the MGSM required solving a Riemann problem at the interface at each time step, while the DRGSM requires solving two Riemann problems at each time step. This adds to the complexity of these methods, as compared to the OGSM.

Moreover, our extensive tests shows very little improvements when DRGSM is used as compared to the MGSM results, despite its added complexity. This means that the MGSM and solving a single Riemann problem at the interface is computationally more reasonable.

The special case of acoustic impedance matching of the solids were studied for both the elastic and elastic-plastic deformations. It was shown, for this special case, all the proposed variants of the GSM remain stable and the results closely agree with the analytical solution. It was shown that, for this case, the ϑ-value remains identically zero which makes the OGSM stable. For the case of acoustic impedance matching of the *fluids*, it was previously observed that the OGFM can lead to non-physical oscillations at the interface. Our studies show that the ϑ-value for the acoustic matching of the fluids reaches a maximum of 1.0 which is ten times larger than the prescribed value. Hence, the OGFM fails. However, for the acoustic impedance matching of the solids, ϑ is identically zero. So, the ϑ-criterion successfully explains the difference of the behavior of the OGSM and OGFM. In other words, this criterion shows that acoustic impedance matching is not necessarily the cause of the numerical errors[1]. However, a combination of factors can lead to large numerical errors. Regardless, of the combination of factors which lead to numerical errors, ϑ-criterion can successfully detect these errors.

Moreover, the elastic model and elastic-plastic model and their effect on the

---

[1] For more information, please see the Appendix.

GSMs were studied. It was observed that, on a case-by-case basis, the OGSM can perform better or worse for the elastic-plastic model. However, in all cases, the ϑ-criterion could correctly detect if the OGSM results are reliable.

The OGSM and MGSM were extended to 2D settings for the elastic-elastic and elastic-plastic solid-solid interface. Two types of interface conditions were considered, namely the no-slip condition and perfect-slip condition. The GSMs were developed for these two types of interface conditions. Their performance were also studied through numerical experiments. It was shown that the numerical errors observed in one-dimensional settings can and will also occur in multi-dimensions. Moreover, through numerical experiments it was shown that the MGSM performs robustly in multi-dimensions. Using numerical experiments, it was presented that the MGSM can be used in problems with complex geometries which involve complicated wave interactions. Error analysis and convergence analysis of the numerical experiments indicate that the MGSM monotonically converges to the analytical solution. Unfortunately, it was shown that the accuracy of the solution, once combined with a first order solver, can be less than first order.

7.1 Future Work

The following topics are suggested for future works to follow up the current research.

- A comprehensive study of the application of the GSMs and GFMs to multi-medium problems with several layers of fluids and solids.

- The GSMs and GFMs are known to be non-conservative methods. Development of conservative variants of the methods, or development of a criterion to measure conservation band of the GSMs can be beneficial for conservation sensitive problems.
- Composite materials [117] have gained significant attention in various fields, including but not limited to aerospace industries [118–120], oil and gas industries [121], and many more. Performance study of the GSMs and GFMs for numerical study of composite materials can be beneficial for numerical research in this field.
- Functionally graded materials (FGMs) [122, 123] are composite materials whose material properties changes gradually by gradual changes in the composition and micro-structure of the material. They can be designed for specific functions and application. A comprehensive study of the feasibility and robustness of the GFMs and GSMs for simulation of dynamic behavior of the FGMs in their interactions with other mediums is suggested.

Bibliography

[1] T.G. Liu, B.C. Khoo, and K.S. Yeo. Ghost fluid method for strong shock impacting on material interface. *Journal of Computational Physics*, 190(2):651–681, 2003.

[2] R.P. Fedkiw, T. Aslam, B. Merriman, and S. Osher. A non-oscillatory Eulerian approach to interfaces in multimaterial flows (the ghost fluid method). *Journal of Computational Physics*, 152(2):457–492, 1999.

[3] O.C. Zienkiewicz and P. Bettess. Fluid-structure dynamic interaction and wave forces: an introduction to numerical treatment. *International Journal for Numerical Methods in Engineering*, 13(1):1–16, 1978.

[4] S.A. Anagnostopoulos. Dynamic response of offshore platforms to extreme waves including fluid-structure interaction. *Engineering Structures*, 4(3):179–185, 1982.

[5] S.I. Sagatun, K. Herfjord, and T. Holmås. Dynamic simulation of marine risers moving relative to each other due to vortex and wake effects. *Journal of fluids and structures*, 16(3):375–390, 2002.

[6] M.P. Paıdoussis, S.J. Price, and E. de Langre. Fluid-structure interactions. *Slender Structures and Axial Flow*, 1, 2004.

[7] C.T. Yamamoto, J.R. Meneghini, F. Saltara, R.A. Fregonesi, and J.A. Ferrari Jr. Numerical simulations of vortex-induced vibration on flexible cylinders. *Journal of fluids and structures*, 19(4):467–489, 2004.

[8] S. Kaewunruen, J. Chiravatchradej, and S. Chucheepsakul. Nonlinear free vibrations of marine risers/pipes transporting fluid. *Ocean engineering*, 32(3):417–440, 2005.

[9] U. Küttler and W.A. Wall. Fixed-point fluid–structure interaction solvers with dynamic relaxation. *Computational Mechanics*, 43(1):61–72, 2008.

[10] J.R. Cebral and R. Lohner. Conservative load projection and tracking for fluid-structure problems. *AIAA Journal*, 35(4):687–692, 1997.

[11] T. Tezduyar and Y. Osawa. Fluid–structure interactions of a parachute crossing the far wake of an aircraft. *Computer Methods in Applied Mechanics and Engineering*, 191(6):717–726, 2001.

[12] F. Liu, J. Cai, Y. Zhu, H.M. Tsai, and A.S.F. Wong. Calculation of wing flutter by a coupled fluid-structure method. *Journal of Aircraft*, 38(2):334–342, 2001.

[13] A. Beckert and H. Wendland. Multivariate interpolation for fluid-structure-interaction problems using radial basis functions. *Aerospace Science and Technology*, 5(2):125–134, 2001.

[14] R. Kamakoti and W. Shyy. Fluid–structure interaction for aeroelastic applications. *Progress in Aerospace Sciences*, 40(8):535–558, 2004.

[15] T. Lieu, C. Farhat, and M. Lesoinne. Reduced-order fluid/structure modeling of a complete aircraft configuration. *Computer methods in applied mechanics and engineering*, 195(41):5730–5742, 2006.

[16] W.M. Telford. *Applied Geophysics*. Cambridge University Press, 1985.

[17] J.W. Demmel, S.C. Eisenstat, J.R. Gilbert, X.S. Li, and J.W.H. Liu. A supernodal approach to sparse partial pivoting. *SIAM Journal on Matrix Analysis and Applications*, 20(3):720–755, 1999.

[18] D. Komatitsch, C. Barnes, and J. Tromp. Wave propagation near a fluid-solid interface: A spectral-element approach. *Geophysics*, 65(2):623–631, 2000.

[19] O.A. Godin. Retrieval of green's functions of elastic waves from thermal fluctuations of fluid-solid systems. *The Journal of the Acoustical Society of America*, 125:1960, 2009.

[20] J.D. Lemmon and A.P. Yoganathan. Three-dimensional computational model of left heart diastolic function with fluid-structure interaction. *Journal of Biomechanical Engineering*, 122(2):109–117, 2000.

[21] P. Le Tallec and J. Mouro. Fluid structure interaction with large structural displacements. *Computer Methods in Applied Mechanics and Engineering*, 190(24):3039–3067, 2001.

[22] F.P.T. Baaijens. A fictitious domain/mortar element method for fluid-structure interaction. *International Journal for Numerical Methods in Fluids*, 35(7):743–761, 2001.

[23] J. De Hart, G.W.M. Peters, P.J.G. Schreurs, and F.P.T. Baaijens. A three-dimensional computational analysis of fluid–structure interaction in the aortic valve. *Journal of Biomechanics*, 36(1):103–112, 2003.

[24] C.M. Scotti, A.D. Shkolnik, S.C. Muluk, and E.A. Finol. Fluid-structure interaction in abdominal aortic aneurysms: effects of asymmetry and wall thickness. *BioMedical Engineering OnLine*, 4(1):64, 2005.

[25] J.F. Gerbeau, M. Vidrascu, and P. Frey. Fluid–structure interaction in blood flows on geometries based on medical imaging. *Computers & Structures*, 83(2):155–165, 2005.

[26] J. Leung, A. Wright, N. Cheshire, J. Crane, S. Thom, A. Hughes, and Y. Xu. Fluid structure interaction of patient specific abdominal aortic aneurysms: a comparison with solid stress models. *BioMedical Engineering OnLine*, 5(1):33, 2006.

[27] U. Küttler, M Gee, C.H. Foerster, A. Comerford, and W.A. Wall. Coupling strategies for biomedical fluid–structure interaction problems. *International Journal for Numerical Methods in Biomedical Engineering*, 26(3-4):305–321, 2010.

[28] S.P. van der Pijl, A. Segal, C. Vuik, and P. Wesseling. A mass-conserving level-set method for modelling of multi-phase flows. *International Journal for Numerical Methods in Fluids*, 47(4):339–361, 2005.

[29] H. Luo, J.D. Baum, and R. LÃűhner. On the computation of multi-material flows using ALE formulation. *Journal of Computational Physics*, 194(1):304–328, 2004.

[30] R. Abgrall and S. Karni. Computations of compressible multifluids. *Journal of Computational Physics*, 169(2):594–623, 2001.

[31] D.J. Benson. Momentum advection on unstructured staggered quadrilateral meshes. *International Journal for Numerical Methods in Engineering*, 75(13):1549–1580, 2008.

[32] D. Fressmann and P. Wriggers. Advection approaches for single- and multi-material arbitrary Lagrangian-Eulerian finite element procedures. *Computational Mechanics*, 39(2):153–190, 2007.

[33] J.S. Peery and D.E. Carroll. Multi-material ALE methods in unstructured grids. *Computer Methods in Applied Mechanics and Engineering*, 187(3-4):591–619, 2000.

[34] C.W. Hirt and B.D. Nichols. Volume of fluid (VOF) method for the dynamics of free boundaries. *Journal of Computational Physics*, 39(1):201–225, 1981.

[35] G.H. Miller and P. Colella. A conservative three-dimensional Eulerian method for coupled solid-fluid shock capturing. *Journal of Computational Physics*, 183(1):26–82, 2002.

[36] J.A. Sethian. A fast marching level set method for monotonically advancing fronts. *Proceedings of the National Academy of Sciences of the United States of America*, 93(4):1591, 1996.

[37] S. Osher and N. Paragios. Level set methods. *Geometric Level Set Methods in Imaging, Vision, and Graphics*, pages 3–20, 2003.

[38] T.G. Liu, B.C. Khoo, and K.S. Yeo. The simulation of compressible multi-medium flow. i. a new methodology with test applications to 1d gas-gas and gas-water cases. *Computers and Fluids*, 30(3):291–314, 2001.

[39] M. Arienti, P. Hung, E. Morano, and J.E. Shepherd. A level set approach to Eulerian-Lagrangian coupling. *Journal of Computational Physics*, 185(1):213–251, 2003.

[40] S. Osher and R.P. Fedkiw. *Level set methods and dynamic implicit surfaces*, volume 153. New York: Springer, 2003.

[41] E. Olsson and G. Kreiss. A conservative level set method for two phase flow. *Journal of Computational Physics*, 210(1):225–246, 2005.

[42] N. Favrie, S.L. Gavrilyuk, and R. Saurel. Solid-fluid diffuse interface model in cases of extreme deformations. *Journal of Computational Physics*, 228(16):6037–6077, 2009.

[43] P.T. Barton, D. Drikakis, and E.I. Romenski. An Eulerian finite-volume scheme for large elastoplastic deformations in solids. *International Journal for Numerical Methods in Engineering*, 81(4):453–484, 2010.

[44] P.T. Barton and D. Drikakis. An Eulerian method for multi-component problems in non-linear elasticity with sliding interfaces. *Journal of Computational Physics*, 229(15):5518–5540, 2010.

[45] P.T. Barton, B. Obadia, and D. Drikakis. A conservative level-set based method for compressible solid/fluid problems on fixed grids. *Journal of Computational Physics*, 230(21):7867–7890, 2011.

[46] P.T. Barton, R. Deiterding, D. Meiron, and D. Pullin. Eulerian adaptive finite-difference method for high-velocity impact and penetration problems. *Journal of Computational Physics*, 240(0):76 – 99, 2013.

[47] V. Dyadechko and M. Shashkov. Moment-of-fluid interface reconstruction. Technical report, Los Alamos National Laboratory, 2006.

[48] J.C. Anderson, C. Garth, M.A. Duchaineau, and K.I. Joy. Discrete multi-material interface reconstruction for volume fraction data. *Computer Graphics Forum*, 27(3):1015–1022, 2008.

[49] G.J. Fix. Phase field methods for free boundary problems. *Department of Mathematical Sciences*, 32, 1982.

[50] Z. Li. *The Immersed Interface Method A Numerical Approach for Partial Differential Equations with Interfaces*. PhD thesis, Citeseer, 1994.

[51] C. Zhang and R.J. LeVeque. The immersed interface method for acoustic wave equations with discontinuous coefficients. *Wave motion*, 25(3):237–263, 1997.

[52] Z. Li. The immersed interface method using a finite element formulation. *Applied Numerical Mathematics*, 27(3):253–267, 1998.

[53] Z. Li and M.C. Lai. The immersed interface method for the Navier-Stokes equations with singular forces. *Journal of Computational Physics*, 171(2):822–842, 2001.

[54] M.N. Linnick and H.F. Fasel. A high-order immersed interface method for simulating unsteady incompressible flows on irregular domains. *Journal of Computational Physics*, 204(1):157–192, 2005.

[55] Z. Li and K. Ito. *The immersed interface method: numerical solutions of PDEs involving interfaces and irregular domains*, volume 33. SIAM, 2006.

[56] S. Xu and Z.J. Wang. An immersed interface method for simulating the interaction of a fluid with moving boundaries. *Journal of Computational Physics*, 216(2):454–493, 2006.

[57] S.K. Sambasivan and H.S. Udaykumar. Ghost fluid method for strong shock interactions part 2: Immersed solid boundaries. *AIAA Journal*, 47(12):2923–2937, 2009.

[58] E.A. Fadlun, R. Verzicco, and P.J. Orlandi. Combined immersed-boundary finite-difference methods for three-dimensional complex flow simulations. *Journal of Computational Physics*, 161(1):35–60, 2000.

[59] C.S. Peskin. The immersed boundary method. *Acta Numerica*, 11(0):479–517, 2002.

[60] M. Uhlmann. An immersed boundary method with direct forcing for the simulation of particulate flows. *Journal of Computational Physics*, 209(2):448–476, 2005.

[61] R. Courant, K. Friedrichs, and H. Lewy. On the partial difference equations of mathematical physics. *IBM Journal of Research and Development*, 11(2):215–234, 2010.

[62] L. Xiao. *Numerical computation of stress waves in solids.* Berlin : Akademie Verlag, ©1996., 1996.

[63] M. Schäfer and I. Teschauer. Numerical simulation of coupled fluid–solid problems. *Computer Methods in Applied Mechanics and Engineering*, 190(28):3645–3667, 2001.

[64] M. Schäfer. Coupled fluid-solid problems: Survey on numerical approaches and applications. In *American Society of Mechanical Engineers, Pressure Vessels and Piping Division (Publication) PVP*, volume 460, pages 3–14. American Society of Mechanical Engineers, New York, NY 10016-5990, United States, 2003.

[65] C. Förster, W.A. Wall, and E. Ramm. Artificial added mass instabilities in sequential staggered coupling of nonlinear structures and incompressible viscous flows. *Computer Methods in Applied Mechanics and Engineering*, 196(7):1278–1293, 2007.

[66] C.A. Felippa and K.C. Park. Staggered transient analysis procedures for coupled mechanical systems: Formulation. *Computer Methods in Applied Mechanics and Engineering*, 24(1):61 – 111, 1980.

[67] W.A. Wall, D.P. Mok, and E. Ramm. Partitioned analysis approach of the transient coupled response of viscous fluids and flexible structures. In *Solids, Structures and Coupled Problems in Engineering, Proceedings of the European Conference on Computational Mechanics ECCM*, volume 99, 1999.

[68] D..P Mok and W.A. Wall. Partitioned analysis schemes for the transient interaction of incompressible flows and nonlinear flexible structures. *Trends in Computational Structural Mechanics*, pages 689–698, 2001.

[69] P. Causin, J.F. Gerbeau, and F. Nobile. Added-mass effect in the design of partitioned algorithms for fluid–structure problems. *Computer Methods in Applied Mechanics and Engineering*, 194(42):4506–4527, 2005.

[70] V. Kalro and T.E. Tezduyar. A parallel 3d computational method for fluidâĂŞstructure interactions in parachute systems. *Computer Methods in Applied Mechanics and Engineering*, 190(3-4):321 – 332, 2000.

[71] W.A. Wall, S. Genkinger, and E. Ramm. A strong coupling partitioned approach for fluid-structure interaction with free surfaces. *Computers & Fluids*, 36(1):169 – 183, 2007. Challenges and Advances in Flow Simulation and Modeling.

[72] J.F. Gerbeau and M. Vidrascu. A quasi-newton algorithm based on a reduced model for fluid-structure interaction problems in blood flows. *ESAIM: Mathematical Modelling and Numerical Analysis*, 37(04):631–647, 2003.

[73] M.Á. Fernández and M. Moubachir. A newton method using exact jacobians for solving fluid–structure coupling. *Computers & Structures*, 83(2):127–142, 2005.

[74] J. Vierendeels, L. Lanoye, J. Degroote, and P. Verdonck. Implicit coupling of partitioned fluid-structure interaction problems with reduced order models. *Computers & Structures*, 85(11):970–976, 2007.

[75] U. Küttler and W.A. Wall. Fixed-point fluid-structure interaction solvers with dynamic relaxation. *Computational Mechanics*, 43(1):61–72, 2008.

[76] U. Küttler and W.A. Wall. Strong coupling schemes for fluid-structure interaction. *Computer Methods in Applied Mechanics and Engineering, under review*, 2008.

[77] Ulrich Küttler and Wolfgang A Wall. Vector extrapolation for strong coupling fluid-structure interaction solvers. *Journal of Applied Mechanics*, 76(2):021205, 2009.

[78] M. W. Gee, U. Küttler, and W. A. Wall. Truly monolithic algebraic multigrid for fluid-structure interaction. *International Journal for Numerical Methods in Engineering*, 85(8):987–1016, 2011.

[79] M. Heil. An efficient solver for the fully coupled solution of large-displacement fluid–structure interaction problems. *Computer Methods in Applied Mechanics and Engineering*, 193(1):1–23, 2004.

[80] B. Hübner, E. Walhorn, and D. Dinkler. A monolithic approach to fluid–structure interaction using space–time finite elements. *Computer Methods in Applied Mechanics and Engineering*, 193(23):2087–2104, 2004.

[81] Y. Bazilevs, V.M. Calo, Y. Zhang, and T.J.R. Hughes. Isogeometric fluid–structure interaction analysis with applications to arterial blood flow. *Computational Mechanics*, 38(4-5):310–322, 2006.

[82] J. Liu, R.K. Jaiman, and P.S. Gurugubelli. A stable second-order scheme for fluid-structure interaction with strong added-mass effects. *Journal of Computational Physics*, 270(0):687 – 710, 2014.

[83] J. Hron and S. Turek. A monolithic FEM/Multigrid solver for an ALE formulation of fluid-structure interaction with applications in biomechanics. In *Fluid-Structure Interaction*, volume 53 of *Lecture Notes in Computational Science and Engineering*, pages 146–170. Springer Berlin Heidelberg, 2006.

[84] T.E. Tezduyar, S. Sathe, T. Cragin, B. Nanna, B.S. Conklin, J. Pausewang, and M. Schwaab. Modelling of fluid-structure interactions with the space-time finite elements: Arterial fluid mechanics. *International Journal for Numerical Methods in Fluids*, 54(6-8):901–922, 2007.

[85] M. Heil, A.L. Hazel, and J. Boyle. Solvers for large-displacement fluidâĂŞstructure interaction problems: segregated versus monolithic approaches. *Computational Mechanics*, 43(1):91–101, 2008.

[86] J. Degroote, K.J. Bathe, and J. Vierendeels. Performance of a new partitioned procedure versus a monolithic procedure in fluid–structure interaction. *Computers & Structures*, 87(11):793–801, 2009.

[87] T. Richter. A fully eulerian formulation for fluid-structure-interaction problems. *Journal of Computational Physics*, 233(0):227 – 240, 2013.

[88] R.P. Fedkiw. Coupling an Eulerian fluid calculation to a Lagrangian solid calculation with the ghost fluid method. *Journal of Computational Physics*, 175(1):200–224, 2002.

[89] R. Abgrall and S. Karni. Computations of compressible multifluids. *Journal of Computational Physics*, 169(2):594–623, 2001.

[90] C. Farhat, A. Rallu, and S. Shankaran. A higher-order generalized ghost fluid method for the poor for the three-dimensional two-phase flow computation of underwater implosions. *Journal of Computational Physics*, 227(16):7674–7700, 2008.

[91] Y. Hao and A. Prosperetti. A numerical method for three-dimensional gas-liquid flow computations. *Journal of Computational Physics*, 196(1):126–144, 2004.

[92] H. Terashima and G. Tryggvason. A front-tracking/ghost-fluid method for fluid interfaces in compressible flows. *Journal of Computational Physics*, 228(11):4012–4037, 2009.

[93] T.G. Liu, W.F. Xie, and B.C. Khoo. The modified ghost fluid method for coupling of fluid and structure constituted with hydro-elasto-plastic equation of state. *SIAM Journal on Scientific Computing*, 30(3):1105–1130, 2008.

[94] C.W. Wang, T.G. Liu, and B.C. Khoo. A real ghost fluid method for the simulation of multimedium compressible flow. *SIAM Journal on Scientific Computing*, 28(1):278–302, 2006.

[95] T.G. Liu, B.C. Khoo, and C.W. Wang. The ghost fluid method for compressible gas water simulation. *Journal of Computational Physics*, 204(1):193–221, 2005.

[96] T.G. Liu, B.C. Khoo, and W.F. Xie. The modified ghost fluid method as applied to extreme fluid-structure interaction in the presence of cavitation. *Communications in Computational Physics*, 1(5):898–919, 2006.

[97] J. Qiu, T.G. Liu, and B.C. Khoo. Simulations of compressible two-medium flow by Runge-Kutta discontinuous Galerkin methods with the ghost fluid method. *Communications in Computational Physics*, 3:479–504, 2008.

[98] G. Taylor. The use of flat-ended projectiles for determining dynamic yield stress. i. theoretical considerations. *Proceedings of the Royal Society of*

London. Series A, Mathematical and Physical Sciences, 194(1038):289–299, 1948.

[99] G. Tryggvason, B. Bunner, A. Esmaeeli, D. Juric, N. Al-Rawahi, W. Tauber, J. Han, S. Nas, and Y.J. Jan. A front-tracking method for the computations of multiphase flow. *Journal of Computational Physics*, 169(2):708–759, 2001.

[100] S.O. Unverdi and G. Tryggvason. A front-tracking method for viscous, incompressible, multi-fluid flows. *Journal of Computational Physics*, 100(1):25–37, 1992.

[101] A. Kaboudian and B.C. Khoo. The ghost solid method for the elastic solid-solid interface. *Journal of Computational Physics*, 257, Part A:102 – 125, 2014.

[102] E.F. Toro. *Riemann solvers and numerical methods for fluid dynamics: a practical introduction.* Springer Verlag, 2009.

[103] T.G. Liu, A.W. Chowdhury, and B.C. Khoo. The modified ghost fluid method applied to fluid-elastic structure interaction. *Advances in Applied Mathematics and Mechanics*, 3:611–633, 2011.

[104] P.D. Lax and R.D. Richtmyer. Survey of the stability of linear finite difference equations. *Communications on Pure and Applied Mathematics*, 9(2):267–293, 1956.

[105] R.J. LeVeque. *Finite volume methods for hyperbolic problems*, volume 31. Cambridge University Press, 2002.

[106] R.J. LeVeque. CLAWPACK software. `http://depts.washington.edu/clawpack/`. Accessed: June 15, 2013.

[107] A. Harten. The artificial compression method for computation of shocks and contact discontinuities. iii. self-adjusting hybrid schemes. *Mathematics of Computation*, 32(142):363–89, 1978.

[108] E. Kreyszig. *Advanced Engineering Mathematics.* John Wiley & Sons, 2006.

[109] A.S. Scott. The method of characteristics & conservation laws. *Journal of Online Mathematics and its Applications*, 2004.

[110] R. Courant and D. Hilbert. *Methods of mathematical physics*, volume 1. Wiley.com, 2008.

[111] F. John. *Partial differential equations.* Springer-Verlag, New York, 1982.

[112] L.C. Evans. Partial differential equations. Technical report, American Mathematical Society, 1998.

[113] A.D. Polianin. *Handbook of first order partial differential equations.* Taylor & Francis, London New York, 2002.

[114] A.D. Polianin. *Handbook of linear partial differential equations for engineers and scientists.* Chapman & Hall/CRC, Boca Raton, 2002.

[115] M. Delgado. Classroom note: The Lagrange-charpit method. *SIAM Review*, 39(2):298–304, 1997.

[116] R. Hill. *The mathematical theory of plasticity*, volume 11. Oxford University Press, 1998.

[117] R.F. Gibson. *Principles of composite material mechanics*, volume 218. CRC Press, 2012.

[118] S. Abrate. Impact on laminated composite materials. *Applied Mechanics Reviews*, 44(4):155–190, 1991.

[119] P.D. Mangalgiri. Composite materials for aerospace applications. *Bulletin of Materials Science*, 22(3):657–664, 1999.

[120] D.U. Shanyi. Advanced composite materials and aerospace engineering [j]. *Acta Materiae Compositae Sinica*, 1:000, 2007.

[121] J. Vandiver. Research challenges in the vortex-induced vibration prediction of marine risers. In *Offshore Technology Conference*, 1998.

[122] S. Suresh, A. Mortensen, and S. Suresh. *Fundamentals of functionally graded materials.* Institute of Materials London, 1998.

[123] Y. Miyamoto. *Functionally graded materials: design, processing, and applications.* Kluwer Academic Publishers, Boston, 1999.

Appendix A

Applicability of the ϑ-criterion to the OGFM

The Original Ghost Fluid Method (OGFM) with isentropic fix has been shown not to work consistently and efficiently when applied to strong shocks impacting on a material interface [1]. Liu et al studied the causes of such inapplicability [1]. Here, we shall briefly discuss the applicability of the ϑ-criterion, introduced in Sections 3.4.4 and 5.3.5, in predicting such problems for the OGFM.

A.1 The Original GFM on Shock Refraction

Here, we shall follow the 1D analysis presented by Liu et al [1]. The 1D Euler equation can be formulated as

$$\frac{\partial \mathbf{U}}{\partial t} + \frac{\partial \mathbf{F}(\mathbf{U})}{\partial x} = 0, \tag{A.1}$$

where $\mathbf{U} = [\rho, \rho u, E]^T$, $\mathbf{F}(\mathbf{U}) = [\rho u, \rho u^2 + p, (E + p)u]^T$, ρ is the density, u is the velocity, p is the pressure, and E is the total energy which is given by

$$E = \rho e + \rho u^2/2. \tag{A.2}$$

Here, e is the specific internal energy. The Mie-Gruneison family of equations of state (EOS), used for the closure of the system, are formulated as

$$\rho e = f(\rho)p + g(\rho), \tag{A.3}$$

where f and g are functions of density and heat conductivity [2]. We shall use the γ-law for perfect gases which implies $f = 1/(\gamma - 1)$ and $g = 0$.

We shall now consider two of the cases studied by Liu et al [1] where OGSM leads to large errors. We consider a shock wave impacting the interface from medium 2 (see Figure A.1).

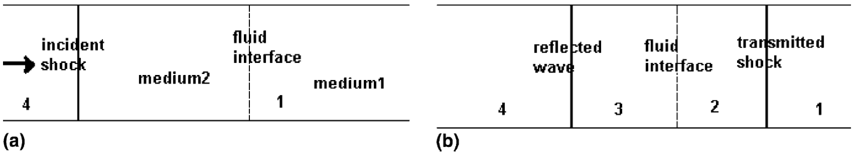

Figure A.1: (a) Before shock refraction. (b) After shock refraction [1].

A constant pressure and velocity profile which is identical over both mediums, denoted by p_1 and u_1, is assumed initially. Eqn. A.1 is the governing equation, and the following initial conditions are assumed:

$$\mathbf{U}|_{t=0} = \begin{cases} \mathbf{U}_4, & x < x_{0s}, \\ \mathbf{U}_{02}, & x_{0s} < x < x_0, \\ \mathbf{U}_{01}, & x > x_0, \end{cases} \cdot \tag{A.4}$$

Here, $\mathbf{U}_4$, $\mathbf{U}_{02}$, and $\mathbf{U}_{01}$ represent the status behind the incident shock, the status ahead of the incident shock, and the initial status of medium 1, respectively. x_{0s} and x_0 denote the initial locations of shock front and the interface, respectively. The Rankine-Hugoniot jump conditions are satisfied for the incident shock, which is

$$\mathbf{F}(\mathbf{U}_4) - \mathbf{F}(\mathbf{U}_{02}) = s_4(\mathbf{U}_4 - \mathbf{U}_{02}), \tag{A.5}$$

where s_4 is the speed of the incident shock. Isentropic fix is applied and a MUSCL scheme is used. The domain of solution is $[0, 1]$, the grid size is $\Delta x = 0.005$ and is uniform over the domain. A CFL number of 0.9 is employed.

A.1.1 Numerical Examples on Application of the OGFM

Case 1: Strong shock on a gas-gas interface

The initial flow conditions for this case are $p_1 = 1.0$, $u_1 = 0.0$, $\rho_{01} = 0.1$, $\rho_{02} = 1.0$, $\gamma_1 = 1.4$ and $\gamma_2 = 1.6667$. The incident shock strength is $p_4/p_1 = 100.0$. The Rankine-Hugniot jump conditions are used to determine the parameters behind and ahead of the shock. The initial locations of the interface, and the incident wave-front are $x_0 = 0.4$ and $x_{0s} = 0.3$, respectively. The solution was obtained for 200 time steps, and the results of the last time step are compared against the analytical solution (see Figure A.2). It can be seen in Figure A.2 there are large

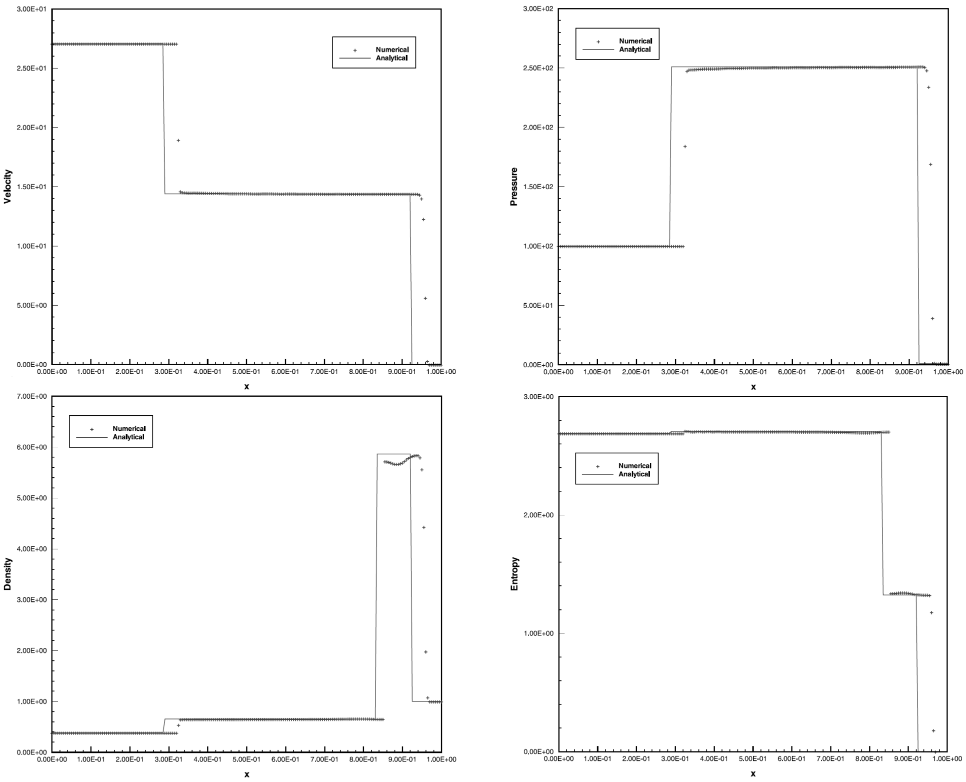

Figure A.2: Case 1: comparison of velocity (top left), pressure (top right), density (bottom left), and entropy (bottom right) profiles obtained using the OGFM against analytical solution [1].

numerical errors both in the location of the wave front and also in the velocity, pressure, density, and entropy profiles when the solution is compared against the analytical results.

The error analysis of this problem was carried out by Liu et al [1]. Figure A.3 shows the comparison of the conservation errors between the OGFM and MGFM. The ϑ value calculated using these results, indicate a $\vartheta_{max} = 1.0$ has been reached which is 10 times larger the maximum permissible value of $\vartheta_{crit} = 0.1$. Henceforth, the criterion is breached, and subsequently, large discrepancies between the numerical results using the OGSM and the analytical solution are

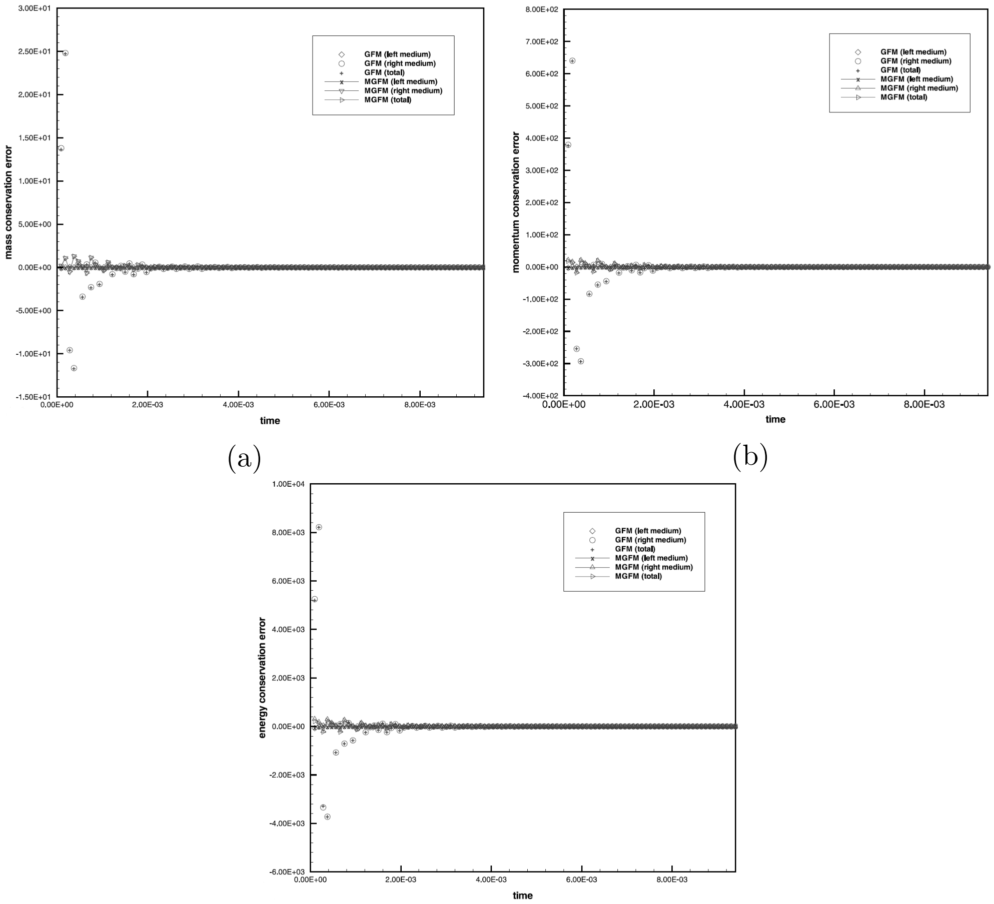

(a) (b)

(c)

Figure A.3: Case 1: comparison of (a) mass conservation error, (b) momentum conservation error, and (c) energy conservation error between the original GFM (OGFM) and the modified GFM (MGFM) [1].

observed.

Case 2: Shock impedance matching on a gas-gas interface

In solid-solid interactions, it was observed that under acoustic impedance matching conditions, the incident wave passes through without any wave reflection at the interface when the OGSM was employed. ϑ values remained identically zero, which predicted agreement between the analytical solution and the OGSM results, which was observed in the numerical experiments.

However, in fluid-fluid interactions, the story plays out differently and the OGFM leads to a reflected wave at the interface which does not agree with the analytical solution. We shall show that the ϑ-criterion can still successfully predict these discrepancies.

This case is specifically designed to enforce a condition that the refracted wave produces no reflection at the interface. In other words, shock impedance matching conditions are satisfied. The incident shock strength is $p_4/p_1 = 100$. The flow parameters, chosen according to the following critical condition

$$\frac{(\gamma_1 - 1)\rho_{01}}{(\gamma_2 - 1)\rho_{02}} = \frac{1 + \tau_2 p_4/p_1}{1 + \tau_1 p_4/p_1}, \tag{A.6}$$

are $p_1 = 1.0$, $u_1 = 0.0$, $\rho_{02} = 0.8236907$, $\rho_{01} = 1.0$, $\gamma_2 = 5/3$, and $\gamma_1 = 1.2$. Here, $\tau = (\gamma + 1)/(\gamma - 1)$. The initial location of the shock front and interface is $x_{0s} = x_0 = 0.2$. A MUSCL-solver has been employed, together with the original GFM, and 200 time steps of computations have been carried out. Our calculations indicate that a $\vartheta_{max} = 1.0$ has been reached which exceeds the maximum permissible value of $\vartheta_{crit} = 0.1$. As such, it is predicted that large numerical errors may occur in the results. Figure A.4 shows the velocity, pressure, and density profiles for the final time step of the calculations. As earlier mentioned, for this case, there should be no shock reflection at the interface. However, as can be seen in this figure, a clear reflected non-physical hump in the velocity profile, and a non-physical depression in the pressure and density profiles can be observed in the results obtained with the OGFM. Moreover, the OGFM has also lead to over-prediction of density in the transmitted wave. This

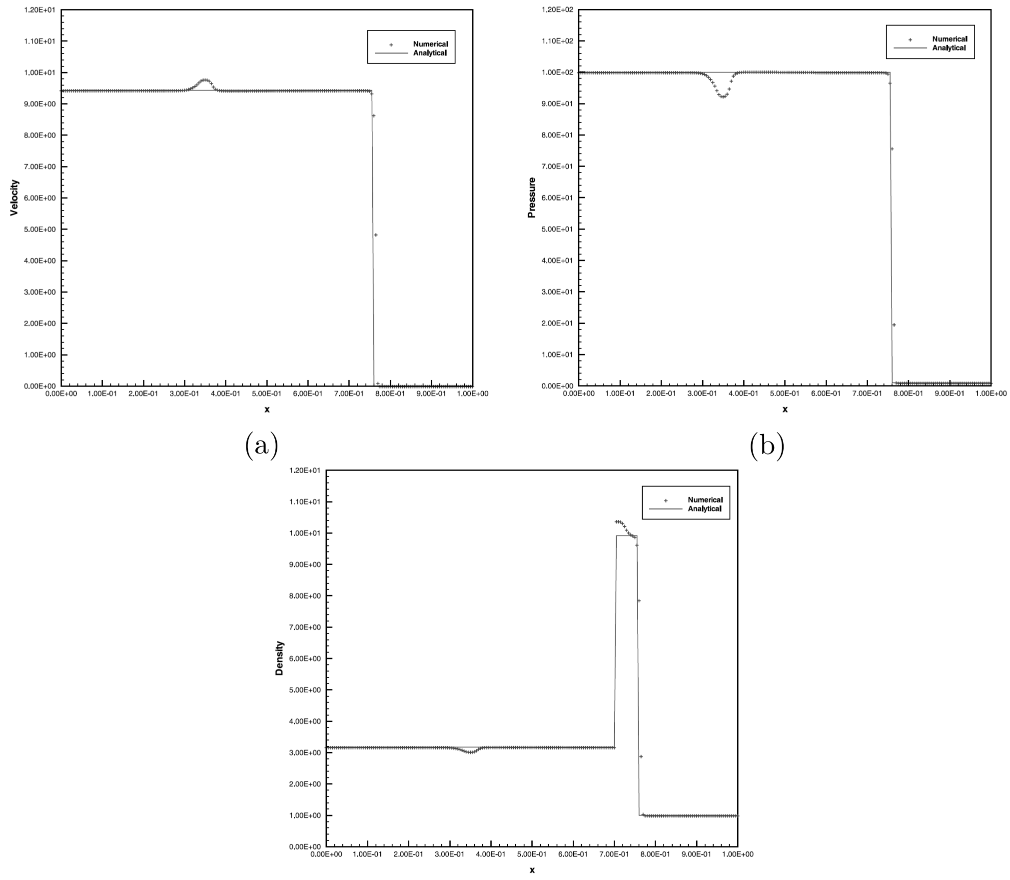

(a) (b)

(c)

Figure A.4: Case 2: comparison of (a) velocity, (b) pressure, and (c) density profiles between the original GFM (OGFM) and the analytical solution [1].

confirms that once the ϑ-criterion is breached, the results obtained using the OGFM are no longer reliable.

Our calculations indicate that for all the cases presented in the work by Liu et al [1] where OGFM leads to large numerical errors, the ϑ-criterion has been breached. This indicates that the ϑ-criterion can be used as a simple and robust means to determine when the results obtained using the OGFM are no longer reliable.

Case 3: the OGFM with no large errors

In this numerical example, we shall study a case whereby the OGFM works well with no oscillations. In this way, we can further test the robustness of the ϑ-criterion. This problem is taken from [2].

A γ-gas law has been assumed to solve for a simple one phase problem. For this fluid, $\gamma = 1.4$. The flow properties on the left and right of the interface are $\rho_L = 2$ `kg/m`^{3}, $\rho_R = 1$ `kg/m`^{3}, $p_L = 9.8 \times 10^5$ `Pa`, $p_R = 2.45 \times 10^5$ `Pa`, and $u_L = u_R = 0$ `m/s`. The domain of the solution is 4 `m` long, and 100 grid points have been considered. The initial location of the interface is between the 50th and 51st grid points. The solution was obtained for the final time of $t_f = 0.0022$ `s`.

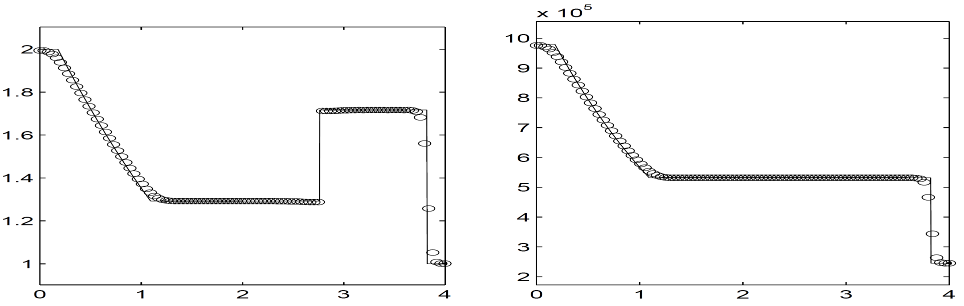

(a) density (ρ) (c) pressure (p)

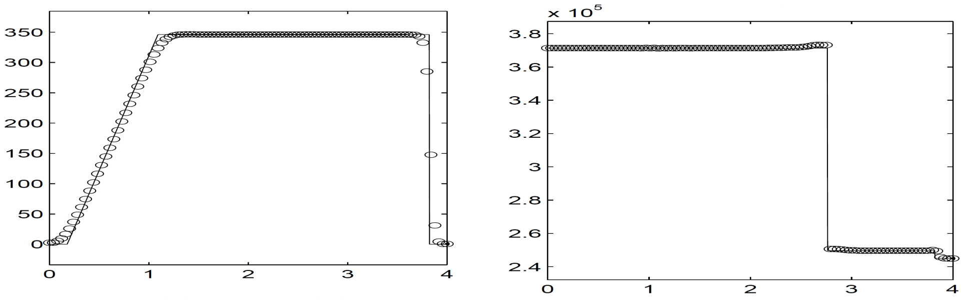

(b) velocity (u) (d) entropy (s)

Figure A.5: Case 3: comparison of the Original Ghost Fluid Method (OGFM) (circles) and the analytical solution (solid line) [2].

Our calculations indicate that for this test example ϑ value remains below $\vartheta_{crit} = 0.1$ during the computations. According to the ϑ-criterion, no large numerical errors are expected to appear in the solution obtained by the OGFM. As can be seen in Figure A.5, the numerical results follow the analytical solution very well. This further attests that the ϑ-criterion can be a good measure as to how reliable the OGFM results are.